A RELUCTANCE MESH-BASED MODELING METHOD FOR ELECTROMAGNETIC CHARACTERIZATION AND RADIAL FORCE CALCULATION IN SWITCHED RELUCTANCE MACHINES

A RELUCTANCE MESH-BASED MODELING METHOD FOR ELECTROMAGNETIC CHARACTERIZATION AND RADIAL FORCE CALCULATION IN SWITCHED RELUCTANCE MACHINES

BY

GAYAN MADUSANKA AMARADASA WATTHEWADUGE, MSc

A THESIS

SUBMITTED TO THE DEPARTMENT OF ELECTRICAL AND COMPUTER ENGINEERING

AND THE SCHOOL OF GRADUATE STUDIES

OF MCMASTER UNIVERSITY

IN PARTIAL FULFILMENT OF THE REQUIREMENTS

FOR THE DEGREE OF

DOCTOR OF PHILOSOPHY

Doctor of Philosophy (2022) McMaster University

(electrical and computer engineering) Hamilton, Ontario, Canada

TITLE:	A Reluctance Mesh-Based Modeling Method for Electromagnetic Characterization and Radial Force Calculation in Switched Reluctance Machines
AUTHOR:	Gayan Madusanka Amaradasa Watthewaduge MSc (Electrical Engineering), University of Manitoba, Winnipeg, Canada
SUPERVISORS:	Dr. Berker Bilgin and Dr. Ali Emadi
NUMBER OF PAGES:	xxxvi, 186

Lay Abstract

Electric motors are utilized in our daily life in various applications such as washing machines, refrigerators, air conditioners, fans, vacuum cleaners, blenders, and many other devices and tools. Motors are widely used in residential, industrial, commercial, and transportation applications. Due to the environmental impact of burning fossil fuels, transportation systems are moving into electrified propulsion. Electric motors with lower cost and higher efficiency are on the path to replacing the traditional combustion engines in vehicles. Among the different electric motors available, switched reluctance motor (SRM) is becoming a promising candidate in future electrified transportation systems due to their simple construction. Developing a motor is a time-consuming and costly task. Therefore, it is essential to determine the characteristics of an SRM before manufacturing it. A mathematical framework is proposed in this thesis to address this problem. The proposed framework is capable of determining the characteristics of an SRM accurately.

Abstract

Switched Reluctance Machines (SRMs) are gaining more attention due to their simple and rugged construction, low manufacturing cost, and high-speed operation capability. An electromagnetic model of the machine is needed in the design and analysis processes. The required accuracy level of the model depends mainly on the application.

Designing an SRM is an iterative process. Usually, finite element method (FEM) is employed in all design stages, which might require extensive computation burden. The magnetic equivalent circuit (MEC) method is an alternative for typical FEM. MEC models require less computational resources and they can help determine the electromagnetic performance with a reasonable accuracy. The conventional MEC method can be challenging when modifying the motor geometry while conducting dynamic analysis with current control. This thesis proposes a reluctance mesh-based MEC model for SRMs that can overcome those challenges. Reluctance mesh-based MEC models are developed for 3-phase 6/4, 6/16, 12/8 SRMs and 4-phase 8/6, 8/10, and 16/12 SRMs. The implemented MEC-based modeling method is validated using FEM and experimental results.

Acoustic noise and vibration is one of the shortcomings of an SRM. The radial force density in the airgap should be calculated before analyzing and mitigating acoustic

noise and vibration. This thesis proposes a radial force density calculation method for SRMs using the proposed MEC model. Fourier series is used to calculate the harmonics of the radial force density. The results obtained from the MEC model are verified using FEM models.

SRM is a promising candidate for electric propulsion systems. In the design process of an SRM, the motor geometry needs to be determined. This thesis applies the proposed MEC technique to the design process of a 3-phase 12/16 SRM for a high lift motor in the NASA Maxwell X-57 electric aircraft. The design is verified using the results computed from FEM.

In dedication to

My Wife and My Parents

All My Teachers

And Friends

Acknowledgements

This thesis becomes successful with the support of many individuals. I would like to convey my sincere appreciation to all of them.

First, I would like to express my sincere gratitude to my supervisors, Prof. Berker Bilgin and Prof. Ali Emadi, for their continuous guidance, valuable time, consistent advice, and knowledge sharing throughout the research. Their wisdom, vision, and efficient workflow helped me to successfully complete my research and gather everlasting life lessons. I am thankful to Prof. Ali Emadi for giving me the invaluable opportunity to be a part of a world-class research group.

I would like to extend a special thank you to my supervisory committee members, Prof. Babak Nahid-Mobarek and Dr. Jin Ye, for their valuable feedback and discussions throughout my research. I especially thank Dr. Gaoliang Fang for his support with the experimental analysis.

This research was undertaken, in part, thanks to funding from the Canada Research Chair in Transportation Electrification and Smart Mobility, Mitacs Accelerate Program, and the Department of Electrical and Computer Engineering (ECE) at McMaster University.

I am grateful to my colleagues at McMaster Automotive Resource Centre (MARC) for their support and friendship throughout my studies. A Special thanks go to

Dr. Alan Callegaro, Dr. Ehab Sayed, Dr. Giorgio Pietrini, Dr. Diego Fernando Valencia Garcia, John Ramoul, Alexander Forsyth, Cyrille Goldstein, and Mohamed Abdelmagid. Thank you to my Sri Lankan friends in Canada for giving me a wonderful time during my studies.

I have no words to express my gratitude to my parents and my sisters. I would not be here today without their love and support.

I would like to thank all of my teachers for giving me the knowledge and life lessons.

At last, big thanks to my wife, my only family member in Canada, Guvanthi, for her love, support, encouragement, and patience throughout these three years.

Thank you All!

Table of Contents

List of Figures

List of Tables

List of Symbols

Vectors

$\vec{A}$	Magnetic vector potential	Wb/m
$\vec{B}$	Magnetic flux density vector	T
$\vec{E}$	Electric field intensity vector	V/m
$\vec{H}$	Magnetic field intensity vector	A/m
$\vec{J}$	Current density vector	A/m^2
$\vec{T}$	Electric vector potential	A/m

Matrices

$\boldsymbol{A}_b \in \mathbb{R}^{n_b \times 1}$	Branch area vector
$\boldsymbol{B} \in \mathbb{R}^{n_b \times 1}$	Magnetic flux density vector
$\boldsymbol{C} \in \mathbb{R}^{n_l \times n_l}$	Branch and loop connection matrix
$\boldsymbol{F}_l \in \mathbb{R}^{n_l \times 1}$	Loop MMF vector
$\boldsymbol{H} \in \mathbb{R}^{n_l \times n_l}$	Hessian matrix

$\boldsymbol{I}_s \in \mathbb{R}^{m\times 1}$	Excitation current vector
$\boldsymbol{J} \in \mathbb{R}^{n_l\times n_l}$	Jacobian matrix
$\boldsymbol{L} \in \mathbb{R}^{n_b\times n_l}$	Loop matrix
$\boldsymbol{M} \in \mathbb{R}^{n_b\times m}$	Phase split matrix
$\boldsymbol{N} \in \mathbb{R}^{n_l\times m}$	Loop winding function matrix
$\boldsymbol{N}_b \in \mathbb{R}^{n_b\times 1}$	Branch winding function vector
$\boldsymbol{\nu}_r \in \mathbb{R}^{n_b\times 1}$	Relative reluctivity vector
$\boldsymbol{\nu}'_r \in \mathbb{R}^{n_b\times 1}$	Derivative of relative reluctivity vector
$\boldsymbol{\phi}_b \in \mathbb{R}^{n_b\times 1}$	Branch flux vector
$\boldsymbol{\phi}_l \in \mathbb{R}^{n_l\times 1}$	Loop flux vector
$\boldsymbol{\psi} \in \mathbb{R}^{m\times 1}$	Phase flux linkage vector
$\boldsymbol{r} \in \mathbb{R}^{n_l\times 1}$	Residual vector
$\boldsymbol{R} \in \mathbb{R}^{n_l\times n_l}$	Reluctance network matrix
$\boldsymbol{R}_b \in \mathbb{R}^{n_b\times 1}$	Branch reluctance vector
$\boldsymbol{r}_d \in \mathbb{R}^{(n_l+m)\times 1}$	Extended residual vector
$\boldsymbol{R}_s \in \mathbb{R}^{m\times m}$	Phase resistance matrix
$\boldsymbol{V}_{ph} \in \mathbb{R}^{m\times 1}$	Phase voltage vector

e^{th} mesh element

$A_{rad,e}, A_{tan,e}$	Radial and tangential cross-sectional area	m^2
$B_{rad,e}, B_{tan,e}$	Radial and tangential flux densities	T
F_{s1}, F_{s2}	MMF values of the sources	A.turns
$\phi_1, \phi_2, \phi_3, \phi_4$	Branch fluxes across the reluctances	Wb
R_1, R_2	Radial and tangential reluctance elements	A.turns/Wb
T_0, T_1, T_2	Nodal electric vector potentials	A/m
θ_e, θ_{e-1}	Spatial positions	degree
U_0, U_1, U_2, U_3, U_4	Nodal magnetic scalar potentials	A/m
V_e	Volume of the mesh element	m^3
W_e	Magnetic energy of the mesh element	J

Other scalars

$A_{c,g}$	Air area of the complex mesh element	m^2
$A_{c,st}$	Steel area of the complex mesh element	m^2
$A_{c,st}$	Total area of the complex mesh element	m^2
β_r	Rotor pole arc angle	rad or degrees

β_s	Stator pole arc angle	rad or degrees
B_{rad}, B_{tan}	Radial and tangential flux density in the airgap	T
D_{bore}	Bore diameter	mm
Δt	Integration time step	s
D_{out}	Outer diameter	mm
D_{shaft}	Bore diameter	mm
E	Electromotive force	V
e_j	j^{th} phase induced voltage	V
F	Magnetomotive force	A.turns
f_{elec}	Electrical frequency	Hz
f_{fc}	Forcing frequency	Hz
f_{mech}	Mechanical frequency	Hz
F_s	MMF in the airgap	A.turns
g	Airgap length	mm
h_r	Rotor pole height	mm
h_{rb}	Rotor back-iron thickness	mm
h_s	Stator pole height	mm
h_{sb}	Stator back-iron thickness	mm

I	Electric current	A
i_j	j$^{\text{th}}$ phase current	A
k_{id}	Configuration index	
L_a	Phase inductance at aligned position	H
L_{ax}	Total axial length	mm
L_{end}	End turn length	mm
L_j	j$^{\text{th}}$ phase inductance	H
L_{stk}	Stator core stack length	mm
L_u	Phase inductance at unaligned position	H
m	Number of phases in the SRM	
μ	Material permeability	H/m
n_b	Number of branches in the MEC	
n_l	Number of flux loops in the MEC	
N_r	Number of rotor poles	
N_{rpm}	Rotor speed in RPM	rpm
N_s	Number of stator poles	
n_s	Number of airgap mesh elements in each layer	
N_t	Number of turns per coil	

$N(\theta_s)$	Winding function	turns
$n(\theta_s)$	Turns function	turns
ν	Material reluctivity	m/H
ν_0	Reluctivitiy of air	m/H
$\nu_{r,comp}$	Relative reluctivity of complex element	Wb/A.turns
$\nu_{r,g}$	Relative reluctivity of air	Wb/A.turns
$\nu_{r,st}$	Relative reluctivity of steel	Wb/A.turns
ω_r	Rotation speed of the rotor	rad/s
ϕ	Magnetic flux	Wb
ψ_j	j$^{\text{th}}$ phase flix linkage	Wb.turns
R_{coil}	Coil resistance	Ω
R_{elec}	Resistance	Ω
ρ	Material resistivity	Ωm
R_j	j$^{\text{th}}$ phase resistance	Ω
R_{mag}	Reluctance	A.turns/Wb
s_f	Scaling factor	
σ	Material conductivity	S/m
$\sigma_{rad}, \sigma_{tan}$	Radial and tangetial force densities	N/m^2

t	Time	
τ_r	Rotor pole taper angle	rad or degrees
τ_s	Stator pole taper angle	rad or degrees
$T_{e,j}$	j$^{\text{th}}$ phase electromagnetic torque	Nm
θ_r	Mechanical rotor position	degree or rad/s
θ_s	Spatial position in the airgap	degree
θ_{sp}	Stator pole pitch	degree
T_{pukse}	Number of torque pulsations	
U	Magnetic scalar potential/magnetic voltage	A.turns
V	Electric scalar potential/voltage	V
v_j	j$^{\text{th}}$ phase voltage	V
W_c	Magnetic co-energy	J
W_f	Magnetic energy	J
W_{mech}	Mechanical energy	J

List of Abbreviations

AI	Artificial intelligence
ANFIS	Adaptive neural fuzzy inference system
ANN	Artificial Neural Network
BEM	Boundary element method
BEMF	Back electromotive force
BM	Breathing mode
BVP	Boundary value problem
CCW	Counter-clockwise
CFNN	Cascade-forward-backpropagation neural network
CM	Conformal mapping
CW	Clockwise
DL	Double layer
EMF	Electromotive force
FDM	Finite difference method
FE	Finite element

FEA	Finite element analysis
FEM	Finite element method
FFT	Fast Fourier transform
FRA	Finite-reluctance approach
GDS	Grid-diamond search
GRNN	General regression neural network
HLM	High lift motor
LSSVM	least square support vector machine
LUT	Look-up tables
MEC	Magnetic equivalent circuit
ML	Machine learning
MST	Maxwell Stress Tensor
OF	Objective function
PM	Permanent magnet
PMSM	Permanent magnet synchronous motor
RBF	Radial basis function
RMS	Root-mean squared
RMSE	Root-mean-squared-error
RNN	Recurrent neural networks
SC	Schwartz-Christoffel
SL	Single layer

SRM	Switched reluctance motor
TSF	Torque sharing function
WFSM	Wound field synchronous machine

Declaration of Academic Achievement

All of the text and figures presented in thesis were created by Gayan Watthewaduge unless explicitly stated otherwise. Any ideas that were not original or based on academic literature have been properly referenced to the authors' best knowledge. The only exception to this is where such information is considered as basic common knowledge in the field. The [1, 2, 4, 5] were published based on the work in this research. The content in the Chapter 3 is based on [1], and Chapter 4 is an extension of work presented in [2, 4]. The Chapter 5 is based on the work presented in [5].

thesis, the IEEE does not endorse any of McMaster University's products or services. Internal or personal use of this material is permitted. If interested in reprinting/republishing IEEE copyrighted material for advertising or promotional purposes or for creating new collective works for resale or redistribution, please go to to learn how to obtain a License from RightsLink.

Chapter 1

Introduction

1.1 Background and Motivation

Switched reluctance machine (SRM) is a viable alternative for typical induction and permanent magnet (PM) machines, which are currently the dominant technologies in various applications. There are multiple advantages of SRMs such as simple construction, lower cost, wider speed range, and more stable supply chain security [1, 6]. Electromagnetic design of an SRM is an iterative process that involves stages such as initial sizing, performance optimization, and loss calculation [7, 8]. Different types of electromagnetic models can be utilized in those stages. Electromagnetic models are essential to determine the geometry parameters of an SRM with fair accuracy. Finite element method (FEM) is typically used in all design stages, but FEM can be complex and account for a substantial time when applied at all design stages [9]. The magnetic equivalent circuit (MEC) technique is a viable alternative to FEM [10–12]. In the MEC method, the flux flow in the magnetic domain is considered as a magnetic circuit, which is analogous to current flowing in an electric circuit [13]. MEC technique

can consider the magnetic saturation and has reasonable accuracy compared to FEM. There are two approaches for the MEC technique: i) conventional MEC method and ii) reluctance mesh-based MEC method [1]. Local saturation, mutual coupling, and leakage flux can be accounted for both in the conventional and reluctance mesh-based MEC techniques.

The conventional MEC approach has been widely applied to model various types of SRMs. The main drawback of the conventional MEC technique is that the flux paths inside the magnetic device should be predefined to develop the magnetic circuit. The computation time for this technique is lower compared to FEM [1]. In [14–17], the conventional MEC technique has been applied to model SRMs that have a conventional geometry. The same technique has also been utilized for modeling E-core and C-core SRMs in [12] and [18]. Moreover, double-sided linear SRM and axial flux segmented rotor SRM are modeled in [19] and [20] using the conventional MEC method. The MEC models developed in [12, 14, 16] and [17] provided only the static characteristics. Additionally, the dynamic characteristics are modeled in [15] and [18–20], and the mutual coupling has been taken into account in [15] and [18].

The reluctance mesh-based MEC method does not require pre-defining the flux path in the machine. The accuracy and computation time for this technique are usually higher than the conventional MEC technique [1]. It can be applied to model motors in both two and three dimensions [21–23]. In [22] and [23], the reluctance mesh-based MEC method has been applied to model induction machines. The reluctance mesh technique has also been applied to model numerous types of PM machines [21, 24–26].

In a typical SRM design process, the pole configuration is identified to satisfy

the design requirements and the motor geometry is modified iteratively considering the performance with dynamic current. An MEC model of the SRM would provide strong benefits in sizing the motor geometry for different pole configurations. The conventional MEC method would be challenging to implement as the flux path would need to be predefined for each pole configuration and different geometrical constraints. The reluctance mesh-based MEC technique has been rarely applied to model SRMs, but it can overcome the challenges with the conventional MEC method. Therefore, this thesis proposes a 2-dimensional (2D) reluctance mesh-based MEC model for SRMs. The developed model accounts for local saturation, leakage and fringing fluxes, and multiphase excitation. The models of 3-phase 6/4, 6/10, 12/8 SRMs, and 4-phase 8/6, 8/10, and 16/12 SRMs are implemented using the reluctance mesh-based MEC technique. The static and dynamic characteristics of those SRMs are computed. Corresponding 2D FEM models have been utilized to validate the results from the MEC models. The simulated static and dynamic performances are further validated using experimental results on a 4-phase 8/6 SRM. The proposed 2D reluctance mesh-based MEC model is utilized to calculate the radial force density in 6/4, 6/10, 12/8, 8/6, 8/10, and 16/12 SRMs. Finally, the proposed MEC method is applied to design 3-phase 12/16 SRM for the performance requirements of the NASA high lift motor (HLM) for the Maxwell X-57 aircraft [3]. Both radial force calculation and 12/16 SRM design are validated using FEM results.

1.2 Thesis Contributions

The author has presented five main contributions in this thesis.

1. The author proposes a comprehensive electromagnetic model for SRMs using the reluctance mesh-based MEC method. The proposed technique does not require predefining the flux path inside the machine, which is a major drawback in the MEC modeling method.

2. Both current and voltage excitation features are included in the developed MEC model to apply in both static and dynamic analysis.

3. The proposed method has considered local saturation, leakage and fringing fluxes and multi-phase excitation. The proposed MEC model has the capability for modeling SRMs with different pole configurations. The proposed model can determine the magnetic energy, magnetic flux density, magnetic field intensity, flux linkage, electromagnetic force and torque.

4. A technique for calculating the radial force density of SRMs is proposed using the developed reluctance mesh-based MEC model. The proposed radial force density calculation method can determine the radial force density in the airgap and stator radial force.

5. The proposed reluctance mesh-based MEC method is applied to design 13.7 kW 3-phase 12/16 SRM for electric aircraft propulsion motor. The initial sizing of the motor geometry is determined using the proposed MEC method. The design specifications of the SRM are obtained from the permanent magnet synchronous

motor (PMSM) designed by NASA for their high lift motor (HLM) in Maxwell-X57 electric aircraft.

1.3 Thesis Outline

The rest of the chapters in this thesis is organized as follows.

Fundamentals of the SRMs are discussed in Chapter 1. The operational principle of an SRM is explained, and derivation of the pole configuration is discussed. The winding configurations of a conventional SRM are also studied. Additionally, SRM drives and current regulation techniques are discussed.

Chapter 3 presents a survey of electromagnetic modeling techniques of electric machines. Then, the discussion is narrowed down to review the analytical modeling techniques, numerical modeling techniques, and MEC modeling techniques of SRMs.

The proposed of the reluctance mesh-based modeling technique is introduced in chapter 4. The calculation of the electromagnetic quantities of the 3-phase 6/4, 6/10, 12/8 SRMs, and 4-phase 8/6, 8/10, and 16/12 SRMs are also discussed. Then, simulation results for the static and dynamic characteristics are presented and compared with FEM results. Furthermore, the experimental test results are presented to validate the proposed MEC method.

Chapter 5 presents the radial force densities calculation using the proposed reluctance mesh-based MEC model by applying the Maxwell Stress Tensor method. The calculated radial force and radial force density results for the 3-phase and 4-phases SRMs from the MEC model are validated using the FEM.

Sizing of a 3-phase 12/16 SRM for the HLM in NASA Maxwell-X57 electric aircraft is presented in Chapter 6. The design specifications provided by NASA for their

permanent magnet-based HLM are studied. The proposed SRM motor geometry is presented. The static and dynamic characteristics of the SRM obtained from the MEC model are validated using the FEM results.

Finally, conclusions and future works are presented in chapter 7.

Chapter 2

Fundamentals of Switched Reluctance Motors (SRMs)

2.1 Introduction

In this chapter, the operating principle of an SRM is discussed. The pole configurations and different winding techniques of an SRM with conventional excitation are also analyzed. The operation modes of the asymmetric bridge converter and the hysteresis current regulation method is discussed.

2.2 Operational Principal

Typically, SRMs have a double salient structure. The number of poles in the stator and rotor determines the pole configuration of the SRM. Fig. 2.1 (a) shows an SRM having four stator poles and two rotor poles, and it is a 4/2 SRM. As shown in

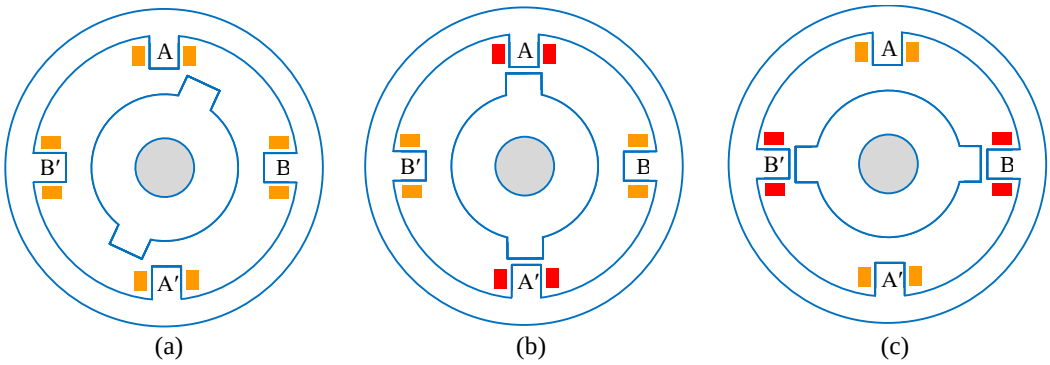

Figure 2.1: Operation of 2-phase 4/2 SRM (a) initial rotor position while phases are not energized, (b) after energizing the phase-A, and (c) after energizing the phase-B.

Fig. 2.1 (a), 4/2 SRM can operate as a two phase machine. After energizing phase-A, the rotor aligns with the stator poles of phase-A to form a minimum reluctance path between stator and rotor as shown in Fig. 2.1 (b). Similarly, phase-B can be energized, and the rotor aligns with the stator poles of phase-B as shown in Fig. 2.1 (c). Continuous rotation can be achieved by energizing and de-energizing phase-A and phase-B alternatively [27]. The reluctance in the magnetic circuit of an SRM change when the rotor rotates. Thus, the flux linkage of a phase winding is a function of rotor position.

The ideal phase flux linkage characteristics of an SRM is shown in Fig. 2.2. The variables α_1 and α_2 are $(\beta_r - \beta_s)/2$ and $[180°/N_r - (\beta_r + \beta_s)/2]$, respectively. As shown in Fig. 2.2, three main regions are identified based on the rotor position [6,27]. These positions are aligned, partial-overlap, and unaligned positions, as shown in Fig. 2.3. At the aligned position, the rotor pole fully overlaps the excited stator pole, whereas it partially overlaps the stator pole in the partial-overlap position as shown in Fig. 2.3(b). There is no overlap between the rotor poles and the excited stator pole at the unaligned region, as shown in Fig. 2.3(c). It should be indicated that

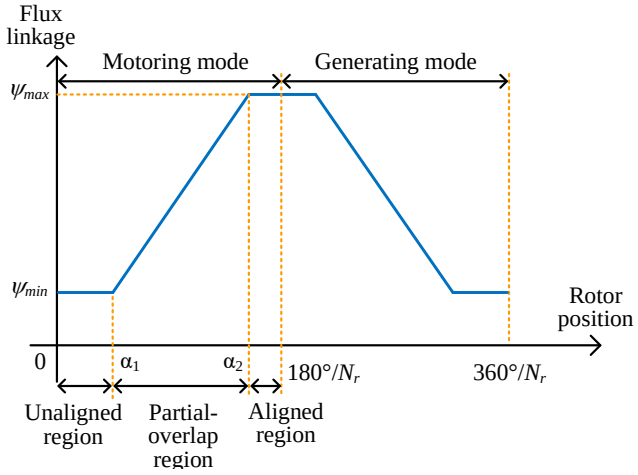

Figure 2.2: Ideal inductance vs. rotor position characteristics of an SRM [1].

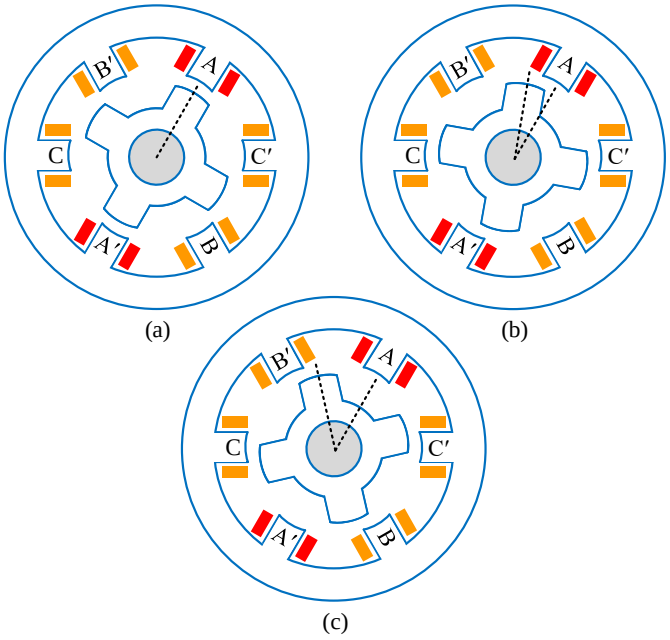

Figure 2.3: Different rotor positions of 3-phase 6/4 SRM with respect to the phase-A (a) aligned position, (b) mid-aligned position, and (b) unaligned position [1].

the phase inductance profile follows a similar pattern to that of the flux linkage. A high phase inductance exists at the aligned position since the flux path reluctance is minimum. The inductance drops as the rotor moves from the aligned position

to the unaligned position since the reluctance increases. Typically, in an SRM, the mutual flux between phases is small, and it can be ignored. Hence, the magnetic characteristics of one phase can be used to analyze the electromagnetic performance of a conventional SRM [1].

The phase voltage v_j of an SRM can be expressed as [6, 27]

$$v_j = R_j i_j + \frac{\mathrm{d}\psi_j}{\mathrm{d}t};\ (j = A, B, C...). \tag{2.2.1}$$

It can be considered that the SRM has linear magnetic characteristics while neglecting the magnetic saturation in iron. Thus, ψ_j is expressed in terms of phase inductance $L_j(\theta_r)$ and i_j

$$\psi_j = L_j(\theta_r) i_j. \tag{2.2.2}$$

From (2.2.1) and (2.2.2)

$$v_j = R_j i_j + L_j \frac{\mathrm{d}i_j}{\mathrm{d}t} + i_j \frac{\mathrm{d}L_j}{\mathrm{d}t}. \tag{2.2.3}$$

Muliplying both sides of (2.2.3) by i_j and re-arranging:

$$v_j i_j = i_j^2 R_j + \frac{\mathrm{d}}{\mathrm{d}t}\big[\frac{1}{2} L_j i_j^2\big] + \frac{1}{2} i_j^2 \frac{\mathrm{d}L_j}{\mathrm{d}\theta_r}\omega_r. \tag{2.2.4}$$

where terms $v_j i_j$, $i_j^2 R_j$, $\frac{d}{dt}\big[\frac{1}{2} L_j(\theta_r) i_j^2\big]$ and $\frac{1}{2} i_j^2 \frac{dL_j}{d\theta_r}\omega_r$ are the input electrical power, copper loss, rate of change of stored magnetic energy and airgap power [6]. The airgap poweris modeled as the torque generating part in an SRM. Hence, the phase

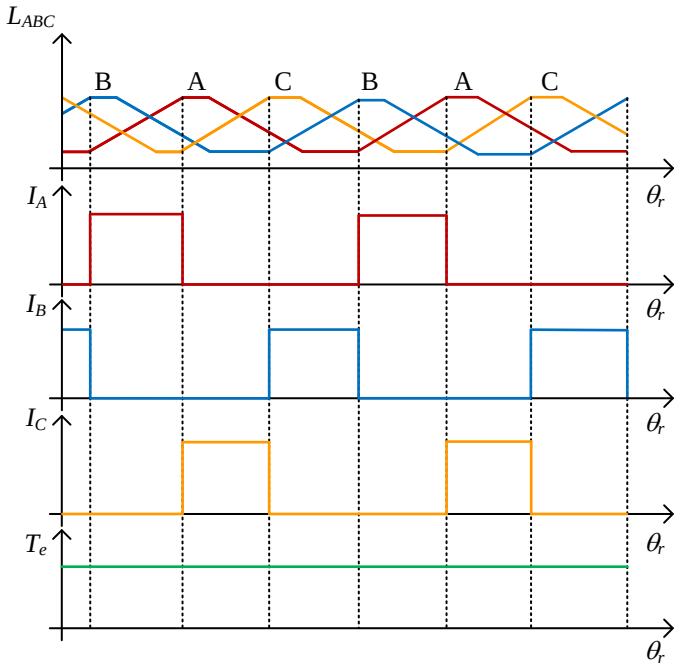

Figure 2.4: Continuous torque production in linear case of a 3-phase SRM.

electromagnetic torque of an ideal SRM can be written as

$$T_{e,j} = \frac{1}{2} i_j^2 \frac{\mathrm{d}L_j}{\mathrm{d}\theta_r}. \tag{2.2.5}$$

According to (2.2.5), the phase should be energized at the positive slope region of the inductance curve in Fig. 2.2 to produce motoring torque. Besides, the torque production is independent of the direction of the current. The phase excitation for continuous torque production of a 3-phase 6/4 SRM in Fig. 2.3 for linear case is shown in Fig. 2.4. Counter-clockwise (CCW) rotation is achieved by exciting the phases in A-C-B sequence.

Considering the magnetic saturation in iron, the relationship between ψ_j and i_j is shown in Fig. 2.5 [6, 27]. The magnetic energy W_f and co-energy W_c per phase can

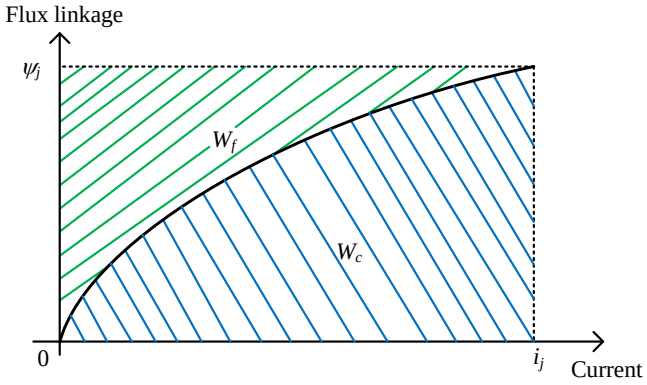

Figure 2.5: The phase flux linkage vs current characteristics with magnetic saturation of an SRM.

be calculated as

$$W_f = \int i_j d\psi_j. \tag{2.2.6}$$

$$W_c = \int \psi_j di_j. \tag{2.2.7}$$

From Fig. 2.5:

$$W_c = \psi_j i_j - W_f. \tag{2.2.8}$$

From energy balance, the input electrical energy W_e can be written as

$$W_e = W_f + W_{mech}. \tag{2.2.9}$$

Hence, the change in the input electrical energy can be derived as

$$dW_e = dW_f + dW_{mech} = dW_f + T_{e,j} d\theta_r. \tag{2.2.10}$$

From Faraday's law, the magnitude of the induced voltage e_j can be written as

$$e_j = \frac{\mathrm{d}\psi_j}{\mathrm{d}t}. \tag{2.2.11}$$

The change in the input electrical energy dW_e can be expressed as

$$dW_e = e_j i_j dt. \tag{2.2.12}$$

From (2.2.10) and (2.2.12),

$$e_j i_j dt = dW_f + T_{e,j} d\theta_r \tag{2.2.13}$$

From (2.2.13) and (2.2.11), the change in the stored magnetic energy can be expressed as

$$dW_f = i_j d\psi_j - T_{e,j} d\theta_r = \left.\frac{\partial W_f}{\partial \psi_j}\right|_{\theta_r = const.} d\psi_j + \left.\frac{\partial W_f}{\partial \theta_r}\right|_{\psi_j = const.} d\theta_r. \tag{2.2.14}$$

Therefore, electromagnetic torque can be calculated by

$$T_{e,j} = -\left.\frac{\partial W_f}{\partial \theta_r}\right|_{\psi_j = const.}. \tag{2.2.15}$$

According to the (2.2.15), the electromagnetic torque can be calculated by differentiation of magnetic energy with respect to the rotor position by keeping the flux linkage constant. Alternatively, the electromagnetic torque can be calculated using the co-energy. From (2.2.8), change in the co-energy can be expressed as

$$dW_c = d(\psi_j i_j) - dW_f. \tag{2.2.16}$$

From (2.2.14) and (2.2.16)

$$dW_c = \psi_j di_j + T_{e,j} d\theta_r = \left.\frac{\partial W_c}{\partial i_j}\right|_{\theta_r = const.} di_j + \left.\frac{\partial W_c}{\partial \theta_r}\right|_{i_j = const.} d\theta_r. \tag{2.2.17}$$

Hence,

$$T_{e,j} = \left.\frac{\partial W_c}{\partial \theta_r}\right|_{i_j = const.}. \tag{2.2.18}$$

According to the (2.2.18), electromagnetic torque can be calculated by differentiating co-energy with respect to the rotor position while keeping the current constant.

2.3 SRM Configurations and Windings

A possible classification of various types of SRMs are shown in Fig. 2.6 [27]. SRMs can be divided into two categories based on the type of motion of the rotor according to Fig. 2.6. In Rotary SRMs, the rotor rotates around the axis of the shaft. Linear SRMs have linear geometry, and the rotor performs translational motion. The rotary SRMs can be further classified into radial flux SRMs and axial flux SRMs. In radial

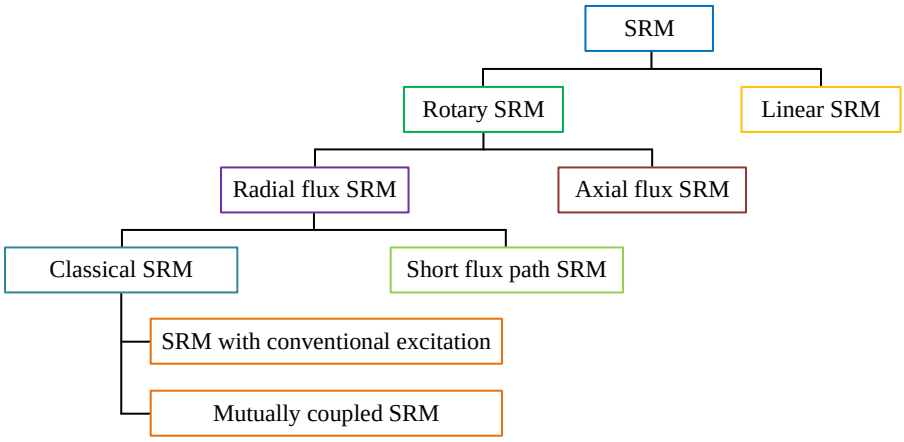

Figure 2.6: Classification of SRMs.

flux SRM, airgap flux is orthogonal to the shaft. The airgap flux is parallel to the shaft in axial flux SRMs. There are mainly two types of radial flux SRMs based on the nature of the geometry. The classical radial flux SRMs have doubly salient geometry as shown in Fig. 2.1 and Fig. 2.3. Short flux path SRMs have asymmetric stator geometry, and a shorter flux path is achieved by connecting two adjacent coils to make a pole pair [27]. The classical SRMs can be further classified as SRMs with conventional excitation and mutually coupled SRMs. In SRMs with conventional excitation, the torque is produced mainly by single-phase excitation and rate of change of self-inductance. The torque in the mutually coupled SRMs is generated by multi-phase excitation and rate of change of self and mutual inductances. Only SRMs with conventional excitation are considered in this thesis and they are referred as SRMs in the rest of the thesis.

2.3.1 Pole Configurations

In an SRM, one electrical cycle is completed when a rotor pole moves one rotor pole pitch from the aligned position. Therefore, the relationship between electrical frequency f_{elec} and mechanical frequency f_{mech} can be defined as

$$f_{elec} = N_r f_{mech}. \tag{2.3.1}$$

All stator poles in the same phase generate the same electromagnetic torque. The remaining phases produce the same torque with a phase shift. Torque pulsations occur during the current transition from one phase to the other phase. The total

number of torque pulsations or number of strokes can be defined by

$$T_{pulse} = mN_r. \tag{2.3.2}$$

The number of rotor poles in an SRM configuration is defined based on the number of stator poles. The magnetic poles are created by the flux linking to the excited phase coils. To obtain a balance configuration, the number of stator poles should be chosen to have an even number of magnetic pole pairs per phase. The relationship between the number of stator and rotor poles is given by [6]

$$k_{id}N_s = mN_r. \tag{2.3.3}$$

The variable k_{id} is an integer and should not be an integer multiplier of prime factors of m.

2.3.2 Windings

Concentrated windings are mostly utilized in SRMs due to their inherent advantages, such as i) high torque density, ii) high slot fill factor, and iii) short-end windings. Single-layer (SL) or double-layer (DL) windings are possible for a concentrated winding conventional SRM [28]. DL windings are mostly used since it utilizes the stator poles effectively. An example for DL concentrated winding for a 3-phase 12/16 SRM is shown in Fig. 2.7. There are two possible configurations for DL concentrated winding. First configuration has 120° phase spread and second configuration has 60° phase spread as shown in Fig. 2.8. According to Fig. 2.8 (a) and (b), 120° phase spread configuration has shorter flux path during the phase commutation and

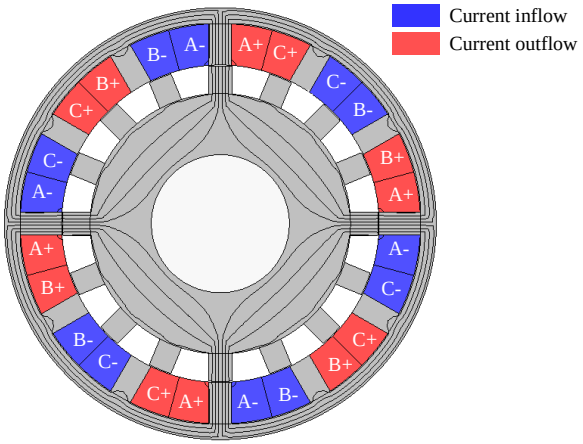

Figure 2.7: Flux pattern in the 3-phase 12/16 SRM at the aligned position for double-layer (DL) concentrated winding.

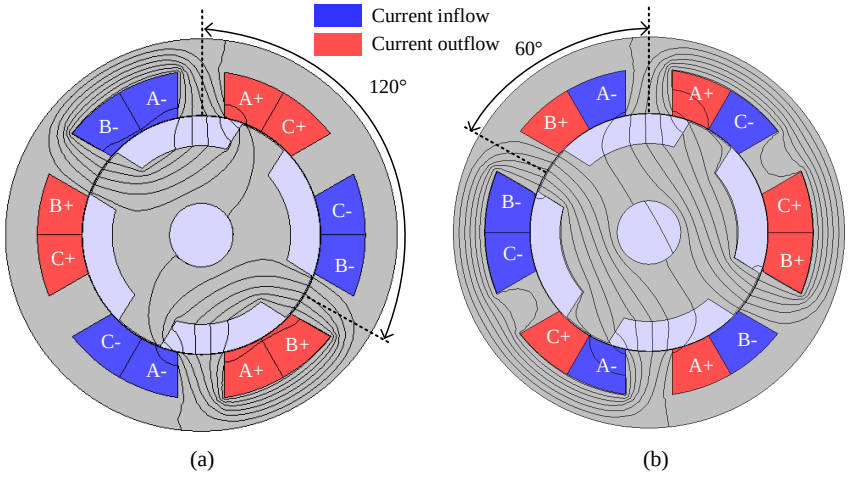

Figure 2.8: Flux pattern in the 3-phase DL concentrated winding 6/4 SRM during the phase commutation from phase-B to phase-A for (a) 120° phase spread and (b) 60° phase spread.

60° phase spread configuration has longer flux path. Therefore, with the 120° phase spread configuration can expect lower core losses.

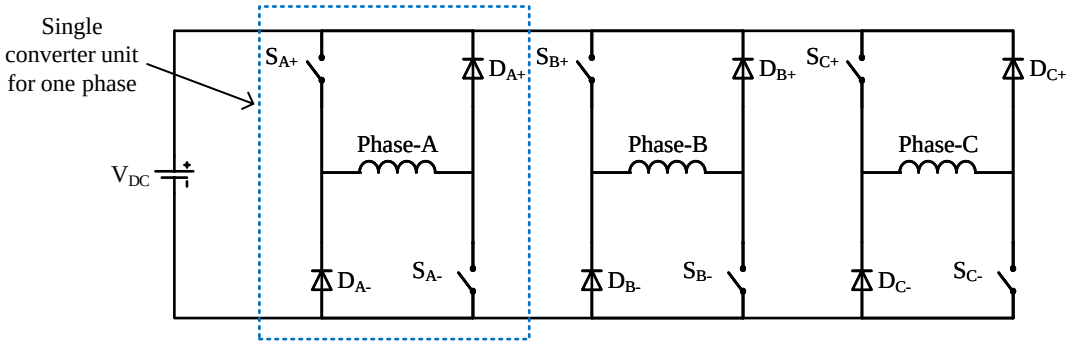

Figure 2.9: Asymmetric bridege converter for a 3-phase SRM.

2.4 SRM Drives

2.4.1 Asymmetric Bridge Converter

The asymmetric bridge converter shown in Fig. 2.9 is widely used to operate conventional SRMs. The converter shown in Fig. 2.9 is for a 3-phase SRM. The phases are independantly controlled in an SRM. Therefore, the single converter unit in Fig. 2.9 can be repeated to create the asymmetric brdige converter according to the number of phases available. The phases are energized/de-energized by connecting the V_{DC} using the switches S_{A+}, S_{A-}, S_{B+}, S_{B-}, S_{C+}, S_{C-}. Usually, the phase current is unidirectional in conventional SRMs. As shown in Fig. 2.10, there are three operating modes for each single converter unit [6]. In phase energizing mode, S_{j+} and S_{j-} are turned on, and positive V_{DC} is applied to the phase-j. Negative V_{DC} can be applied to phase-A by turning off S_{j+} and S_{j-} which results in de-energizing the phase-j. Switch S_{j-} is turned on, and S_{j+} is turned off during the freewheeling mode that applies zero voltage to the phase coil. In all three operating modes, the current flows in the same direction through the coils.

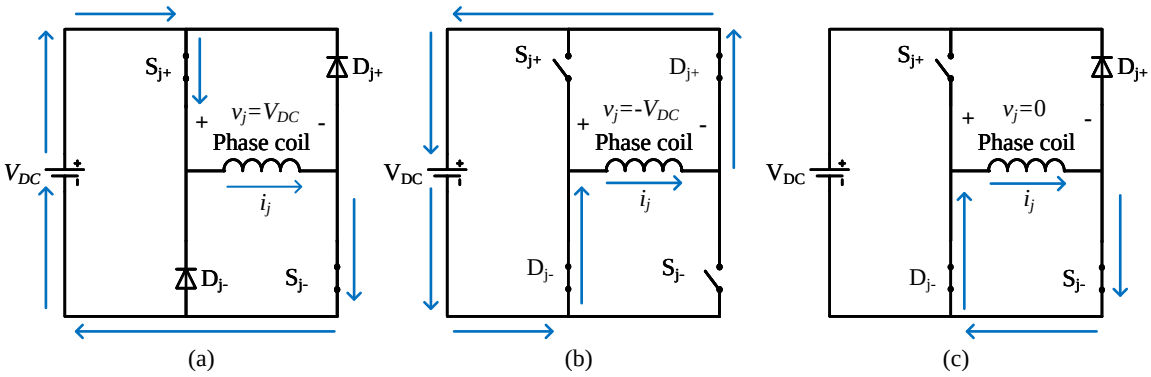

Figure 2.10: Operating modes of the asymmetric bridge converter (a) phase energizing mode, (b) phase de-energizing mode, and (c) freewheeling mode.

2.4.2 Current Control

Hysteresis current controllers are primarily used to regulate the phase currents. The reference current is compared against the measured current and the hysteresis current controller issues the phase excitation signals to the switches to regulate the phase current at the given reference. The hard switching or soft switching techniques can be applied for current chopping for regulating the current [6]. In hard switching, only the phase energizing mode and phase de-energizing mode are utilized to control the current, as shown in Fig. 2.11 (a). According to Fig. 2.11 (b), all three operating modes of the asymmetric bride converter are utilized in soft switching.

2.5 Summary

The construction and operational principle of an SRM were discussed in this chapter. Classifications of SRMs under the type of motion, flux pattern, and geometry structure were discussed. The pole configurations and windings of conventional SRMs have been analyzed. The Asymmetric bridge converter was introduced, and its main

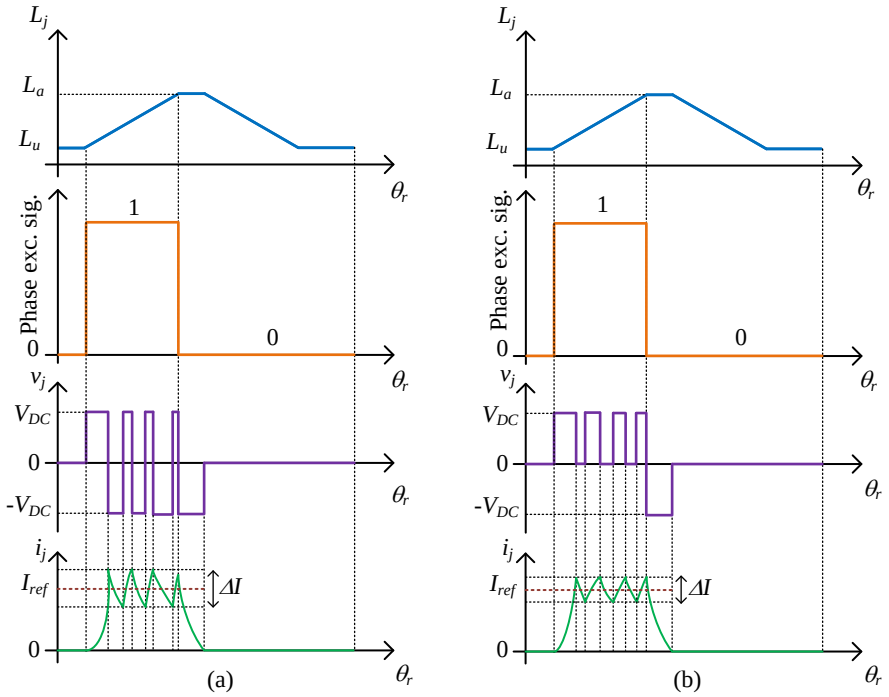

Figure 2.11: Hysteresis current control (a) hard switching and (b) soft switching.

operating modes have been discussed. The hard and soft switching techniques used in the hysteresis current control have also been explained.

Chapter 3

Electromagnetic Modeling Techniques of SRMs

3.1 Introduction

Design and analysis of electric machines require an electromagnetic model. The model provides various key electromagnetic performance characteristics such as magnetic flux density, magnetic field intensity, induced electromotive force, and electromagnetic torque. The model could also estimate the machine losses such as AC copper loss, hysteresis loss, and eddy-current loss. In addition, it could be utilized within an optimization process to achieve different objectives such as to minimize the torque ripple [29], maximize the efficiency, and minimize the motor weight [30]. Moreover, it helps in the design of the motor drive system [31, 32].

This chapter investigates various electromagnetic modeling techniques for SRMs. Analytical, numerical, and hybrid models are considered. The work investigates analytical models that are based on Maxwell's equations in addition to interpolation and

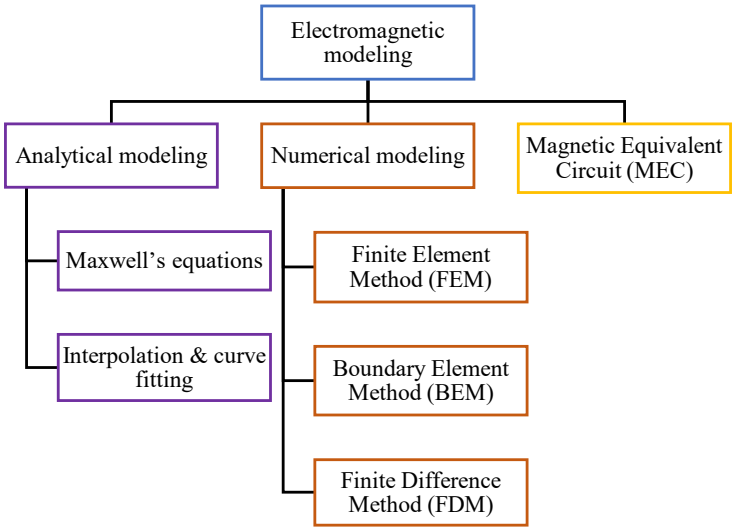

Figure 3.1: Electromagnetic modeling techniques of electric machines.

curve fitting techniques. Numerical techniques such as FEM and boundary element method (BEM) are studied. Finally, MEC method is discussed [9, 10].

3.2 Modeling Techniques for Electrical Machines

Electromagnetic modeling of electric machines can be divided into two main categories (i) analytical modeling and (ii) numerical modeling. Each category comprises sub-categories as shown in Fig. 3.1 [10]. Analytical techniques have major challenges in approximating a complex geometry, considering core saturation, calculating the hysteresis and eddy current losses in the core, modeling the skin and proximity effects in the winding, and modeling the end-winding inductance [10, 33]. However, analytical models are computationally cheap compared to numerical models [10]. The most common analytical models are based on Maxwell's equations or interpolation and

curve fitting techniques. In Maxwell's-equations-based models, the differential equations are analytically solved by neglecting the local saturation, the effect of mutual coupling, and leakage flux. This reduces the model accuracy [34, 35]. The Maxwell's equations based analytical models are preferred in initial design stages to estimate the main design parameters [36, 37]. The interpolation- and curve-fitting-based techniques are another approach to model SRMs. They include experimental or Finite Element (FE) model data to develop the model. However, new data is required if the machine geometry changes. Thus, these models are more suitable for designing the controllers of motor drive systems.

Various numerical techniques are utilized in modeling electric machines such as FEM, BEM, and Finite Difference Method (FDM). FEM is the most common numerical technique due to its high accuracy [38, 39]. It can accurately estimate various electromagnetic characteristics considering complex geometries and nonlinearity of the core materials, where the material relative permeability depends on the magnetic flux density [38]. In [38], the FEM was utilized to solve low frequency saturable electromagnetic field problems. A 2D FE model was introduced in [38] and [39] to calculate the electromagnetic fields in electric machines. FEM is currently utilized to model complex geometries of electric machines considering skin, and proximity effects, and 3-dimensional (3D) effects. It also helps estimating the machine losses. However, the FE models have high computational cost and, depending on the complexity of the problem, the simulation time might takes hours to finish. BEM can be utilized as an alternative to FEM, since it introduces less computational burden. The problem domain is reduced from 3D to 2D in BEM [9]. However, BEM is difficult to apply to solve saturable electromagnetic fields since the coefficient matrices are not

symmetric, not positive definite and completely populated [39, 40]. FDM is another option to model electric machines. However, it has difficulties in modeling complex geometries; therefore, it is not directly applied to model electric machines [39].

The MEC modeling is a popular method in modeling electric machines [10]. It is a special case since it can be considered as an analytical or a numerical technique according to how it is applied. It is considered as an analytical technique if it is combined with other analytical modeling techniques such as Maxwell's equations [41, 42]. When the nonlinearity of the magnetic materials is considered, the MEC modeling has to be combined with numerical techniques [13]. In [13], the MEC method was applied to calculate the magnetic flux in toroidal-core and C-core magnetic devices. The method has been applied in [13] to model magnetic devices with moving parts.

In the MEC method, an electric circuit model is developed to analyze the magnetic characteristics of a system by utilizing the analogy between magnetic and electric circuits presented in Table 3.1. A simple magnetic device that comprises a toroid with two air gaps is illustrated in Fig. 3.2 (a). The corresponding MEC is shown in Fig. 3.2 (b). The MEC in Fig. 3.2 (b) has four reluctances: two reluctances for the core parts (R_{c1}, R_{c2}) and two reluctances for the airgaps (R_{g1}, R_{g2}). The flux flow in the toroid and airgaps can be considered similar neglecting the leakage flux. The magnetomotive force (MMF) source is calculated by multiplying the winding turns N and the excitation current I. The MEC technique can be improved to model the saturation, leakage flux, and various electromagnetic losses with fair accuracy compared to FEM [10]. The model accuracy increases by adding more reluctance elements. However, this increases the model complexity [13]. Narrowing the discussion from electric machines to SRMs, the modeling techniques can still be categorized according to

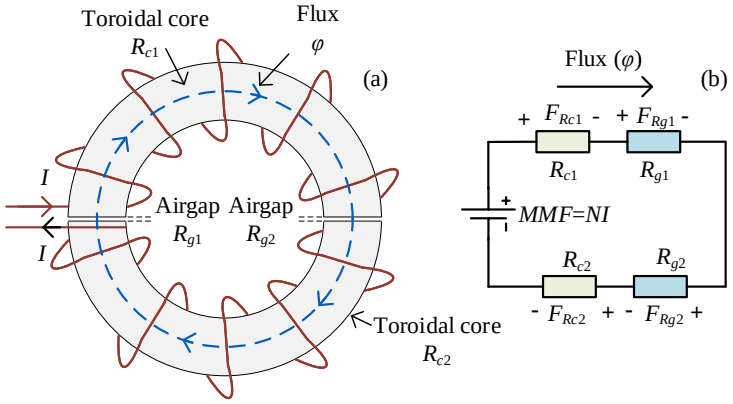

Figure 3.2: (a) A toroidal core and (b) the corresponding MEC.

the previous classification [9, 43]. The main objective of electromagnetic modeling of SRMs is to obtain the machine phase flux linkage as a function of the stator current and rotor position [9]. Then, other electromagnetic characteristics can be predicted using (2.2.1), (2.2.7) and (2.2.18).

Table 3.1: Analogy between magnetic and electric circuits

Type of the circuit		
Quantity	Magnetic circuit	Electric circuit
Flux/Current density	$\vec{B}$	$\vec{J}$
Field intensity	$\vec{H}$	$\vec{E}$
Permeability/Conductivity	μ	σ
Reluctivity/Resistivity	ν	ρ
Reluctance/Resistance	R_{mag}	R_{elec}
Flux/Current	ϕ	I
Magnetomotive/Electromotive force	F	E
Magnetic/Electric potential	U	V
Hopkinson's/Ohm's law	$F = \phi R_{mag}$	$V = IR_{elec}$
Magnetic/Electric energy	$F\Phi$	VI

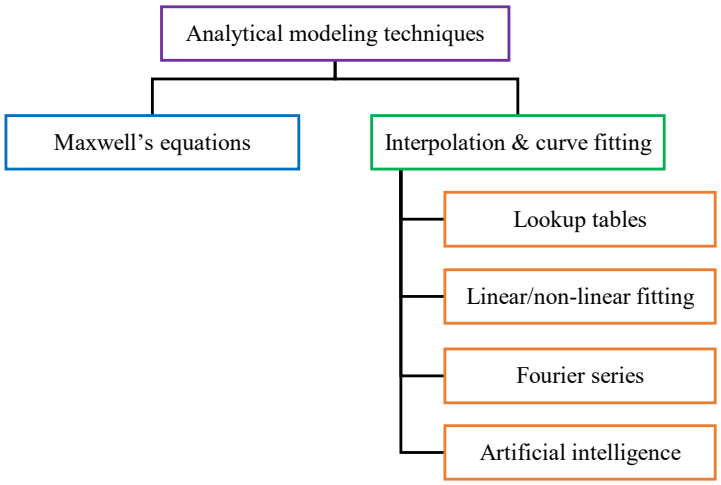

Figure 3.3: Various types of analytical methods for SRM modeling.

Modeling of SRMs is challenging due to many reasons. The phase flux linkage is a nonlinear function of the rotor position and the stator excitation current [9, 44], and the machine commonly works in a saturated condition. Moreover, the airgap periphery is irregular due to the doubly-salient structure of the machine. Hence, various modeling techniques can be applied to SRMs.

3.3 Analytical Modeling Techniques For SRMs

Analytical modeling techniques, shown in Fig. 3.1, can be extended further as shown in Fig. 3.3. The interpolation-and-curve-fitting-based techniques are divided into four subcategories, where they rely on lookup tables, linear/nonlinear curve fitting, Fourier series, or artificial intelligence.

3.3.1 Maxwell's-Equations-Based Methods

The partial differential equations, formulated using Maxwell's equations, are solved using analytical methods. The magnetic vector potential or magnetic scalar potential inside the SRM boundary is determined by solving these differential equations [38]. Poisson's equation of magnetic vector potential $\vec{A}$ is

$$\nabla^2 \vec{A} = -\mu \vec{J}. \tag{3.3.1}$$

Equation (3.3.1) is derived assuming the material is isotropic and linear. Therefore, the permeability of the material does not depend on the flux density, and has no spatial variation. Alternatively, the magnetic field can be solved by using magnetic scalar potential U under the same assumptions [39, 45]. Poisson's equation of U can be obtained as

$$\nabla^2 U = \nabla \cdot \vec{T}. \tag{3.3.2}$$

The equations (3.3.1) [46] or (3.3.2) [39,47] can be solved analytically as a Boundary Value Problem (BVP) to calculate the magnetic vector potential or magnetic scalar potential. There are several ways to solve this BVP. The most common approaches are variable separable method [46, 48] and conformal mapping [47, 49–51].

As shown in Fig. 3.4, the circular geometry of the SRM can be approximated as 2D unwrapped rectangular shape in the x-y plane. However, this approximation can introduce errors due to inconsistency in the geometry. These modeling errors in the calculation of the magnetic field of an SRM can be reduced by solving the Poison or Laplace equation in the cylindrical domain as shown in Fig. 3.5. A major assumption in the field calculation is that an infinite permeability is considered for the iron core.

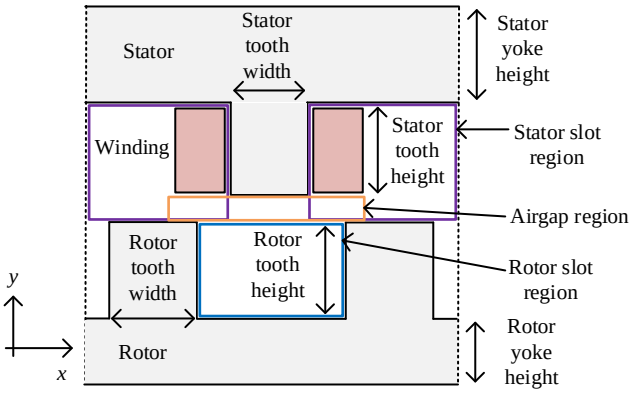

Figure 3.4: Formulation of a rectangular-shaped Boundary Value Problem (BVP) by unwrapping the circular SRM shape.

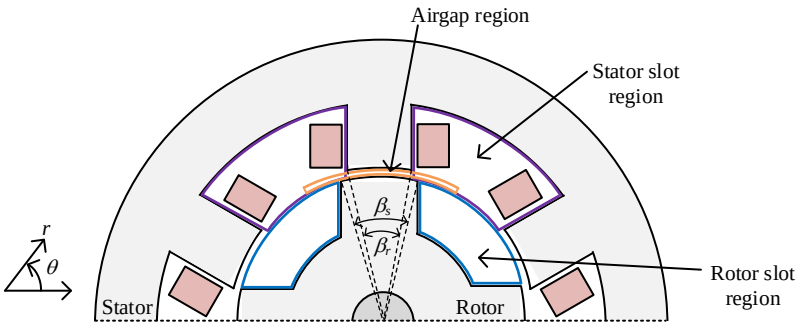

Figure 3.5: Formulation of a circular-shaped BVP for SRM.

Thus, $\vec{H}$ field inside the stator and rotor core becomes zero. The geometry inside the air region can be divided into three parts as in Fig. 3.4 and Fig. 3.5: Airgap region, stator slot region, and rotor slot region [52]. The vector $\vec{T}$ in the rotor slots and airgap regions is zero due to zero current density in these regions. Hence, (3.3.2) transforms to a Laplace equation and the variable separable method can be applied within the boundaries as shown in Fig. 3.4 and Fig. 3.5 to calculate U. The magnetic field inside the stator slot region can be calculated by solving (3.3.1) using the variable separable method inside the defined boundaries in Fig. 3.4 and Fig. 3.5 [46].

In conformal mapping technique, the Schwartz-Christoffel (SC) transformation

is applied to transform a complicated geometry into a simple one, which makes the magnetic field calculation easier [47,49,50,53]. This technique was applied to calculate the airgap magnetic field [49] of SRMs. The transformation process is illustrated in Fig. 3.6 [49, 53]. The circular geometry of the SRM is represented in the complex z-plane. Then, a logarithmic Conformal mapping (CM) is applied to transform the geometry from the z-plane to the w-plane. This results in a rectangular shape SRM geometry with trapezoidal shape stator and rotor poles. The SC transformation is applied again to transform the geometry from the w-plane to the S-plane, which results in a canonical rectangular shape. Finally, an exponential CM is applied again to transform the geometry from the S-plane to the T-plane, which results in an annular shape. The solution of the magnetic field $\vec{H}_{ag,T}(x, y)$ in the airgap in the T-plane is obtained by Hague's equation [49]. Once $\vec{H}_{ag,T}(x, y)$ is calculated, the inverse transformations are applied to obtain the electromagnetic field in the airgap in the z-plane. The SC techniques is highly accurate in the linear regions of the magnetic materials and useful for analyzing the 2D electromagnetic characteristics of SRMs. However, this technique cannot be applied for 3D modeling and, with this method, it is more challenging to take the local saturation into account.

3.3.2 Interpolation- and curve-fitting-based Methods

These methods are popular in the design and development of SRM drives [54]. Phase flux linkage/inductance and torque characteristics as functions of the rotor position and the stator current are necessary to develop the models. Numerical simulation data, mostly based on finite element analysis (FEA) or experimental results are utilized [9]. The phase flux linkage of SRMs can be estimated experimentally at different

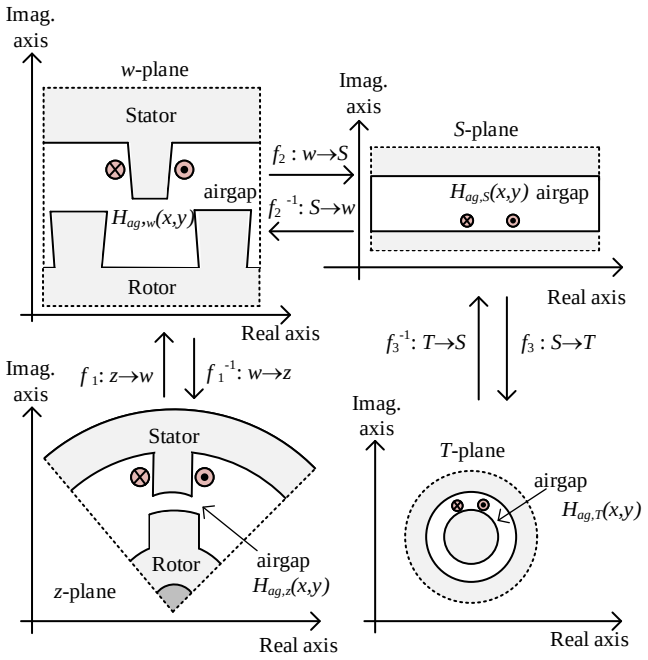

Figure 3.6: Schwarz-Christoffel transformation of SRM domain.

rotor positions and different excitation currents [55–59]. The flux linkage is the integral of the machine electromotive force (EMF) which is estimated based on the measured winding resistance, current, and voltage. The torque can be measured using a torque sensor or estimated by applying (2.2.1), (2.2.7) and (2.2.18) to the mentioned measurements. FE simulations can also be used to obtain the flux linkage and torque characteristics. Preparing the experimental or the FE data takes significant time, and the developed model will be valid only for the given geometry and the configuration.

The flux linkage and torque data can be used in the form of look-up tables (LUTs), linear/nonlinear curve-fitting formulas, Fourier series, and artificial intelligence (AI) [54, 60].

Look-up tables

This technique is simple to implement with good accuracy using tools such as MATLAB, OCTAVE, and Compose and Activate by Altair [57, 58, 61, 62]. The machine phase flux linkage/inductance and torque characteristics at different stator currents and different rotor positions are saved in 2D lookup tables. The torque and flux linkage/inductance values in the model are then obtained based on the input rotor position and excitation. Interpolation is applied between the existing data. Lookup tables developed by running FEM simulations of an 8/6 SRM model are illustrated in Fig. 3.7.

Linear/nonlinear curve-fitting formulas

In this technique, the formulas of the machine phase inductance/flux linkage and torque are utilized as functions of the rotor position and stator current [63]. The least square technique is applied to fit the simulation or experimental data to these

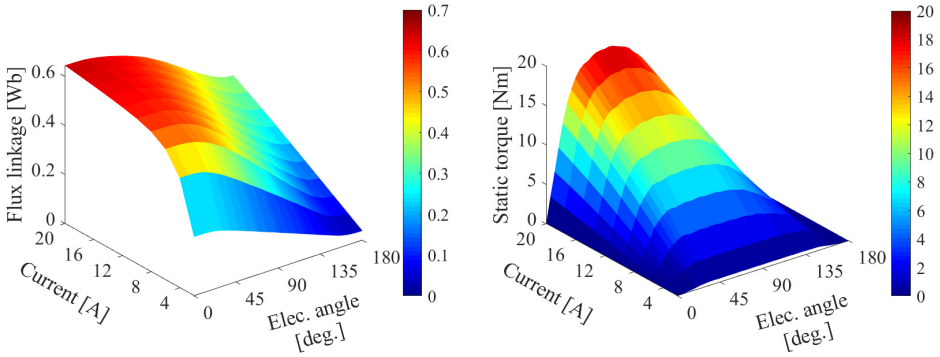

(a) (b)

Figure 3.7: SRM lookup tables obtained form finite element (FE) simulations (a) flux linkage versus rotor position and current and (b) torque versus rotor position and current.

formulas. The phase inductance profile, as an example, can be simply approximated as a piecewise linear function [64]

$$L_j(\theta_r) = \begin{cases} L_a & ; 0 \leq \theta_r \leq \alpha_1 \\ L_a - K_{au}(\theta_r - \alpha_1) & ; \alpha_1 \leq \theta_r \leq \alpha_2 \\ L_u & ; \alpha_2 \leq \theta_r \leq \frac{2\pi}{N_r} - \alpha_2 \\ L_a + K_{au}(\theta_r - \frac{2\pi}{N_r} + \alpha_1) & ; \frac{2\pi}{N_r} - \alpha_2 \leq \theta_r \leq \frac{2\pi}{N_r} \end{cases} \tag{3.3.3}$$

where the constant K_{au} is given by $(L_a - L_u)/\beta_s$. The L_a is the inductance at the aligned position and L_u is the minimum inductance at unaligned position. The angles α_1 and α_2 were shown in Fig. 2.2. Fig. 3.8 shows an SRM inductance profile developed using (3.3.3) and using FEM. Although the approximation is reasonable, there is some difference between the two profiles. The linear inductance profile in Fig. 3.8 is developed for a 8/6 SRM. The FE model of the 8/6 SRM is developed using ANSYS Maxwell software.

Similarly, the flux linkage versus current profile can be approximated as linear

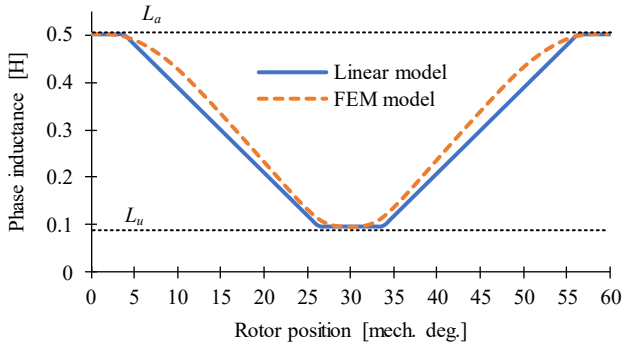

Figure 3.8: Inductance profile of an 8/6 SRM developed using piecewise linear function and finite element method (FEM).

piecewise functions [64,65]. Different piecewise functions can be developed at different rotor position ranges. Piecewise nonlinear functions [66–68] such as parabolic function [68] can also be applied. The flux linkage versus current characteristic at the aligned and unaligned rotor positions can be approximated as [68]

$$\psi_j(i_j) = \begin{cases} L_u i_{ph} & ; \text{unaligned} \\ L_{a,0} i_{ph} & ; \text{aligned } (i_j \leq i_s) \\ \psi_0 + \sqrt{4a_s(i_j - i_0)} & ; \text{aligned } (i_j > i_s) \end{cases} \tag{3.3.4}$$

where a_s, ψ_0, and i_0 are constants that are determined using simulation or experimental data. The flux linkage profile is linear at the unaligned position. However, for the aligned position, a linear flux linkage can be considered only up to a certain excitation current i_s [68]. Therefore, $L_{a,0}$ is the inductance at the aligned position when $(i_j \leq i_s)$. The flux linkage is nonlinear when $(i \geq i_s)$, as shown in Fig. 3.9. The representation matched the FEM profile well at the unaligned position, whereas there are some discrepancies at the aligned position. The same 8/6 SRM is utilized in here to obtain the flux linkage profiles in Fig. 3.9. Alternatively, various 2D polynomials such as bivariate polynomials and bi-cubic spline polynomials can be utilized to model the flux linkage and torque characteristics of an SRM [69, 70]. Curve fitting techniques based on off-line and online least square method can be used to determine the coefficients of the polynomials [69]. A 2D orthogonal polynomial of the flux linkage as a function of the rotor position and the stator current is expressed as [69]

$$\psi_j(i_j, \theta_r) = \sum_{m=0}^{k-1} \sum_{n=0}^{r-1} a_{mn} (\theta_r - \bar{\theta})^m (i_j - \bar{i})^n \tag{3.3.5}$$

where a_{mn} is a constant. k and r are positive integers such that $k \times r$ equals the number of available data points. The parameters $\bar{\theta}$ and $\bar{i}$ are the mean values of the rotor position data and current data, respectively [71]. Additionally, other nonlinear functions such as Gaussian functions [72], piecewise Frohlich functions [73], and exponential functions [71, 74, 75] could be utilized to approximate the flux linkage profiles.

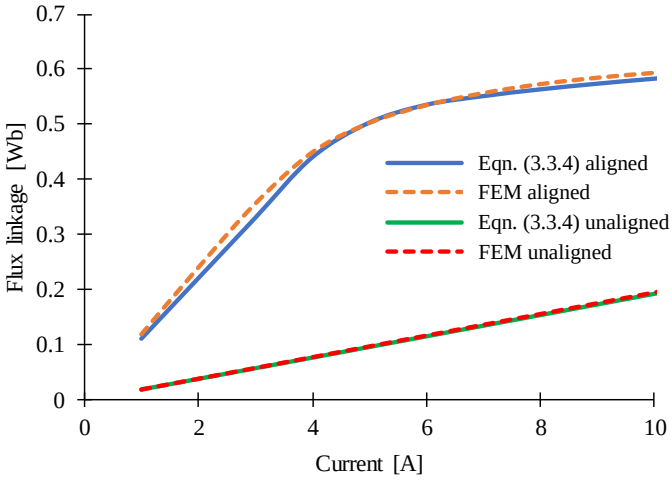

Figure 3.9: Comparison of the flux linkage profile of an 8/6 SRM developed using the nonlinear function in (3.3.4) against FEM.

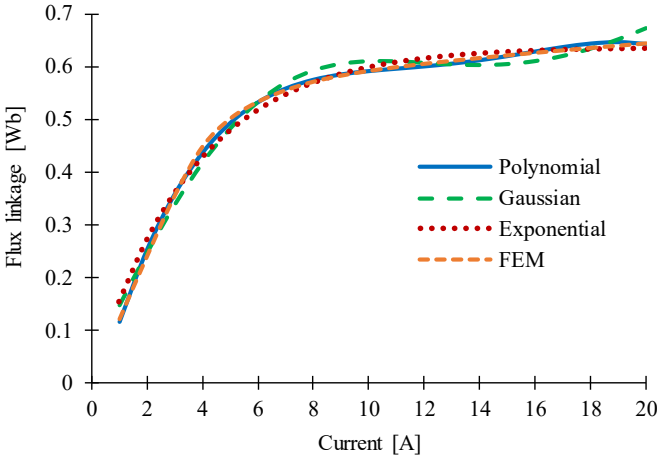

Figure 3.10: Comparison of different curve fitting techniques for modeling flux linkage characteristics of an 8/6 SRM.

Fig. 3.10 shows the developed flux linkage profiles using 2D orthonormal polynomial [69], Gaussian function [72], and exponential function [71]. The profiles are compared with that obtained using the FEM model of the same 8/6 SRM. Table 3.2 shows the root-mean-squared-error (RMSE) of the flux linkage profiles obtained from nonlinear curve-fitting formulas with respect to FEM results at the aligned position. The orthonormal-polynomial representation has the lowest RMSE.

Fourier Series

Fourier decomposition method can be utilized to represent the machine phase flux linkage/inductance and torque profiles as functions of the stator current and rotor position. It has been extensively applied to SRM modeling [76–84]. Considering that an infinite series is not practical, the number of terms is mostly limited between two and four. The accuracy increases as the number of terms increases. The models developed based on Fourier series method can be adaptable to parameter variations due to various losses in SRM, aging, and manufacturing defects [76]. Therefore, these models can be more suitable for controller design in SRM. The inductance profile $L_j(i_j, \theta_r)$ as a function of the rotor position and stator current can be expanded using

Table 3.2: Root-mean-squared-error (RMSE) comparison between interpolation- and curve-fitting techniques with respect to FEM results

Modeling technique	RMSE
Eqn. (3.3.4)	3.34%
Polynomial	1.67%
Gaussian	5.84%
Exponential	7.33%

Fourier series as follows [79]

$$L_j(i_j, \theta_r) = \sum_{n=0}^{k_t} L_{j,n}(i_j) cos(n(N_r\theta_r + \delta_n)) \tag{3.3.6}$$

where $L_{j,n}(i_j)$, δ_n, and k_t are the n^{th} Fourier coefficient, phase angle of each Fourier component, and the series truncation level, respectively. The flux linkage profile versus rotor position developed using (3.3.6) is compared with the FE model of the 8/6 SRM in Fig. 3.11. There is significant difference between the profiles if only two terms are considered in the Fourier series. The representation is significantly improved when a third term is added. 2D Fourier series can also be utilized to represent the flux linkage characteristics. The phase flux linkage can be expanded as a 2D Fourier series in exponential form [78].

The Fourier coefficients in (3.3.6) can be determined using FEA [78, 84], experimental [77] or analytical [76, 79–81, 83] techniques. As an example, various analytical techniques such as assuming ideal inductance profile with weighting functions [76, 82],

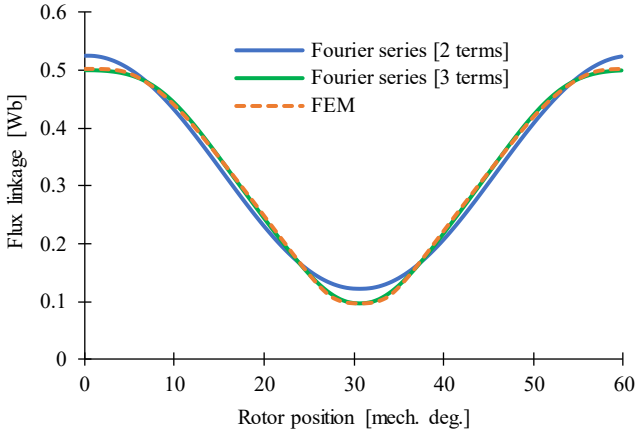

Figure 3.11: Flux linkage profile versus rotor position developed using Fourier series, eqn. (3.3.6), and FEM for the 8/6 SRM.

on-line parameter identification techniques [79,81], polynomial approximations [79,80] and field reconstruction technique [83] can be applied to determine the Fourier coefficients.

Artificial Intelligence

A learning algorithm can be developed to obtain the flux linkage and torque characteristics of an SRM as functions of rotor position and stator current. The artificial neural network (ANN) [85–91] and machine learning (ML) [92, 93] techniques can be applied to develop this learning algorithm. The key advantage of these techniques is the capability of adapting to parameter variations of the machine due to losses, aging and manufacturing tolerances [85].

ANN has basically three types of layers: input layers, output layers, and hidden layers. Each layer comprises different tiers, which can be considered as a piece of intelligence. The learning rules and algorithms are defined in these tiers. They need to be trained properly to process the given raw data. In case of SRM modeling, there are two main inputs which are the stator current and the rotor position. These inputs pass through the hidden layers. This data is then processed as flux linkage and torque outputs. The concept is illustrated in Fig. 3.12. The four-layer network consists of one input layer, two hidden layers and one output layer. The input layer has two tiers to take the stator current and rotor position. Each hidden layer consists of four tiers whereas the output layer has two tiers. Various neural networks can be identified based on the way of processing the data in each tier. Recurrent neural networks (RNN) [85] and radial basis function (RBF) neural networks [90] are more popular in SRM modeling. The learning techniques are applied to train the neural networks.

This is necessary such that the network functions properly. There are various learning techniques that have been applied in SRM modeling such as back-propagation algorithm [86], B-spline neural network [87], cascade-forward-backpropagation neural network (CFNN) [88], general regression neural network (GRNN) [89], Fuzzy clustering [90], and hybrid adaptive neural fuzzy inference system (ANFIS) [91]. Artificial intelligence provides models with high accuracy but it requires large number of data points to train the network. The large data set requirement causes over-fitting [92]; i.e. the accuracy of the fitted model is high within the given data set and low outside. ML techniques address this issue [92, 93]. They are developed based on the statistics theory [92]. The most popular ML technique in SRM modeling is the least square support vector machine (LSSVM) technique [92, 93]. Grid-diamond search (GDS) algorithm is applied to optimize the machine model developed using LSSVM technique [93].

As a summary, the polynomial functions, exponential functions and Fourier series technique can provide higher accuracy for the flux linkage/inductance profiles of the

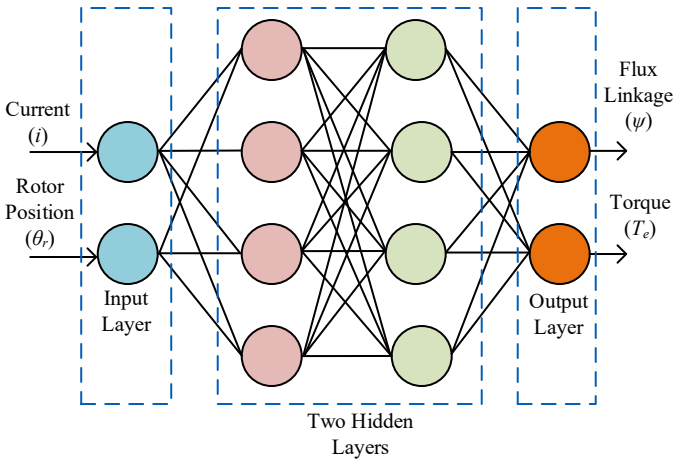

Figure 3.12: Four-layer Artificial Neural Network for modeling SRMs.

SRM compared to FEM. In addition to that, ANN and ML techniques can also provide high accuracy in comparison with FEM. However, those techniques consume large amount of time to develop the learning mechanism.

3.4 Numerical Modeling Techniques of SRMs

3.4.1 Finite Element Method

Among all numerical modeling techniques, FEM is considered as the most popular technique for modeling SRMs [44]. It is utilized in the design, analysis, and optimization of SRMs. The FEM is applied to design and analyze SRMs with various stator/rotor topologies [8, 94–97], stator/rotor segmented designs [95], double stator/rotor designs [97], and designs with multi-level airgaps [98]. It is also used in optimizing SRM designs to achieve different objectives such as to maximize the developed torque [30, 94, 95], minimize the torque ripple [8, 29, 30], minimize the Back EMF (BEMF) harmonics [96], minimize the machine weight and volume [96, 97, 99], and minimize the winding AC copper losses (DC copper loss and eddy current loss) [100, 101]. Despite the irregular flux pattern inside the machine slots, the FEM gives a relatively accurate calculation of the winding eddy-current density distribution [9].

The FE analysis procedure is shown in Fig. 3.13. The machine domain is discretized into a finite number of elements. A possible discretization of a quarter model of a 6/14 SRM is shown in Fig. 3.14 (a). The accuracy of the FE model depends on the number of mesh elements [38]. SRMs operate in saturation conditions, so it is necessary to increase the number of elements in the highly saturated regions to improve the model accuracy. Moreover, the machine airgap is changing with the rotation of

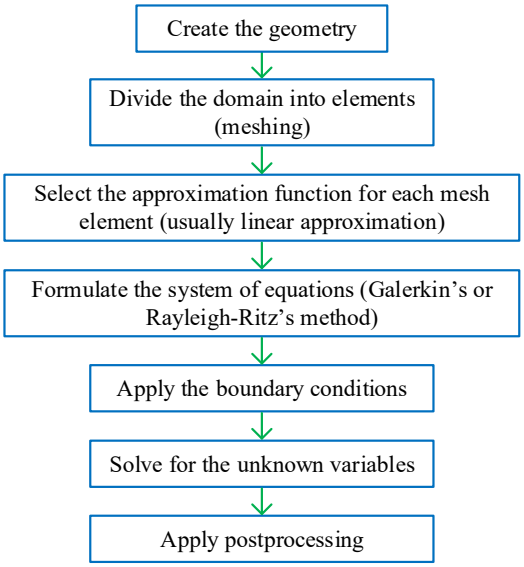

Figure 3.13: Procedure of the FE analysis.

the rotor, so it requires a large number of elements. This can be seen in Fig. 3.14 (b). Generally, magnetic vector potential or magnetic scalar potential are utilized to formulate the 2D FE system of equations [39]. The magnetic-vector-potential-based formulation is less suitable for 3D FE problems since it makes the system more complex and increases the computation burden significantly [9]. The 2D FE problem can be formulated using magnetic vector potential. A system of equations is developed for each element in terms of the magnetic vector potentials at the element nodes. These local systems are assembled together to formulate one global system of equations. Dirichlet, Neumann, and periodic boundary conditions are applied to the formulated system [38].

Due to the nonlinearity of the magnetic materials, the formulated system of equations is nonlinear. Numerical techniques, such as Newton-Raphson method, are used to solve for the magnetic vector potentials [102]. Post-processing is then applied to

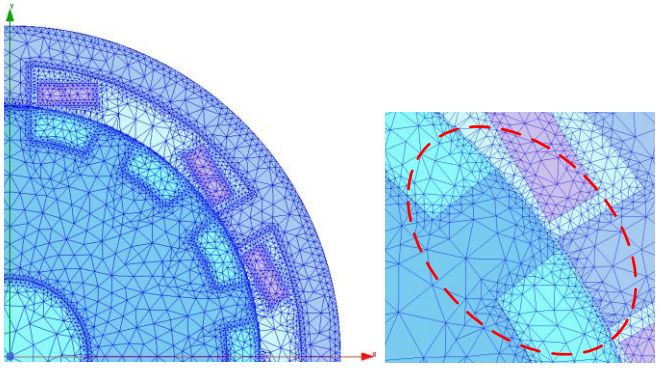

Figure 3.14: A mesh of a quarter model of a 6/14 SRM (a) whole mesh (b) mesh near the airgap.

the converged magnetic vector potentials to calculate various electromagnetic quantities such as flux linkage, flux density, and electromagnetic torque. The flux density distribution and flux lines in the stator and rotor of a FE model of a 6/14 SRM is shown in Fig. 3.15.

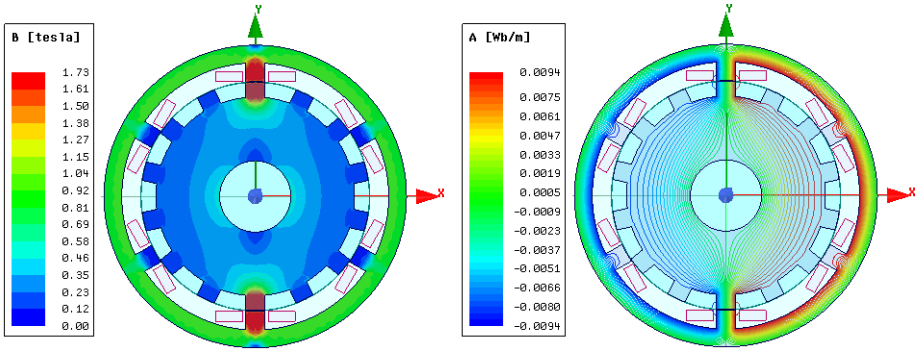

Figure 3.15: FE simulation model of a 6/14 SRM (a) Flux density distribution in the stator and rotor (b) Flux lines inside the machine at aligned position.

3.4.2 Boundary Element Method

BEM is another technique to model SRMs. Boundary integral equations are used in BEM to solve the electromagnetic fields on the problem domain boundary. BEM has been applied in the design and optimization of SRMs [103]. The accuracy of the BEM is as high as the FEM, and it requires lower computational burden [104]. However, its major drawback is the difficulty of considering the magnetic saturation [39] due to non-symmetric and fully populated coefficient matrices. Therefore, BEM and FEM [104, 105] or BEM and MEC [106] are commonly combined together to model SRMs. The FEM or MEC estimates the magnetic fields in the nonlinear regions whereas the BEM solves the magnetic field in the linear regions. Solving the electromagnetic field in the nonlinear region using MEC instead of using FEM reduces the computational burden and increases the simulation speed.

Meshing in BEM is performed at the machine boundary. The boundary mesh elements are one-dimensional for 2D domain and two-dimensional for 3D domain [9]. That is why it is less complex compared to FEM. A possible boundary mesh of a 2D half model of an 8/6 SRM is shown in Fig. 3.16. The mesh can be further refined to increase the accuracy. As in the FEM, a global coefficient matrix can be developed

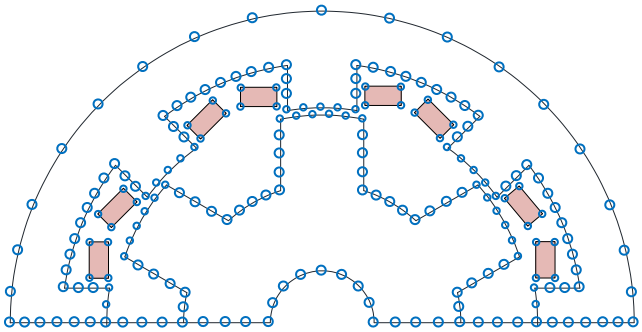

Figure 3.16: A boundary element mesh of a half model of an 8/6 SRM.

for BEM by assembling each local coefficient matrices. Hence the magnetic vector or scalar potential can be calculated inside the region of the boundary mesh region.

3.5 Magnetic Equivalent Circuit (MEC) Modeling Techniques of SRMs

The MEC method became popular in modeling SRMs in the past decade [9, 107]. In this method, the SRM geometry is represented as a magnetic circuit, that is analogues to an electric circuit. Then, the flux distribution inside the machine is calculated by solving the magnetic circuit. After that, the flux density, magnetic field intensity, phase flux linkage, and electromagnetic torque can be determined. The MEC technique is usually utilized to provide preliminary designs [11,12,108,109] and to analyze the electromagnetic characteristics [14,15,107] of SRMs. This technique is divided into two approaches: conventional MEC approach [110–112] and reluctance-mesh/finite-reluctance approach (FRA) [21, 25, 113, 114].

3.5.1 Conventional MEC Approach

This approach is simpler and faster compared to FEM. However, it is necessary to define the flux paths inside the machine before the modeling. The approach is based on Hopkinson's law [113] which can be stated as

$$F = \phi R_{mag}. \tag{3.5.1}$$

The magnetic scalar potential difference or MMF, F across a reluctance element

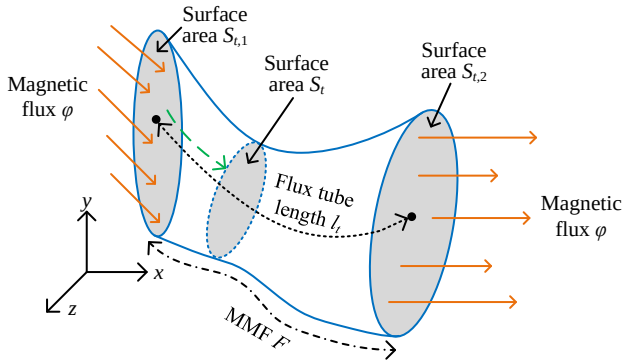

Figure 3.17: An arbitrary flux tube representation of flux path.

in Fig. 3.17 is obtained from [22]

$$F = \int_{l_t} \vec{H}.d\vec{l}. \tag{3.5.2}$$

The magnetic flux, ϕ can be defined as [113]

$$\phi = \iint_{S_t} \vec{B}.d\vec{S}. \tag{3.5.3}$$

The magnetic reluctance is a function of the magnetic circuit geometry and material permeability. The concept of flux tube can be applied to evaluate the reluctance of different geometries. A flux tube is an arbitrary 3D tube-shaped volume where flux enters from one side, and leaves from the other side as shown in Fig. 3.17 [22,115,116]. A general expression of the reluctance R_{mag} of this arbitrary geometry is [115]

$$R_{mag} = \int_0^{l_t} \frac{\nu}{S_t} dl. \tag{3.5.4}$$

Three common flux tube shapes could be utilized in an SRM as illustrated in Fig.

3.18 [13]. Applying (3.5.4), the corresponding reluctances in Fig. 3.18 (a), (b) and (c) can be evaluated as

$$R_a = \int_0^l \frac{\nu}{ah} dl = \frac{\nu l}{ah} \tag{3.5.5}$$

$$R_b = \frac{\nu \xi}{a \, log(r_2/r_1)} \tag{3.5.6}$$

$$R_c = \frac{\nu(l_2 - l_1)}{ah \, log(l_2/l_1)} \tag{3.5.7}$$

It is necessary to identify the flow paths of the flux inside the machine to develop the conventional MEC model. The identified flux paths can be divided into different flux tubes [12,14,15,19,20]. Each flux tube can be represented as a reluctance in the MEC model. A section of a developed conventional MEC model of the stator, rotor, and airgap of an SRM is shown in Fig. 3.19 [110]. The rotor is at the aligned position. The leakage fluxes between stator poles, and between stator poles and stator yoke

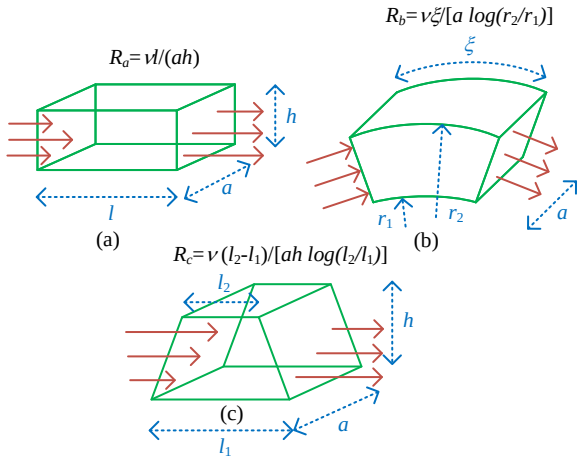

Figure 3.18: Common flux tube shapes for SRMs (a) rectangular shape, (b) curvilinear rectangular shape, and (c) trapezoidal shape elements.

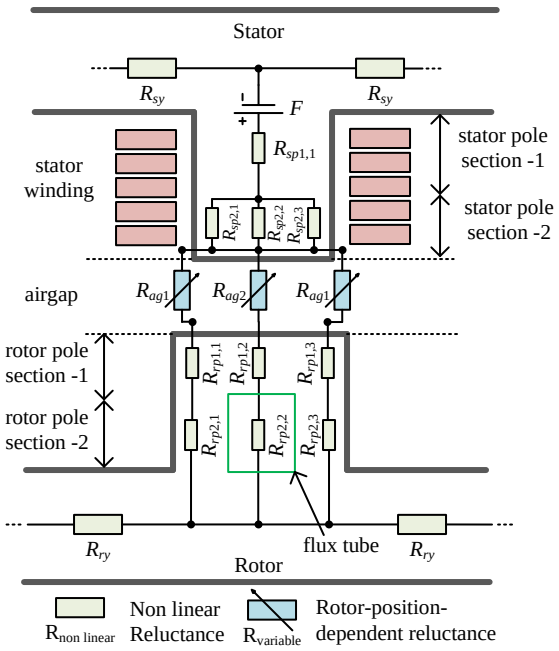

Figure 3.19: A conventional MEC of an SRM at the aligned position.

are neglected. Three main reluctance types are considered in an SRM [117]. Linear reluctance for materials with constant permeability, nonlinear reluctance for materials with nonlinear *B-H* characteristics, and position-dependent reluctance that depends on the rotor position. The third type is used in the airgap and has a constant relative permeability of 1. As shown in Fig. 3.19, both stator and rotor poles are divided into two sections, designated as section-1 and section-2 for each pole. This division helps estimating the local saturation accurately. The top section of the stator pole, section-1, has a single reluctance element $R_{sp1,1}$ whereas the bottom section, section-2, has three reluctance elements, $R_{sp2,1}$, $R_{sp2,2}$, and $R_{sp2,3}$. The flux flow inside the rotor pole becomes nonuniform if the rotor pole moves away from the excited stator pole. Thus, more discretization is necessary in the rotor pole region to improve the model accuracy. In Fig. 3.19, the rotor pole is divided into two sections, and each

section has three reluctance elements. Hence, the rotor pole has six reluctances which are $R_{rp1,1}$-$R_{rp1,3}$ and $R_{rp2,1}$-$R_{rp2,3}$. Both stator and rotor yokes are divided into two sections. Each stator and rotor yoke section has the same reluctances R_{sy} and R_{ry} since flux tubes in those sections have the same mean length and cross-section area. The airgap contains three reluctance elements. Two R_{ag1} reluctances corresponding to the fringing flux flowing through the non-overlap region between the stator and rotor poles. R_{ag2} corresponds to the flux passing through the overlap region. These airgap reluctances depend on the rotor position. The MMF source in the model represents the winding current times the number of turns.

The conventional MEC approach can be further extended to model the mutual coupling, multi-phase excitation [15, 111], and asymmetric airgap [19] in SRMs. The MEC models can be coupled with numerical or analytical models to develop hybrid models. In [16, 118], the airgap reluctances are obtained by FE simulations whereas the stator and rotor reluctances were modeled based on the conventional MEC approach. Instead of using FE simulations, analytical techniques may also be used to calculate the airgap reluctances, as in [17]. In [41, 42] and [119–121], analytical methods based on the MEC approach were proposed to estimate the phase flux linkage/phase inductance of an SRM. These methods are easy to implement and faster than solving the MEC numerically. However, leakage fluxes and local saturation in the stator and rotor poles were neglected in these analyses.

3.5.2 Reluctance Mesh/Finite Reluctance Approach

This approach can be derived as an extension of the finite fifference method (FDM). In FDM, the problem domain is divided into discrete grid points as shown in Fig. 3.20.

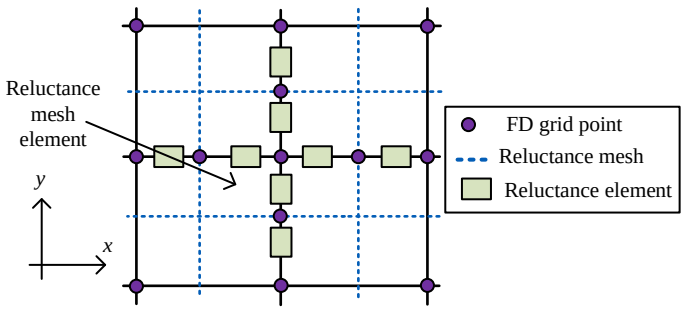

Figure 3.20: A general 2D section of a grid.

Then, the partial derivatives of magnetic scalar potential in (3.3.2) are approximated using finite difference (FD) and the potential values on the grid points [21,22,25,122]. In the reluctance mesh approach, the reluctances are defined between adjacent grid points as illustrated in Fig. 3.20 [9]. A reluctance mesh element, as depicted in Fig. 3.20, is defined around each grid point. The shape of the element is mainly rectangular, curvilinear rectangular, or trapezoidal as in Fig. 3.18. However, other shapes such as diamond [25] and hexagon [123] have also been utilized. Fig. 3.21 shows the 2D section of an open-profile SRM that is divided into a rectangular-shaped grid. Unlike the conventional MEC approach, the flux path inside the machine is not required to be known in advance to develop the reluctance mesh-based MEC model. The accuracy of the reluctance mesh-based model can be improved by refining the grid. However, this increases the number of elements and, hence, the computational burden and the simulation time.

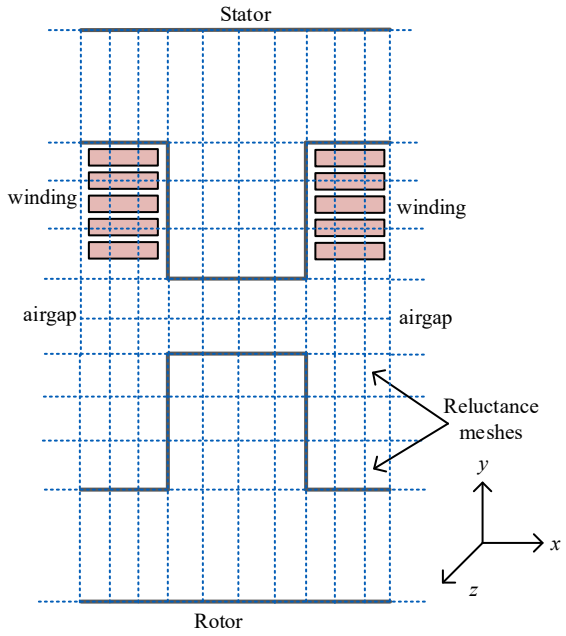

Figure 3.21: A reluctance mesh developed for an SRM.

3.5.3 Discussion

In this chapter, various modeling techniques have been investigated for SRMs. Table 3.3 summarizes the advantages, disadvantages, and applications of these techniques. These models are compared in terms of the accuracy, computational time, and the capability of modeling local saturation, electromagnetic losses, complex geometries, and 3D effects. It can be concluded that proper selection of the modeling technique depends on the application, required accuracy, suitable simulation speed, and available computational power.

Table 3.3: Comparison of electromagnetic modeling techniques for SRMs

	Model	Advantages	Disadvantages	Applications
Analytical	Maxwell's equations	Low computation time; easy to develop	Difficult to model local saturation, complex geometries, 3D effects and electromagnetic losses	Electromagnetic analysis & preliminary design
	Interpolation & curve fitting	Low computation time, easy to develop, can include local saturation	New data is required if the machine geometry changes	Motor drives
Numerical	FEM	High accuracy; can model complex geometries, 3D effects, electromagnetic losses, local saturation; the matrix assembly is simple	Requires large computation time and memory	Electromagnetic design & analysis, optimization
	BEM	High accuracy; can model complex geometries, 3D effects; requires moderate computational time and memory	Difficult to model local saturation, electromagnetic losses; matrix assembly is difficult	Electromagnetic design & analysis, optimization (Combined with FEM/MEC)
MEC	Conventional	Easy to develop; low computation time; can model local saturation electromagnetic losses; matrix assembly is simple	Difficult to model complex geometries, 3D effects; has moderate accuracy; requires defining flux paths in advance	Electromagnetic design & analysis
	Reluctance Mesh	Good accuracy; can model complex geometries, 3D effects, local saturation, electromagnetic losses; does not require defining flux path in advance; matrix assembly is easy	Requires moderate computational time and memory	Electromagnetic design & analysis, optimization

3.5.4 Summary

Various modeling techniques for SRMs were presented in this chapter. Both analytical, numerical, and MEC modeling techniques were discussed. Maxwell's equation-based methods and interpolation, and curve fitting methods were discussed under the analytical methods. Modeling of SRMs using the FEM and BEM methods were discussed as the numerical methods. The conventional and reluctance mesh-based MEC methods were analyzed under the MEC modeling techniques. Finally, the advantages, disadvantages, and applications of each modeling technique were summarized.

Chapter 4

Modeling SRMs Using Reluctance Mesh-Based MEC Method

4.1 Introduction

This chapter proposes a 2D reluctance mesh-based MEC model for SRMs. The developed model accounts for local saturation, leakage and fringing fluxes, and multiphase excitation. The models of 3-phase 6/4, 6/10, 12/8 SRMs, and 4-phase 8/6, 8/10, and 16/12 SRMs are implemented using the reluctance mesh-based MEC technique. The static and dynamic characteristics of those SRMs are computed. Corresponding 2D FEM models have been utilized to validate the results from the MEC models. The simulated static and dynamic performances are further validated using experimental results on a 4-phase 8/6 SRM.

4.2 Proposed Reluctance Mesh-Based MEC

4.2.1 Derivation of the Proposed MEC Method

The magnetic scalar potential-based approach can be applied to solve the magnetic field inside a magnetic circuit. The magnetic scalar potential distribution U inside the magnetic device is expressed using [25, 39]

$$\nabla \cdot (\frac{1}{\nu} \nabla U) = \nabla \cdot (\frac{1}{\nu} \vec{T}). \tag{4.2.1}$$

The magnetic domain can be discretized as shown in Fig. 4.1 (a). The partial derivatives in (4.2.1) are approximated using Finite Difference (FD) by

$$\frac{1}{\nu}\left(\frac{U_1 - U_0}{h^2} + \frac{U_3 - U_0}{h^2}\right) + \frac{1}{\nu}\left(\frac{U_2 - U_0}{l^2} + \frac{U_4 - U_0}{l^2}\right) = \frac{1}{\nu}\left(\frac{T_1 - T_2}{2h}\right). \tag{4.2.2}$$

Electric vector potential, $\vec{T}$ in (4.2.1) is not a physical vector field. It is defined to follow the Ampere's law around any arbitrary closed loop inside the magnetic domain [45]. In 2D analysis, the direction of $\vec{T}$ can be assumed either along the x- or y-axis. That assumption satisfies the Ampere's law and simplifies the analysis. In Fig. 4.1 (a), the direction of $\vec{T}$ is chosen along the y-axis. Additionally, $\vec{T}$ is distributed uniformly in the magnetic domain since uniform current density distribution is assumed in the stator slots.

The reluctivity of each mesh element is considered constant. The length and height of a mesh element in Fig. 4.1 (a) are $2l$ and $2h$, respectively. Multiplying both sides of (4.2.2) by the product of the length l, height h, and axial length a of a mesh

element (lha) and rearranging the expression, we get

$$\frac{1}{\nu}\left(\frac{U_1-U_0}{R_1}+\frac{U_3-U_0}{R_1}\right)+\frac{1}{\nu}\left(\frac{U_2-U_0}{R_2}+\frac{U_4-U_0}{R_2}\right)= \frac{1}{\nu}\left(\frac{(T_1+T_0)h}{2}-\frac{(T_2+T_0)h}{2}\right)\frac{1}{R_2}. \quad (4.2.3)$$

R_1 and R_2 are the reluctance elements along x- and y-axis directions and they are expressed as $(\nu h/la)$ and $(\nu l/ha)$, respectively. The relationship between the MMF and $\vec{T}$ is given by

$$F=\oint_{l_c}\vec{T}\cdot d\vec{l} \quad (4.2.4)$$

where l_c is any closed line in the magnetic domain. The electric vector potentials in

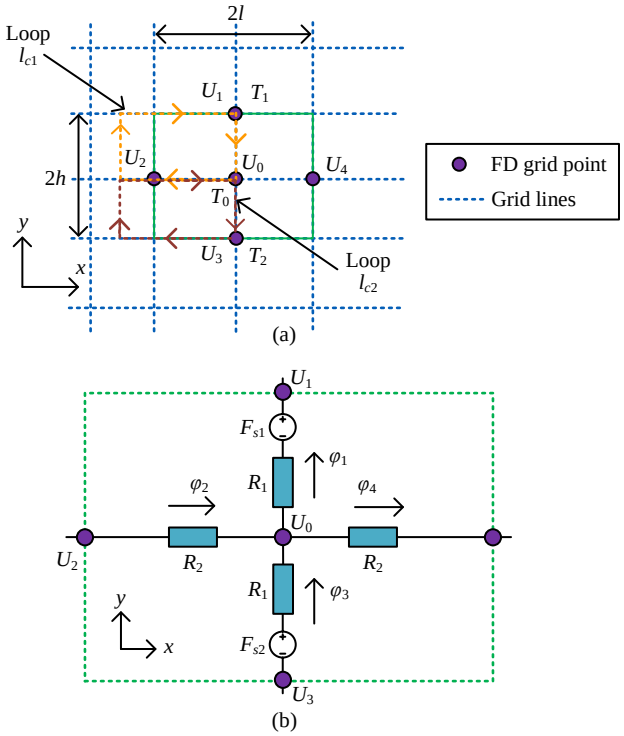

Figure 4.1: (a) Discretization of the magnetic domain and (b) the general representation of a mesh element [2].

(4.2.3) is replaced using MMFs F_{s1} and F_{s2} by evaluating (4.2.4) along closed lines l_{c1} and l_{c2} shown in Fig. 4.1 (a). Hence, (4.2.3) is further simplified as

$$\left(\frac{U_1 - U_0 - F_{s1}}{R_1} + \frac{U_3 - U_0 + F_{s2}}{R_1}\right) + \left(\frac{U_2 - U_0}{R_2} + \frac{U_4 - U_0}{R_2}\right) = 0. \tag{4.2.5}$$

Fig. 4.1 (b) shows the arrangement of reluctance elements in a mesh element according to (4.2.5) [23]. ϕ_1, ϕ_2, ϕ_3 and ϕ_4 in Fig. 4.1 (b) are branch fluxes across the reluctances in the mesh element.

4.2.2 Proposed Method for Meshing the Geometry

It is necessary to mesh the SRM geometry before obtaining field solutions. In the proposed model, the SRM geometry is divided into five regions: stator pole region, stator back-iron region, rotor pole region, rotor back-iron region, and airgap region. Each region is independently meshed along the radial and circumferential directions, as shown in Fig. 4.2.

The size of the airgap mesh elements needs to be chosen at the beginning of meshing. For a higher number of rotor poles, a smaller circumferential width should be selected for airgap mesh elements to increase the accuracy of the field solution. The circumferential width of the mesh elements in the airgap region is the same as the rotation step angle. The widths of the mesh elements in other regions are integer multiples of the step angle. The accuracy of the model increases with a lower rotation step angle. That also increases the computation time. In Fig. 4.2, the airgap region elements have circumferential arc length of 1.5°. For simplicity, the circumferential width of the rotor pole region elements are chosen the same as the airgap region. The elements in the stator pole region have a circumferential arc length of 3°. The

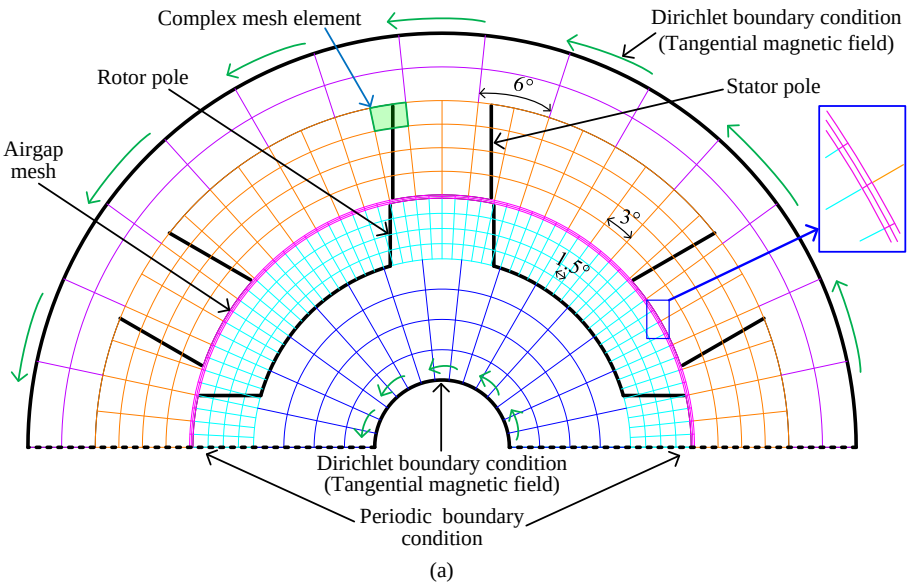

Figure 4.2: An example reluctance mesh for half model of 6/4 SRM [2].

stator back-iron and rotor back-iron region elements have a circumferential length of 6° since these regions do not experience high local saturation.

The number of radial divisions in each region can also be chosen based on the required level of accuracy and computation time. The stator and rotor pole regions have four radial layers as depicted in Fig. 4.2. There are only two radial layers in the stator back-iron region due to lower saturation. There are four radial layers in the rotor back-iron region even though this region has lower saturation because it is thicker than the stator back-iron. The airgap consists of two layers along the radial direction. The first layer is stationary and near the stator. The second layer is closer to the rotor, and the elements in that layer rotate with the rotor. The mesh elements in the stator slots, the gaps between the rotor poles and airgap contain only air. These elements are called linear elements and they have unity relative reluctivity. The mesh elements that belong to the stator and rotor poles and back-iron contain

reluctivity characteristics of the magnetic steel. Thus, these elements are nonlinear elements. The relative reluctivity of the utilized magnetic steel material is calculated using the B-H characteristics of the material.

The mesh elements near the stator and rotor pole teeth edges include both magnetic steel and air. Thus, these elements are called complex elements. The relative reluctivities of the complex elements are computed by averaging the reluctivity of steel portion and the reluctivity of the air portion [113]

$$\nu_{r,comp} = \frac{\nu_{r,st}\nu_{r,g}A_{c,tot}}{\nu_{r,st}A_{c,g} + \nu_{r,g}A_{c,st}}. \tag{4.2.6}$$

The length and height of these complex elements are needed to be sufficiently small to minimize the geometry approximation errors even though this raises the computation time.

4.2.3 Proposed Method for Calculating MMF

The flux is produced in an SRM only by the excitation currents in the windings. Hence, the value of $\vec{T}$ is not zero in the mesh elements that belong to the stator slots. A non-zero value is defined in the stator poles for $\vec{T}$ to follow the Ampere's law. Thus, MMF sources are applied to the mesh elements that belong to the slots and stator poles, as shown in Fig. 4.3 (a). However, stator back-iron, the entire rotor, and airgap have no MMF sources due to zero $\vec{T}$ distribution.

The winding function theory is applied to calculate the values of the MMF sources of the mesh elements in the slots and stator poles [124]. As shown in Fig. 4.3 (a),

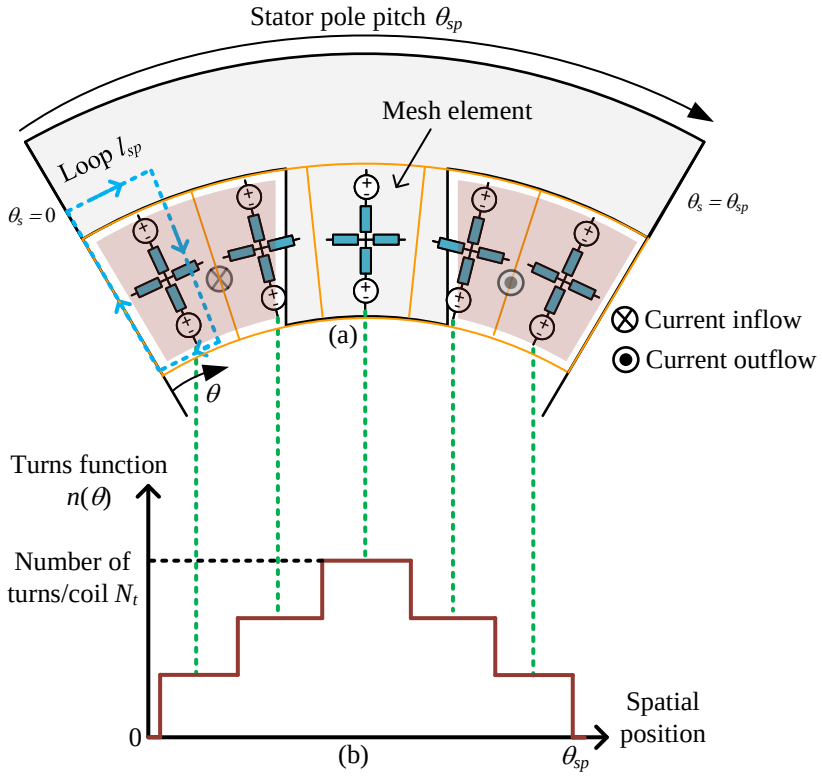

Figure 4.3: Magnetomotive force (MMF) calculation (a) The locations of MMF sources and (b) a half period of the $n(\theta_s)$ for one stator pole pitch of an SRM [2].

Ampere's law is applied along the closed-loop, l_{sp}

$$\oint_{l_{sp}} \vec{H} \cdot d\vec{l} = n(\theta_s) I_s \tag{4.2.7}$$

where I_s is the excitation current. The turns function, $n(\theta_s)$ indicates the total number of turns enclosed in the loop l_{sp} at the spatial position θ_s. $n(\theta_s)$ has a magnitude and sign. The magnitude depends on the number of turns, and the sign is positive or negative according to the direction of the current flow in the stator slots. A half period of $n(\theta_s)$ is shown in Fig. 4.3 (b) and the remaining half period has similar and opposite magnitude. The winding turns are assumed to be uniformly

distributed in the stator slots. Then, the winding function $N(\theta_s)$ can be defined by

$$N(\theta_s) = n(\theta_s) - n_{avg}(\theta_s) \tag{4.2.8}$$

where $n_{avg}(\theta_s)$ is the average of the $n(\theta_s)$ over 360° mechanical period. $n_{avg}(\theta_s)$ for an SRM with a double layer concentrated winding is zero based on the distribution of $n(\theta_s)$ around the stator. Thus, $N(\theta_s)$ is the same as $n(\theta_s)$ shown in Fig. 4.3 (b). Hence, the MMF distribution, F_s in the airgap can be determined as a function of θ_s

$$F_s = N(\theta_s)I_s. \tag{4.2.9}$$

4.2.4 Assembling the Mesh Elements in the MEC

After meshing the SRM geometry and calculating the MMF, neighboring reluctance elements can be connected to build the MEC model. Fig. 4.4 shows an example for assembling the reluctance elements and imposing the boundary conditions. As shown in Fig. 4.4, the 1st and 2nd rows of the reluctance mesh belong to the stator back-iron region and stator pole region, respectively. The mesh elements in the 3rd row are for the airgap. The 4th row and 5th row mesh elements are for the rotor pole region and rotor back-iron region, respectively. As shown in Fig. 4.4, any particular mesh element has four branches. A branch is the part between two nodes in the MEC. Each single mesh element contains maximum of four branches. The top and bottom branches in the 2nd row mesh elements (i.e. stator pole region) can have MMF sources depending on $n(\theta_s)$. The MMF sources are connected in series with the reluctance elements. Branches can be connected with other neighboring branches, and these connections create flux loops in the MEC, as shown in Fig. 4.4. In this example, 1st

row mesh elements and 5^{th} row mesh elements have only three branches in each mesh element that impose the Dirichlet boundary condition. Thus, the magnetic field is tangential at the top and bottom boundaries. Also, periodic boundary condition is applied according to the symmetry of the MEC. The rotating elements are shown in the middle in Fig. 4.4. The rotation is achieved by interchanging the nodes n_{r1}, n_{r2} and n_{r3}. Counter-clockwise rotation is considered here and one step angle rotation is achieved by moving n_{r1} to n_{r2}, n_{r2} to n_{r3}, and n_{r3} to n_{r1}.

4.2.5 Field Solution Technique

After assembling the MEC, the loop analysis method is applied to solve the loop fluxes in the MEC model. The following equation system is solved iteratively [24]

$$\boldsymbol{r} = \boldsymbol{R}\boldsymbol{\phi}_l - \boldsymbol{F}_l. \tag{4.2.10}$$

The reluctance network matrix $\boldsymbol{R}$ is derived by

$$\boldsymbol{R} = \boldsymbol{L}^T diag(\boldsymbol{R}_b)\boldsymbol{L}. \tag{4.2.11}$$

The reluctance elements in every branch of the MEC model is included as a column vector in $\boldsymbol{R}_b$. The element l_{ij} in the i^{th} row and the j^{th} column of $\boldsymbol{L}$ is defined as follows [24]

$$l_{ij} = \begin{cases} 1, & \text{loop } j \text{ \& branch } i \text{ are in same direction} \\ -1, & \text{loop } j \text{ \& branch } i \text{ are in opposite direction} \\ 0, & \text{otherwise.} \end{cases} \tag{4.2.12}$$

The elements in $\boldsymbol{F}_l$ in (4.2.10) contain total MMF enclosed in each loop flux. $\boldsymbol{F}_l$ is defined as

$$\boldsymbol{F}_l = \boldsymbol{N}\boldsymbol{I}_s. \tag{4.2.13}$$

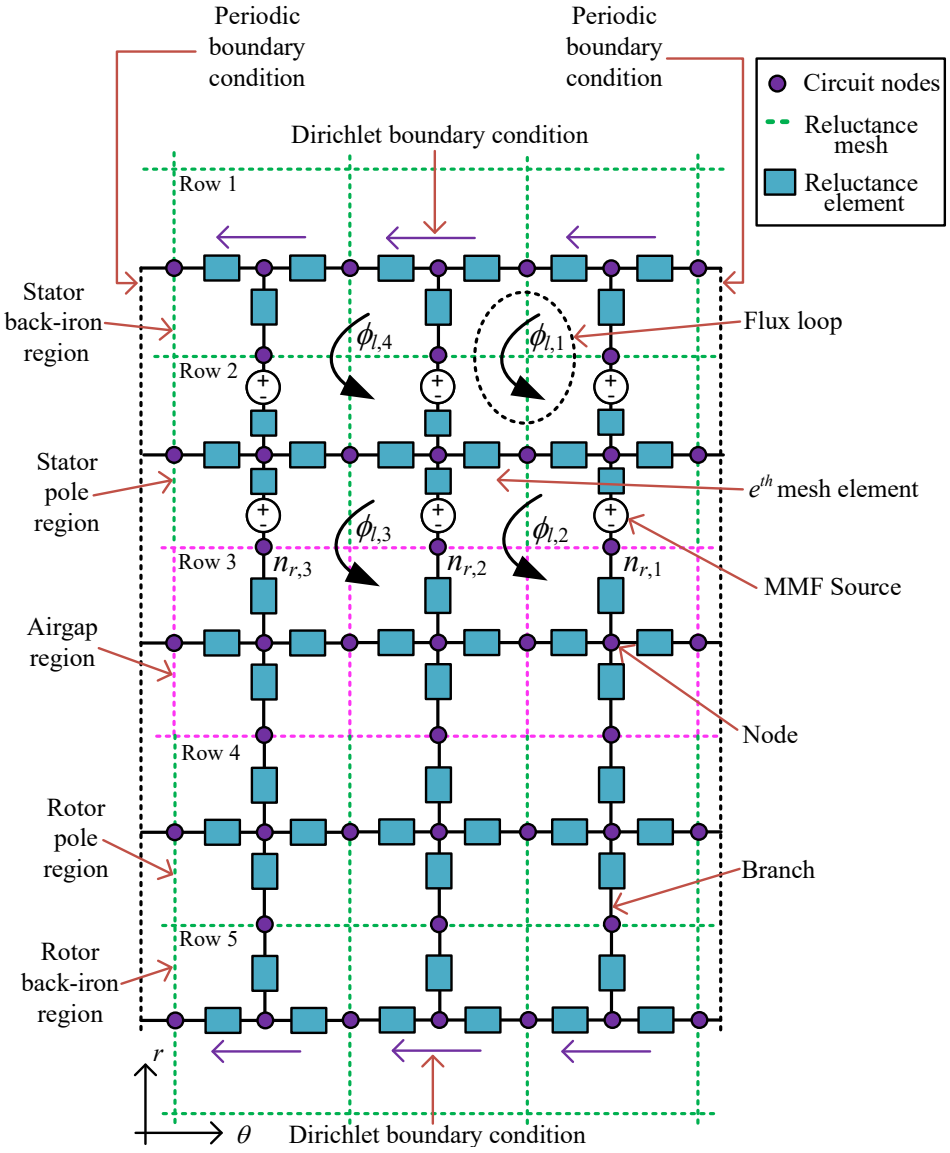

Figure 4.4: An example of assembling the mesh elements and imposing the boundary conditions [2].

$\boldsymbol{N}$ is the winding function matrix which contains sum of $N(\theta_s)$ values of each loop corresponding to each phase in the MEC model. $\boldsymbol{N}$ is deduced by

$$\boldsymbol{N} = \boldsymbol{L}^T diag(\boldsymbol{N}_b)\boldsymbol{M} \tag{4.2.14}$$

where $\boldsymbol{N}_b$ contains the $N(\theta_s)$ value corresponding to each branch in mesh elements. The phase split matrix $\boldsymbol{M}$ that splits the $N(\theta_s)$ values in $\boldsymbol{N}_b$ into corresponding phases of the SRM. The matrix $\boldsymbol{M}$ is defined as

$$\boldsymbol{M} = \begin{pmatrix} \mathbf{1}_{(n_{rs}\times 1)} & \mathbf{0}_{(n_{rs}\times 1)} & \cdots & \mathbf{0}_{(n_{rs}\times 1)} \\ \mathbf{0}_{(n_{rs}\times 1)} & \mathbf{1}_{(n_{rs}\times 1)} & \cdots & \mathbf{0}_{(n_{rs}\times 1)} \\ \vdots & \vdots & \ddots & \vdots \\ \mathbf{0}_{(n_{rs}\times 1)} & \mathbf{0}_{(n_{rs}\times 1)} & \cdots & \mathbf{1}_{(n_{rs}\times 1)} \end{pmatrix} \tag{4.2.15}$$

where n_{rs} represents the ratio of the total number of reluctance elements in the MEC and the total number of stator poles of the SRM. Here, n_{rs} determines the size of ones and zero vectors in $\boldsymbol{M}$.

The equation system in (4.2.10) is formulated as an unconstrained nonlinear least-square optimization problem. Then Gauss-Newton method is applied to minimize the Objective Function (OF)

$$OF = \frac{1}{2}\boldsymbol{r}^T\boldsymbol{r}. \tag{4.2.16}$$

The iterative algorithm to solve (4.2.16) is shown in Fig. 4.5. At the beginning, the rotor position θ_r is set to zero. Also, $\boldsymbol{\phi_l}$ and $\boldsymbol{B}$ are defined as zero vectors. Additionally, the $\boldsymbol{\nu}_r$ is defined as a unit vector and its derivative $\boldsymbol{\nu}_r'$ is defined as a

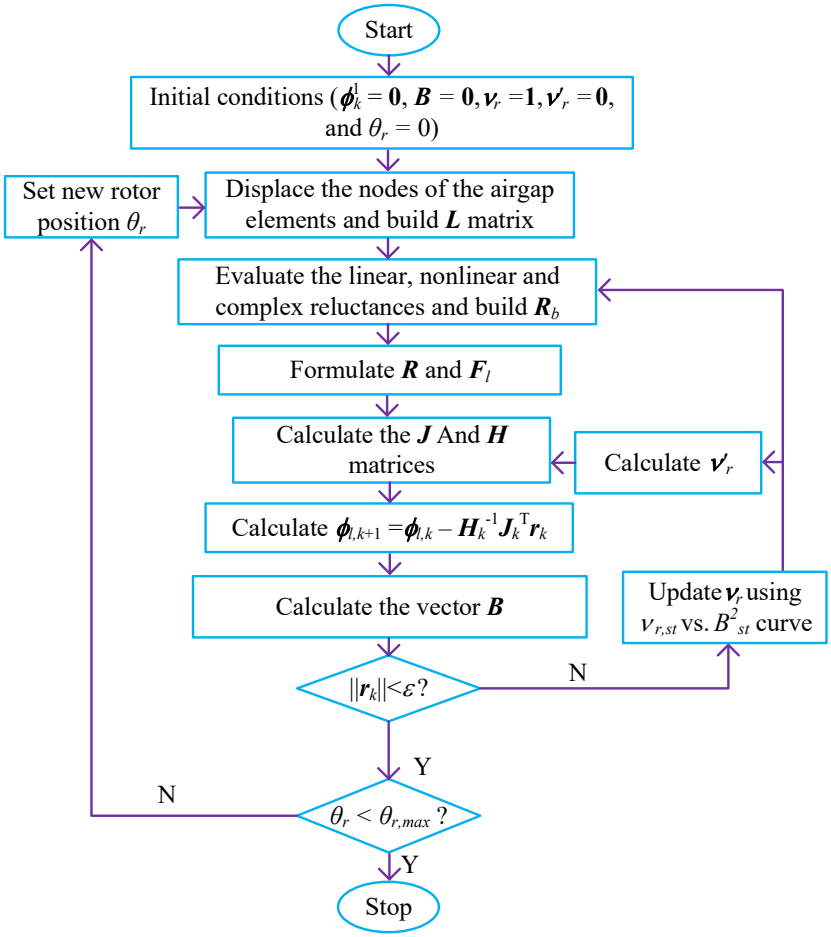

Figure 4.5: The procedure for solving the reluctance mesh-based MEC [2].

zero vector. Then $\boldsymbol{L}$ is assembled according to θ_r. After that $\boldsymbol{R}_b$ is built by calculating the reluctances of all the branches in the MEC model. Hence, vector $\boldsymbol{R}$ and vector $\boldsymbol{F}_l$ are determined from (4.2.11) and (4.2.13). Then the Jacobian matrix $\boldsymbol{J}$ is computed from

$$\boldsymbol{J} = \boldsymbol{R} + \boldsymbol{L}^T \cdot diag\Big(\boldsymbol{R}_b \circ (\boldsymbol{\nu}_r \circ \boldsymbol{A}_b^{\circ 2})^{\circ -1} \circ \boldsymbol{\nu}'_r \circ \boldsymbol{\phi}_b\Big)\Big((\boldsymbol{L} \cdot diag(\boldsymbol{\phi}_l)\boldsymbol{C}) \circ \boldsymbol{L}\Big). \quad (4.2.17)$$

The symbols $\cdot$ and $\circ$ denote matrix multiplication and element-wise multiplication,

respectively. The *diag* operator creates a diagonal matrix from a given vector. $\boldsymbol{\phi}_b$ can be determined by

$$\boldsymbol{\phi_b} = \boldsymbol{L}\boldsymbol{\phi}_l. \tag{4.2.18}$$

$\boldsymbol{C}$ in (4.2.17) describes the connection between branch and loop fluxes. The element c_{ij} in the i^{th} row and the j^{th} column of $\boldsymbol{C}$ is defined as [24]

$$c_{ij} = \begin{cases} 1, & \text{if } i = j \\ 1, & \text{if } \phi_{l,i} - \phi_{l,j} = \phi_{b,k} \\ 0, & \text{otherwise} \end{cases} \tag{4.2.19}$$

where $\phi_{l,i}$ and $\phi_{l,j}$ are i^{th} and j^{th} loop fluxes, respectively. $\phi_{b,k}$ is the k^{th} branch flux that can be calculated by $\phi_{l,i} - \phi_{l,j}$.

The vector $\boldsymbol{\nu}_r$ in (4.2.17) consists of the relative reluctivities of linear, nonlinear and complex mesh elements. The relative reluctivities of linear elements are one. The relative reluctivity of nonlinear elements is calculated by

$$\nu_{r,st} = \nu_{r,st}(B_{st}^2) \tag{4.2.20}$$

where $\nu_{r,st}(B_{st}^2)$ is the relative reluctivity as a function of B_{st}^2. The function, $\nu_{r,st}$ is obtained using the B-H characteristics of the steel material. $\nu_{r,st}$ corresponding to each pair of flux density, B_{st} and magnetic field intensity, H_{st} values in the B-H characteristics is calculated by

$$\nu_{r,st} = \frac{H_{st}}{\nu_0 B_{st}}. \tag{4.2.21}$$

Using (4.2.21), $\nu_{r,st}$ corresponding to each B_{st} value in B-H characteristics is determined. B_{st}^2 is then obtained by squaring each B_{st} value in the B-H characteristics. Hence, function $\nu_{r,st}(B_{st}^2)$ is developed with the calculated values of $\nu_{r,st}$ and corresponding B_{st}^2 values using linear piece-wise interpolation. Developing $\nu_{r,st}$ as a function of B_{st}^2 enables using only the first quadrant of the B-H curve. After calculating the flux densities of the nonlinear mesh elements, (4.2.20) is applied to calculate $\nu_{r,st}$ of the nonlinear elements. The relative reluctivities of the complex elements are then calculated using (4.2.6).

$\boldsymbol{\nu}_r'$ in (4.2.17) contains the derivatives of the elements in $\boldsymbol{\nu}_r$ with respect to the corresponding B_{st}^2 of mesh elements. The derivatives of the linear elements are zero. The FD approximation is applied to determine the derivatives of the nonlinear elements

$$\nu_{r,st}'(B_{st}^2) = \frac{\nu_{r,st}(B_{st}^2 + \Delta B_{st}^2) - \nu_{r,st}(B_{st}^2 - \Delta B_{st}^2)}{2(\Delta B_{st}^2)}. \tag{4.2.22}$$

Equation (4.2.6) is differentiated with respect to B_{st}^2 to calculate the derivatives of the complex elements. Once $\boldsymbol{J}$ is obtained by (4.2.17), the Hessian matrix $\boldsymbol{H}$ is calculated by

$$\boldsymbol{H} = \boldsymbol{J}^T \boldsymbol{J}. \tag{4.2.23}$$

Then, the solution of $\boldsymbol{\phi}_l$ at $(k+1)^{th}$ iteration is obtained by

$$\boldsymbol{\phi}_{l,k+1} = \boldsymbol{\phi}_{l,k} - \boldsymbol{H}_k^{-1} \boldsymbol{J}_k^T \boldsymbol{r}_k. \tag{4.2.24}$$

After that, a new $\boldsymbol{B}$ is determined and the convergence criteria are checked. If the field solution is converged, the same procedure is repeated for the next θ_r. Else, $\boldsymbol{\nu}_r$ is updated from $\nu_{r,st}$ vs. B_{st}^2 relationship based on the new $\boldsymbol{B}$ and $\boldsymbol{\nu}_r'$ is re-calculated.

Hence, new $\boldsymbol{R}_b$ is obtained, and the iterative process repeats until the convergence is achieved.

4.3 Calculating the Electromagnetic Quantities

After obtaining $\boldsymbol{\phi_l}$, different results can be post-processed. This section explains the calculation of magnetic energy, magnetic flux density, magnetic field intensity, phase flux linkage, and electromagnetic torque.

4.3.1 Magnetic Energy

The magnetic energy of the e^{th} mesh element shown in Fig. 4.1 (b) is obtained by [13]

$$W_{m,e} = \frac{1}{2} V_e (\nu_{r,e}\, \nu_0) B_e^2 \tag{4.3.1}$$

where B_e and $\nu_{r,e}$ are the magnetic flux density and relative reluctivity of the e^{th} element, respectively. The volume V_e of the e^{th} element is equal to $4alh$, as the length of an element is $2l$ and the height of an element is $2h$. The magnetic energy of the same mesh element in Fig. 4.1 (b) can also be expressed as [23]

$$W_{m,e} = \frac{1}{2} R_1 (\phi_1^2 + \phi_3^2) + \frac{1}{2} R_2 (\phi_2^2 + \phi_4^2). \tag{4.3.2}$$

4.3.2 Magnetic Flux Density and Magnetic Field Intensity

The volume $V_e = 4alh$ is substituted in (4.3.1) and, $R_1 = (\nu h/la)$ and $R_2 = (\nu l/ha)$ are substituted in (4.3.2). As shown in Fig. 4.1 (b), ϕ_1 and ϕ_3 are the branch fluxes along the radial direction and, ϕ_2 and ϕ_4 are the branch fluxes along the tangential

direction. Then, equations (4.3.1) and (4.3.2) are equated, and the radial flux density $B_{rad,e}$ and the tangential flux density $B_{tan,e}$ of the e^{th} mesh element [23] are obtained as

$$B_{rad,e} = \sqrt{\frac{\phi_1^2 + \phi_3^2}{2A_{rad,e}^2}},\ B_{tan,e} = \sqrt{\frac{\phi_2^2 + \phi_4^2}{2A_{tan,e}^2}}. \tag{4.3.3}$$

Hence, the magnitude of the flux density and magnetic field intensity of the e^{th} mesh element are obtained as

$$B_e = \sqrt{B_{rad,e}^2 + B_{tan,e}^2},\ H_e = (\nu_0\, \nu_{r,e}) B_e. \tag{4.3.4}$$

4.3.3 Phase Flux Linkage

The phase flux linkage of an SRM can be determined by

$$\boldsymbol{\psi} = p\boldsymbol{N}^T \boldsymbol{\phi}_l \tag{4.3.5}$$

where p represents the number of magnetic poles of the considered SRM. $\boldsymbol{N}$ and $\boldsymbol{\phi}_l$ are the winding function matrix and the loop flux vector, respectively.

4.3.4 Electromagnetic Torque

Maxwell Stress Tensor (MST) method is applied to calculate the electromagnetic torque. The radial and tangential force densities in the airgap can be expressed by [6]

$$\sigma_{rad} = \frac{\nu_0}{2}(B_{rad}^2 - B_{tan}^2), \sigma_{tan} = \nu_0(B_{rad}\, B_{tan}). \tag{4.3.6}$$

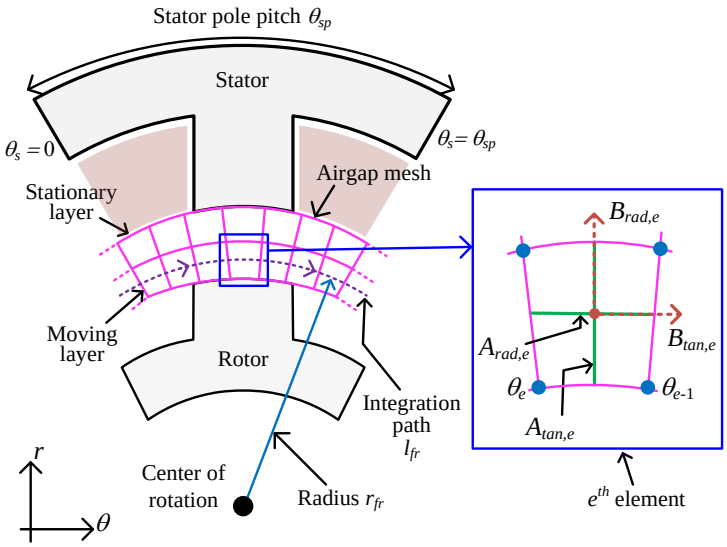

Figure 4.6: Choosing the integration path for computing the electromagnetic torque [2].

B_{rad} and B_{tan} are the flux densities at an arbitarary location in the airgap where, σ_{rad} and σ_{tan} are evaluated. In 2D analysis, the electromagnetic torque generated on the rotor can be calculated by integrating the tangential force density in the airgap,

$$T = p\nu_0 a \int_{l_{fr}} r_{fr}(B_{rad}\, B_{tan}) dl \tag{4.3.7}$$

where l_{fr} is the integration path in the airgap, r_{fr} is the distance to the center of the rotation axis. As shown in Fig. 4.6, the arc l_{fr} is selected along the centers of the rotating airgap mesh elements [22]. l_{fr} is divided into n_s number of sections, which is similar to the number of mesh elements in the rotating airgap layer. Then, (4.3.7) is written as a summation for all elements along the integration path

$$T = p\nu_0 a\, r_{fr}^2 \sum_{e=1}^{n_s} (B_{rad,e}\, B_{tan,e})(\theta_e - \theta_{e-1}). \tag{4.3.8}$$

4.4 Static Characteristics of SRMs

Using the proposed MEC model, the static characteristics of SRMs with different pole configurations are simulated with constant current excitation applied to one phase. The field solution is obtained by solving (4.2.10). The airgap flux densities and static flux linkage are computed from (4.3.3) and (4.3.5), respectively. Then, static electromagnetic torque is obtained using (4.3.8). The airgap flux density and static characteristics of the 3-phase and 4-phase SRMs from the MEC model are presented in this section and verified with the corresponding FEM results.

4.4.1 Airgap Flux Density

The airgap radial and tangential flux densities of 3-phase 6/4, 6/16, and 12/8, and 4-phase 8/6, 8/10, and 16/12 SRMs over one stator pole pitch are presented in Figs. 4.7, 4.8, 4.9, 4.10, 4.11, and 4.12, respectively. The exciation currents in the flux density calculation are chosen to operate the magnetic core in the nonlinear region of the B-H curve.

Overall, the radial and tangential flux density components at the unaligned and aligned positions show good agreement with corresponding flux densities obtained from FEM. The tangential component of the flux density at the aligned position shows small errors closer to the spatial positions corresponding to stator and rotor teeth edges. This is due to the geometry approximations with the complex elements. A smaller error can be achieved by decreasing the size of the complex elements. This would also increase the computation time. The accuracy of the airgap flux densities can be further enhanced by adding more mesh elements to the airgap. Moreover, increasing the number of elements in the stator and rotor poles also improves the

accuracy as these regions experience higher local saturation.

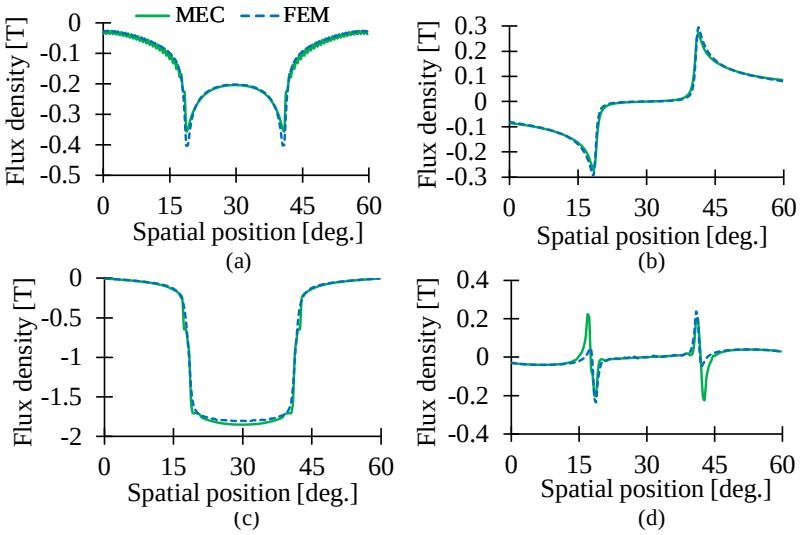

Figure 4.7: The flux density components in the airgap for 20 A excitation current of the 6/4 SRM (a) radial and (b) tangential components at the unaligned position, and (c) radial and (d) tangential components at the aligned position [2].

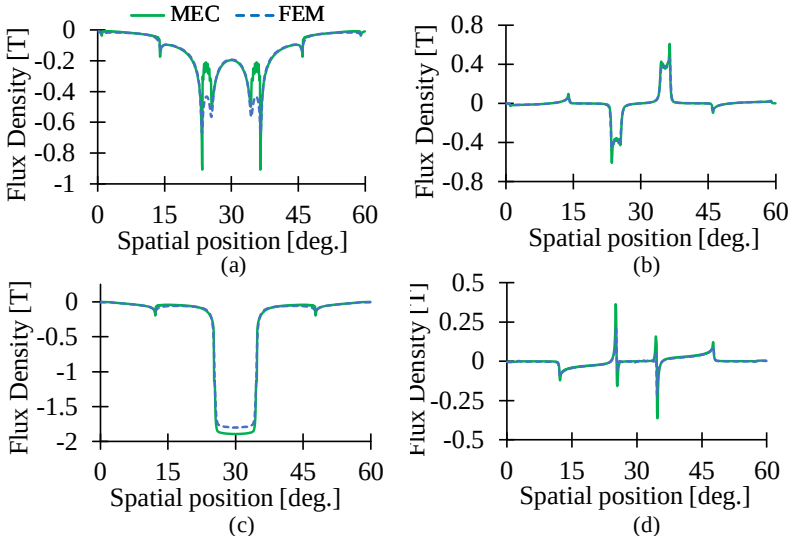

Figure 4.8: The flux density components in the airgap for 20 A excitation current of the 6/16 SRM (a) radial and (b) tangential components at the unaligned position, and (c) radial and (d) tangential components at the aligned position.

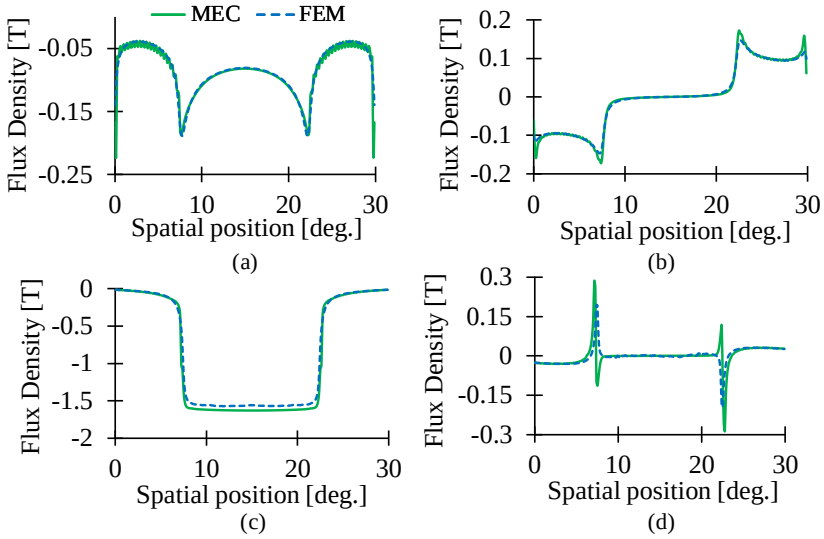

Figure 4.9: The flux density components in the airgap for 20 A excitation current of the 12/8 SRM (a) radial and (b) tangential components at the unaligned position, and (c) radial and (d) tangential components at the aligned position.

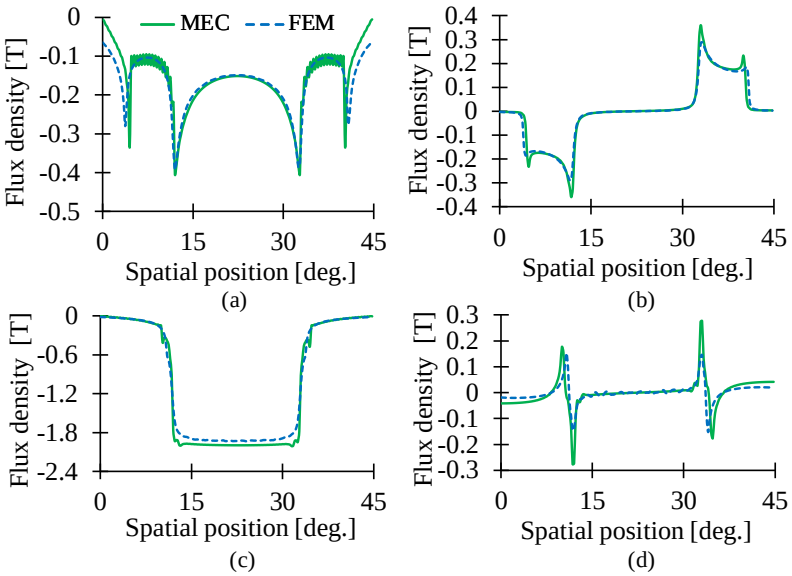

Figure 4.10: The flux density components in the airgap for 35 A excitation current of the 8/6 SRM (a) radial and (b) tangential components at the unaligned position, and (c) radial and (d) tangential components at the aligned position [2].

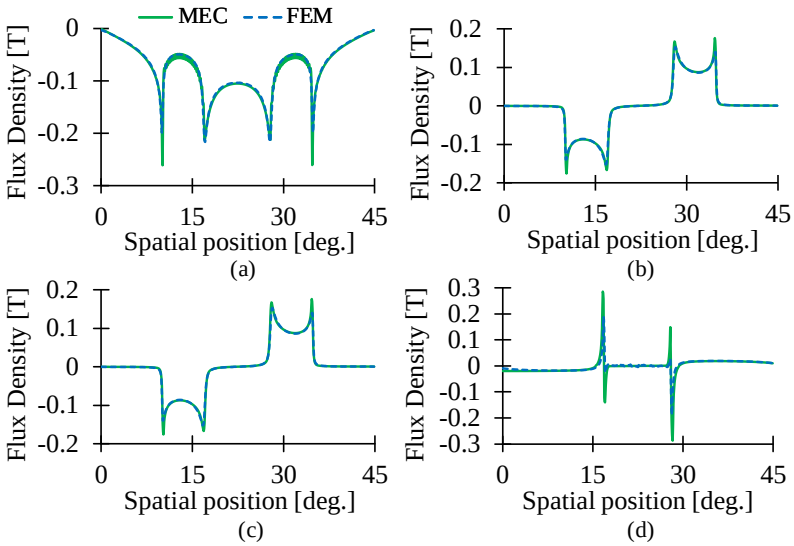

Figure 4.11: The flux density components in the airgap for 20 A excitation current of the 8/10 SRM (a) radial and (b) tangential components at the unaligned position, and (c) radial and (d) tangential components at the aligned position.

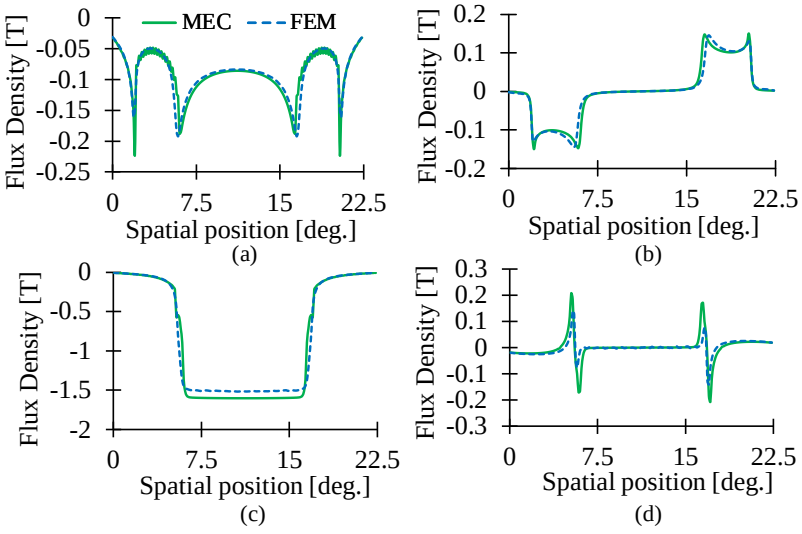

Figure 4.12: The flux density components in the airgap for 20 A excitation current of the 16/12 SRM (a) radial and (b) tangential components at the unaligned position, and (c) radial and (d) tangential components at the aligned position.

4.4.2 Phase Flux Linkage and Electromagnetic Torque

The static phase flux linkage and electromagnetic torque of 6/4, 6/16, 12/8, 8/6, 8/10, and 16/12 SRMs at different excitation currents for a half electrical cycle are presented in Figs. 4.13, 4.14, 4.15, 4.16, 4.17 and 4.18, respectively. The phase flux linkage profiles computed using MEC in Figs. 4.13, 4.14, 4.15, 4.16, 4.17 and 4.18 (a) are in good agreement with FEM results. The static electromagnetic torque characteristics of the MEC model match the FEM model results fairly, as evident in Figs.4.13, 4.14, 4.15, 4.16, 4.17 and 4.18 (b). There are minor deviations in the static electromagnetic torque characteristics between the MEC and FEM results which is due to the small errors in the airgap flux density characteristics.

4.5 Dynamic Characteristics of SRMs

The developed MEC model can be applied for dynamic analysis. For this purpose, the MEC model is extended to add voltage excitation feature, as (4.2.10) can only be applied for current excitation. The current is then regulated with hysteresis control based on the voltage excitation.

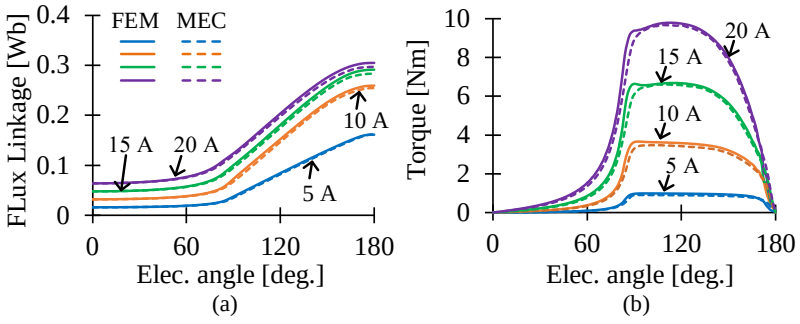

Figure 4.13: A half cycle of (a) static phase flux linkage and (b) static electromagnetic torque characterics of 6/4 SRM [2].

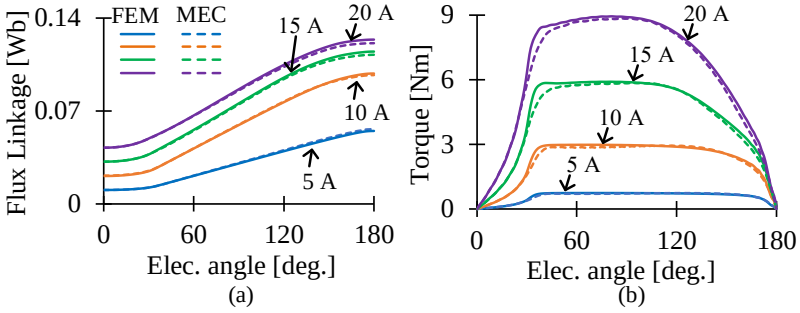

Figure 4.14: A half cycle of (a) static phase flux linkage and (b) static electromagnetic torque characterics of 6/16 SRM.

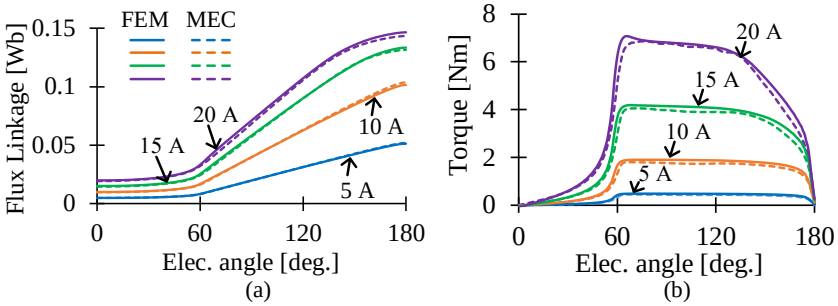

Figure 4.15: A half cycle of (a) static phase flux linkage and (b) static electromagnetic torque characterics of 12/8 SRM.

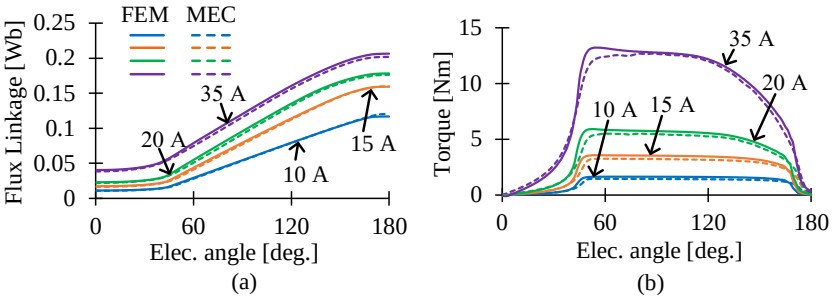

Figure 4.16: A half cycle of (a) static phase flux linkage and (b) static electromagnetic torque characterics of 8/6 SRM [2].

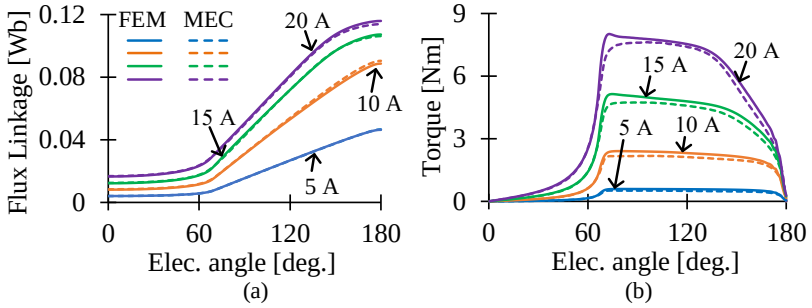

Figure 4.17: A half cycle of (a) static phase flux linkage and (b) static electromagnetic torque characterics of 8/10 SRM.

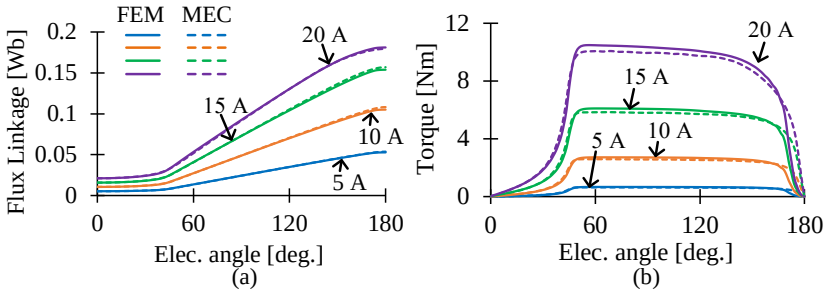

Figure 4.18: A half cycle of (a) static phase flux linkage and (b) static electromagnetic torque characterics of 16/12 SRM.

4.5.1 Proposed MEC-based Dynamic Model

The relationship between phase voltages and currents in the windings is given by

$$\boldsymbol{V}_{ph} = \boldsymbol{R}_s \boldsymbol{I}_s + \frac{d}{dt}\boldsymbol{\psi} \tag{4.5.1}$$

where $\boldsymbol{R}_s$ is a diagonal matrix which contains phase resistances. Equation (4.5.1) is discretized to calculate the flux linkage $\boldsymbol{\psi}$ at $(k+1)^{\text{th}}$ iteration

$$\boldsymbol{\psi}_{k+1} = \boldsymbol{\psi}_k + \Big(\boldsymbol{V}_{ph,k} - \boldsymbol{R}_s \boldsymbol{I}_{s,k}\Big)\Delta t. \tag{4.5.2}$$

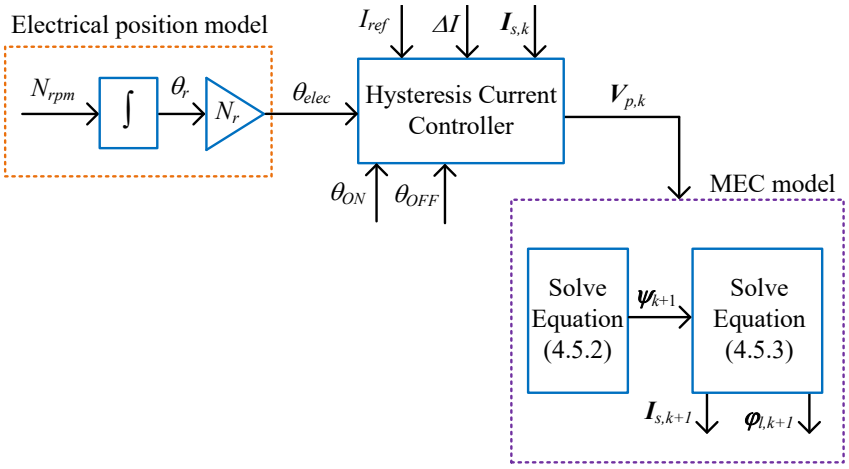

Figure 4.19: The solution process of the dynamic SRM model.

The dynamic equation for an SRM is deduced from (4.2.10) and (4.3.5)

$$\boldsymbol{r}_d = \begin{bmatrix} \boldsymbol{R} & -s_f \boldsymbol{N} \\ p\boldsymbol{N}^T & \boldsymbol{0} \end{bmatrix} \begin{bmatrix} \boldsymbol{\phi}_l \\ \boldsymbol{I}_s \end{bmatrix} - \begin{bmatrix} \boldsymbol{0} \\ \boldsymbol{\psi} \end{bmatrix}. \tag{4.5.3}$$

The scaling factor s_f is applied to avoid ill-conditions in (4.5.3) that can occur due to the difference between the order of magnitudes in $\boldsymbol{\phi}_l$ and $\boldsymbol{I}_s$. The value of the s_f is determined heuristically. Gauss-Newton method is applied to solve (4.5.3) iteratively. The solution process of the dynamic model is shown in Fig. 4.19. The rotor position θ_r is calculated by integrating the rotation speed N_{rpm} of the SRM. The electrical angle θ_{elec} is obtained by multiplying θ_r with the number of rotor poles N_r and applying the phase shift between phases. A hysteresis current controller is used to control the current based on the θ_{elec}, turn-on angle θ_{ON}, turn-off angle θ_{OFF}, phase excitation currents $\boldsymbol{I}_{s,k}$, reference current I_{ref}, and hysteresis band ΔI. The reference current I_{ref} can be either a constant or a function of θ_{elec}. $\boldsymbol{V}_{ph,k}$ is the output of the current

controller. Then, (4.5.2) is applied to determine the value of $\boldsymbol{\psi}_{k+1}$. Finally, (4.5.3) is solved to obtain $\boldsymbol{\phi}_{l,k+1}$ and $\boldsymbol{I}_{s,k+1}$. The phase currents, and self and mutual flux linkages during the phase commutation are considered in (4.5.2). The mutual flux linkages calculated in (4.5.2) are used in (4.5.3) to consider the mutual coupling effects while solving for the phase currents.

4.5.2 Dynamic Current and Electromagnetic Torque

The calculated dynamic current and generated electromagnetic torque of 6/4, 6/16, 12/8, 8/6, 8/10, and 16/12 SRMs for one electrical cycle are shown in Figs. 4.20, 4.21, 4.22, 4.23, 4.24 and 4.25, respectively. I_{ref} is kept constant at the given reference current during all of these simulations. In all simulations, θ_r is zero when the rotor is at the align position with phase-A and the θ_{elec} is zero when phase-A is at the unaligned position. The conduction angles θ_{ON} and θ_{OFF} are refered to phase-A.

The waveforms in Figs. 4.20, 4.21, 4.22, 4.23, 4.24 and 4.25 (a) and (b) are dynamic current and electromagnetic torque, respectively for the case where the current can be controlled at the given I_{ref}. The waveforms in (c) and (d) correspond to the dynamic current and electromagnetic torque at a higher speed point. The current cannot be controlled at the given I_{ref} at those operating points as the induced voltage is higher than the DC link voltage. It can be observed that the dynamic current and the electromagnetic torque waveforms acquired from the MEC model in Figs. 4.20, 4.21, 4.22, 4.23, 4.24, and 4.25 reasonably match with the results obtained from FEM simulations. FEM models are developed in JMAG and voltage excitation is used by implementing an asymmetric bridge converter. Table 4.1 shows the maximum percentage errors for the root-mean squared (RMS) current and average torque between

the MEC and FEM models for the considered SRMs. The maximum average torque error was 8.6 % and the maximum RMS current error in the MEC model was 10.5 %. The errors in the dynamic current waveforms have occured due to minor deviations in the flux linkage and the induced voltage between MEC and FEM models.

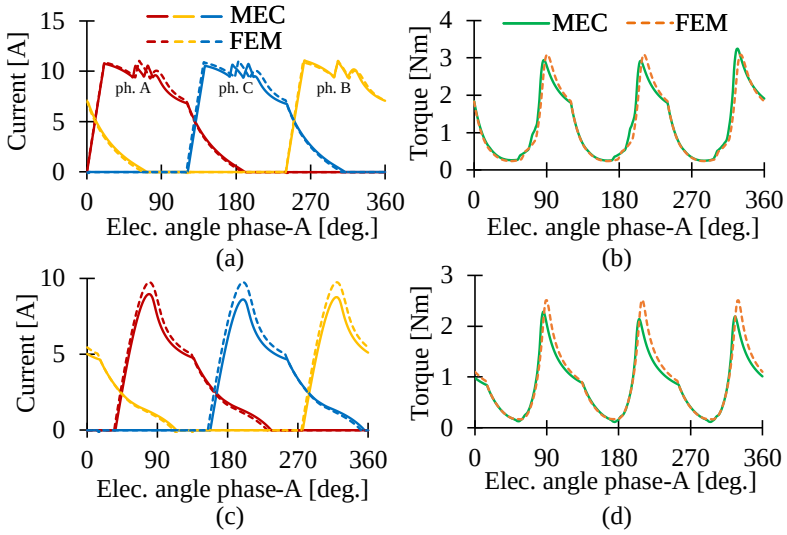

Figure 4.20: Dynamic simulation of 6/4 SRM (a) phase current, (b) electromagnetic torque at $I_{ref} = 10$ A, $\theta_{ON} = 0°$, $\theta_{OFF} = 120°$ and $N_{rpm} = 7500$ rpm, and (c) phase current, (d) electromagnetic torque at $I_{ref} = 10$ A, $\theta_{ON} = 35°$, $\theta_{OFF} = 135°$ and $N_{rpm} = 12000$ rpm.

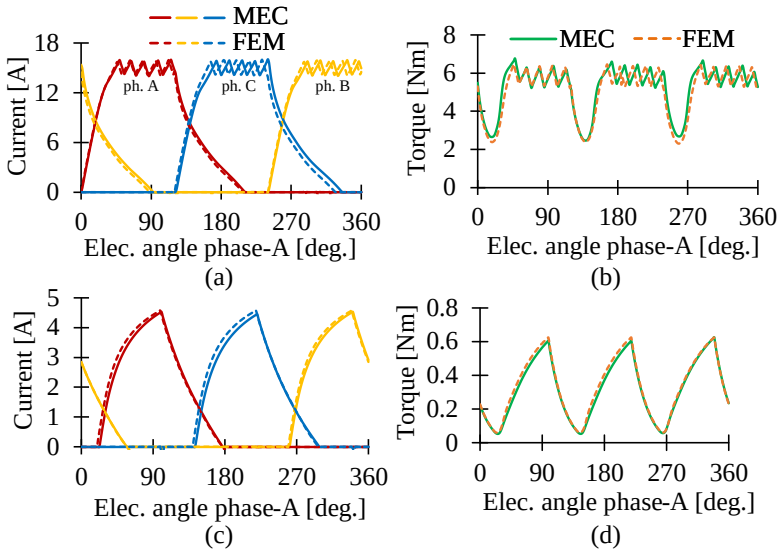

Figure 4.21: Dynamic simulation of 6/16 SRM (a) phase current, (b) electromagnetic torque at $I_{ref} = 15$ A, $\theta_{ON} = 0°$, $\theta_{OFF} = 120°$ and $N_{rpm} = 3000$ rpm, and (c) phase current, (d) electromagnetic torque at $I_{ref} = 5$ A, $\theta_{ON} = 20°$, $\theta_{OFF} = 100°$ and $N_{rpm} = 8000$ rpm.

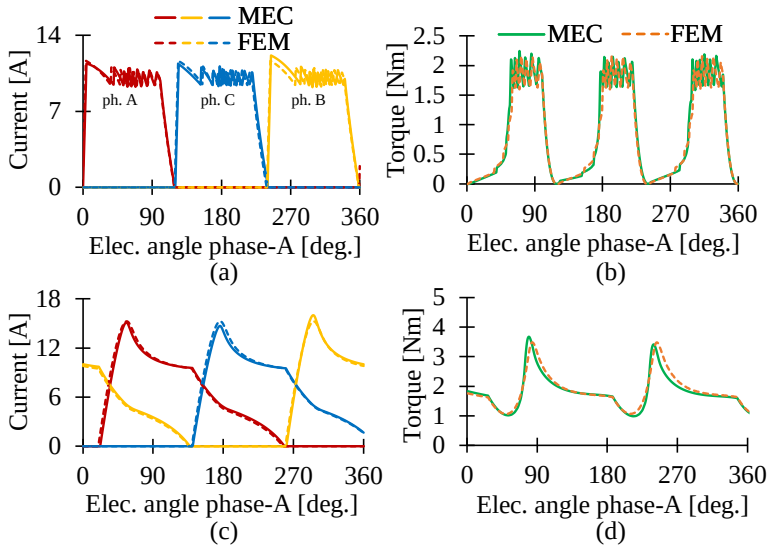

Figure 4.22: Dynamic simulation of 12/8 SRM (a) phase current, (b) electromagnetic torque at $I_{ref} = 10$ A, $\theta_{ON} = 0°$, $\theta_{OFF} = 120°$ and $N_{rpm} = 2500$ rpm, and (c) phase current, (d) electromagnetic torque at $I_{ref} = 20$ A, $\theta_{ON} = 20°$, $\theta_{OFF} = 120°$ and $N_{rpm} = 10000$ rpm.

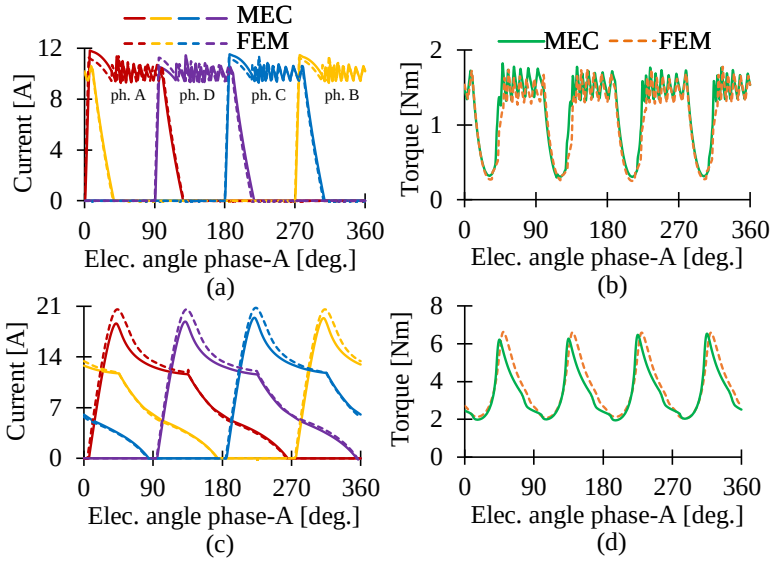

Figure 4.23: Dynamic simulation of 8/6 SRM (a) phase current, (b) electromagnetic torque at $I_{ref} = 10$ A, $\theta_{ON} = 0°$, $\theta_{OFF} = 100°$ and $N_{rpm} = 3500$ rpm, and (c) phase current, (d) electromagnetic torque at $I_{ref} = 20$ A, $\theta_{ON} = 5°$, $\theta_{OFF} = 135°$ and $N_{rpm} = 10000$ rpm.

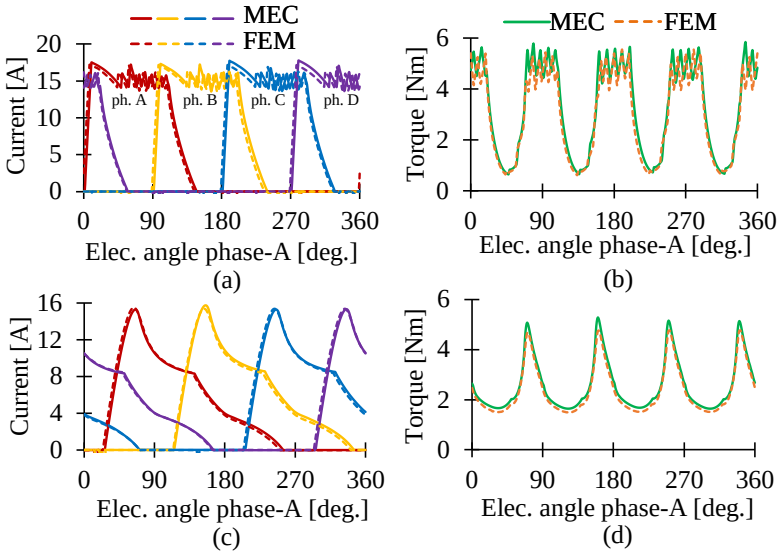

Figure 4.24: Dynamic simulation of 8/10 SRM (a) phase current, (b) electromagnetic torque at $I_{ref} = 15$ A, $\theta_{ON} = 0°$, $\theta_{OFF} = 110°$ and $N_{rpm} = 3000$ rpm, and (c) phase current, (d) electromagnetic torque at $I_{ref} = 15$ A, $\theta_{ON} = 25°$, $\theta_{OFF} = 140°$ and $N_{rpm} = 10000$ rpm.

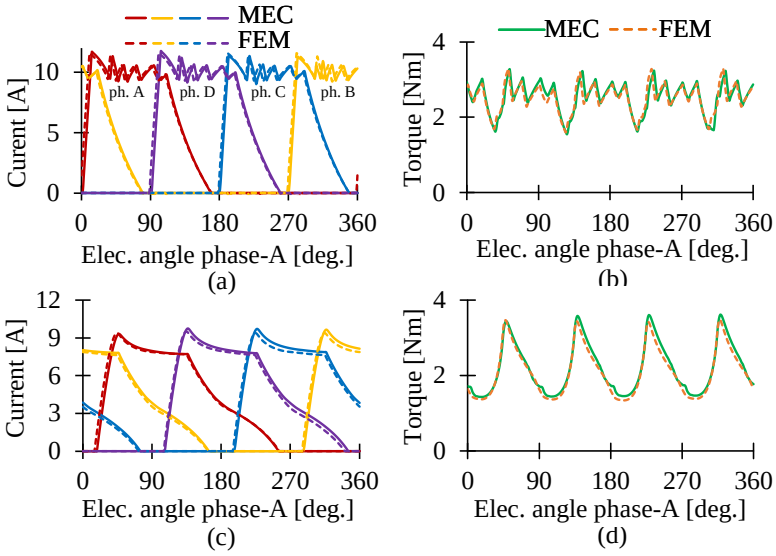

Figure 4.25: Dynamic simulation of 16/12 SRM (a) phase current, (b) electromagnetic torque at $I_{ref} = 10$ A, $\theta_{ON} = 0°$, $\theta_{OFF} = 110°$ and $N_{rpm} = 4000$ rpm, and (c) phase current, (d) electromagnetic torque at $I_{ref} = 10$ A, $\theta_{ON} = 16°$, $\theta_{OFF} = 136°$ and $N_{rpm} = 8000$ rpm.

In applications such as torque sharing function (TSF) for SRMs, I_{ref} varies with the rotor position. Fig. 4.26 shows the calculated dynamic current of 8/6 and 12/8 SRMs for a variable current reference and the generated electromagnetic torque. A cubic TSF is applied to obtain the current references in Figs. 4.26 (a) and (c). In Fig. 4.26 (a), I_{ref} is generated to produce 2 Nm average torque at 3500 rpm. The parameters of the TSF are $\theta_{ON} = 34°$, $\theta_{OFF} = 125°$ and, commutation angle, $\theta_{com} = 35°$. The current reference in Fig. 4.26 (c) is obtained to generate 4 Nm torque at 2500 rpm with TSF parameters $\theta_{ON} = 47°$, $\theta_{OFF} = 165°$ and $\theta_{com} = 15°$. As shown in Fig. 4.26 (a) and (c), obtained currents from MEC and FEM models show a good agreement with each other. The computed currents both with MEC and FEM models have a tracking error at the turn-off. This error occurs since the example phase current reference cannot be tracked due to the voltage dynamics. The

agreement between the current waveforms of the MEC and FEM models demonstrate that MEC model can calculate the dynamic current even at that condition.

The generated torque of the 12/8 SRM in Fig. 4.26 (d) shows good agreement with the torque calculated from the FEM. The MEC model of the 8/6 SRM has predicted a higher peak torque as shown in Fig. 4.26 (b). The main reason is that the MEC method calculates slightly higher flux density in the airgap compared to the FEM for a similar current. The maximum percentage errors of the RMS current and average torque in the considered SRMs with respect to the FEM results are shown in Table 4.2. In the MEC technique, the maximum RMS error in the calculated current is 1 %, and the maximum error in the average torque is 1.67 %.

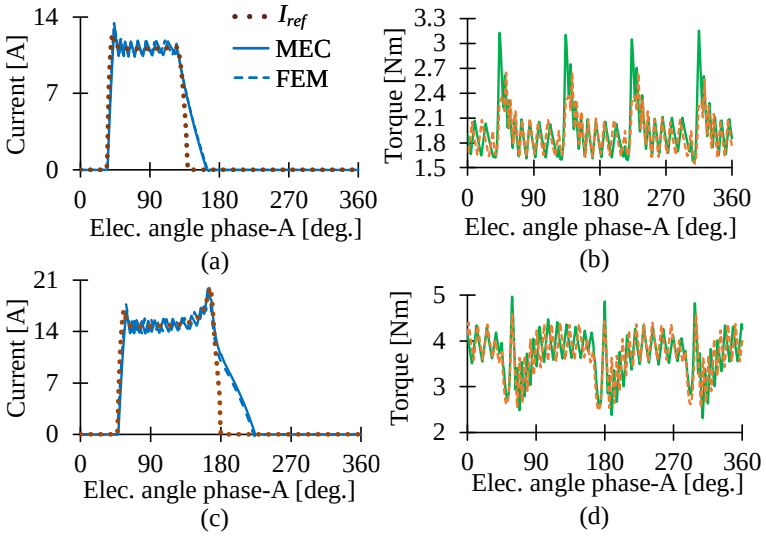

Figure 4.26: Variable I_{ref} for 8/6 SRM at $N_{rpm} = 3500$ rpm (a) phase current, (b) electromagnetic torque, and variable I_{ref} for 12/8 SRM at $N_{rpm} = 2500$ rpm (c) phase current, (d) electromagnetic torque.

4.5.3 Magnetic Flux Density

Using the dynamic currents in Figs. 4.20, 4.21 and 4.22 (a), magnetic flux density contours in the 3-phase 6/4, 6/16 and 12/8 SRMs can be calculated in the MEC and FEM models. In Figs. 4.27, 4.28 and 4.29 (a) and (b), flux density contours are plotted for 6/4, 6/16 and 12/8 SRMs, respectively at rotor positions 22.5°, 5.625° and 20.625°. The magnetic flux density contours obtained from MEC model are in good agreement with the contours obtained from the FEM. As observed in Figs. 4.27 and 4.28 (a) and (b), both phase-C and phase-B conduct in 6/4 and 6/16 SRMs at the rotor positions 22.5° and 5.625°. Only phase-B conducts in 12/8 SRM at 11.25° rotor position, as shown in Fig. 4.22 (a) and (b). The radial and tangential airgap flux

Table 4.1: Maximum error in root-mean squared (RMS) current and average torque (constant I_{ref}).

Pole configuration	RMS current error	Avg. torque error
3-phase SRMs		
6/4	10.5 %	7.1 %
6/16	4.9 %	3.3 %
12/8	2.9 %	2.1 %
4-phase SRMs		
8/6	3.4 %	5.8 %
8/10	1.3 %	8.6 %
16/12	2.1 %	3.6 %

Table 4.2: Maximum error in RMS current and average torque (variable I_{ref}).

Pole configuration	RMS current error	Avg. torque error
8/6	1 %	1.67 %
12/8	0.7 %	0.2 %

density waveforms for 3-phase 6/4, 6/16 and 12/8 SRMs at the given rotor positions are shown in Figs. 4.27, 4.28 and 4.29 (c) and (d). For 6/4 and 6/16 SRMs, spatial position is between 0 to 180°, as those are two-pole motors. The spatial position for 12/8 SRM is between 0 to 90° as it is a four-pole motor. Radial and tangential components of the flux density waveforms obtained from the MEC models show fair agreement with flux density waveforms obtained from the FEM models. Minor errors can be observed in the flux density computed from the MEC model of the 6/16 SRM near the spatial positions 30° and 150° as shown in Figs. 4.28 (c) and (d). In 12/8 SRM, small errors can be observed near the 30° spatial position according to Figs. 4.29 (c) and (d). Those errors are due to the coarse mesh density and geometry approximation errors.

For the 4-phase 8/6, 8/10, and 16/12 SRMs, the flux density contours are also calculated in the MEC and FEM models at the rotor positions 17.5°, 10.5°, and 8.75°, for the dynamic current waveforms in Figs. 4.23, 4.24, and 4.25 (a), respectively. The magnetic flux density contours obtained from MEC model are in good agreement with those obtained from the FEM model. It can be observed in Fig. 4.30 (a), (b) and Fig. 4.32 (a) and (b), that both phase-C and phase-B conduct in the 8/6 and 16/12 SRMs. As shown in Fig. 4.31 (a) and (b), phase-C and phase-D conduct in the 8/10 SRM. Radial and tangential airgap flux density waveforms are shown in Figs. 4.30, 4.31, 4.32 (c) and (d). As shown in Figs. 4.30 and 4.31 (a) and (b), for the 8/6 and 8/10 SRMs, the spatial position is between 0° and 180°, as these are two-pole motors. The spatial position for 16/12 SRM is between 0 to 90°, as shown in Fig. 4.32 (a) and (b). The flux density waveforms from the MEC models show good match with the ones from the FEM models. There are some minor errors in the flux density

waveforms of the 8/10 SRM near the spatial position 110°, as shown in Figs. 4.31 (c) and (d).

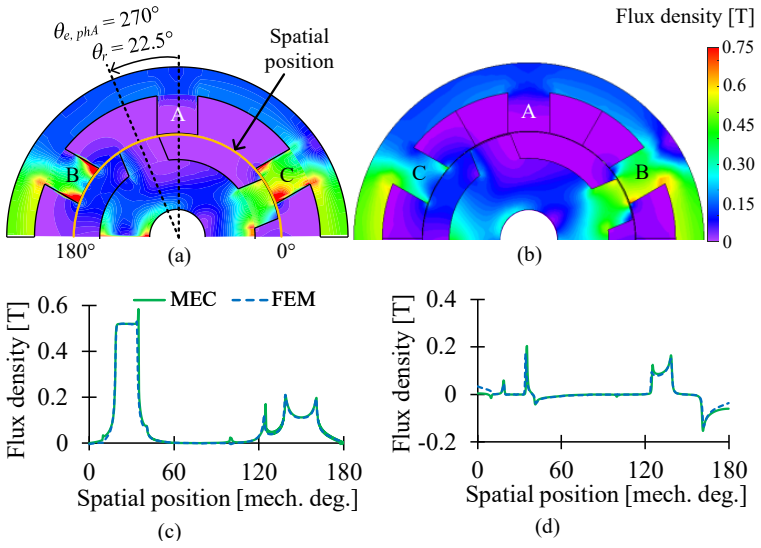

Figure 4.27: Magnetic flux density of 6/4 SRM at $\theta_r = 22.5°$ and $\theta_{e,phA} = 270°$ (a) flux density contours from MEC, (b) flux density contours from FEM, (c) radial component of the airgap flux density and (d) tangential component of the airgap the flux density.

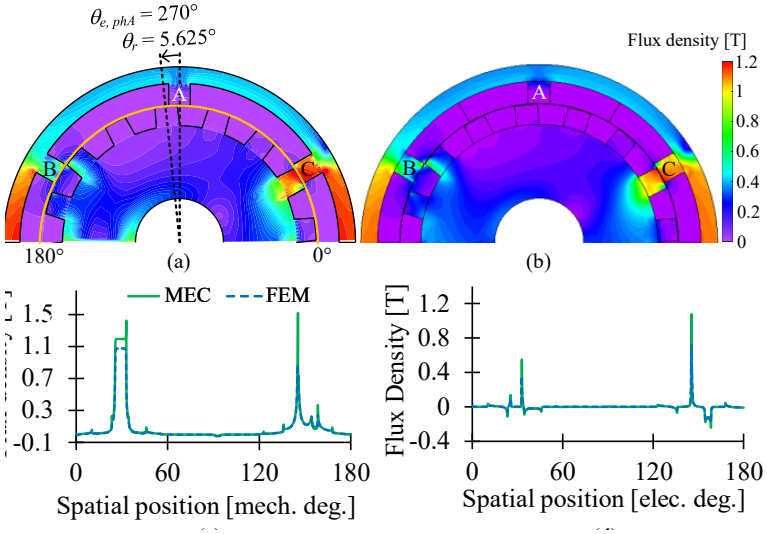

Figure 4.28: Magnetic flux density of 6/16 SRM at $\theta_r = 5.625°$ and $\theta_{e,phA} = 270°$ (a) flux density contours from MEC, (b) flux density contours from FEM, (c) radial component of the airgap flux density and (d) tangential component of the airgap the flux density.

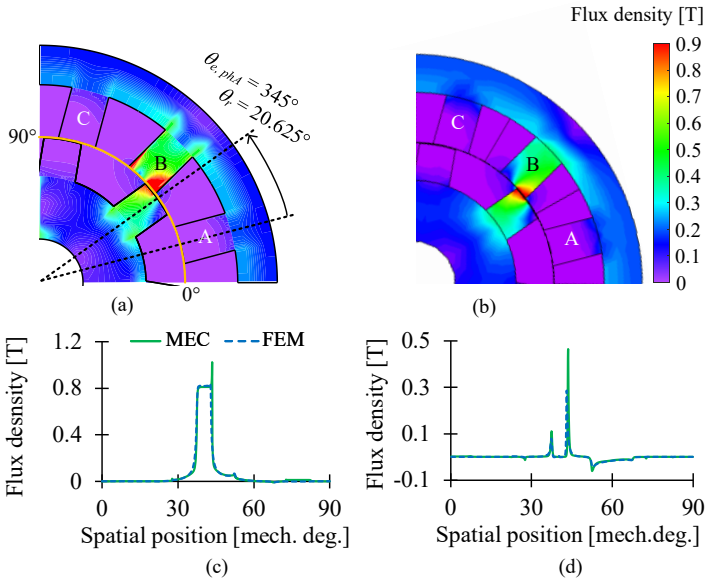

Figure 4.29: Magnetic flux density of 12/8 SRM at $\theta_r = 20.625°$ and $\theta_{e,phA} = 345°$ (a) flux density contours from MEC, (b) flux density contours from FEM, (c) radial component of the airgap flux density and (d) tangential component of the airgap the flux density.

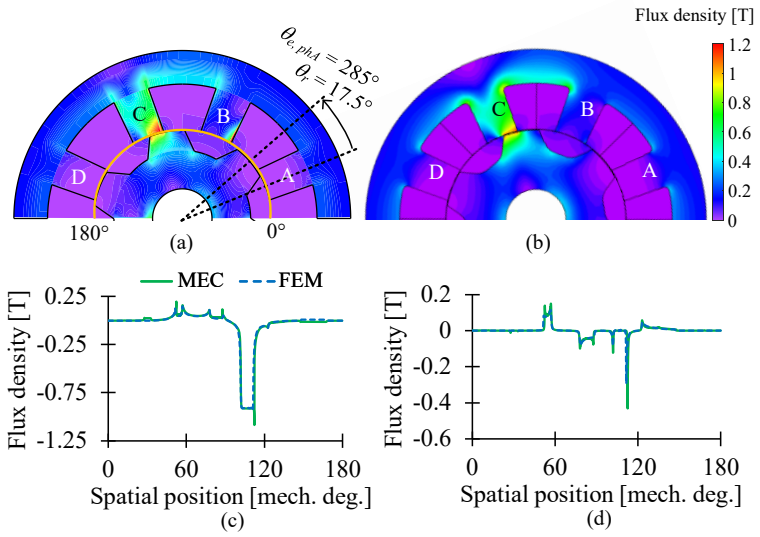

Figure 4.30: Magnetic flux density of 8/6 SRM at $\theta_r = 17.5°$ and $\theta_{e,phA} = 285°$ (a) flux density contours from MEC, (b) flux density contours from FEM, (c) radial component of the airgap flux density and (d) tangential component of the airgap the flux density.

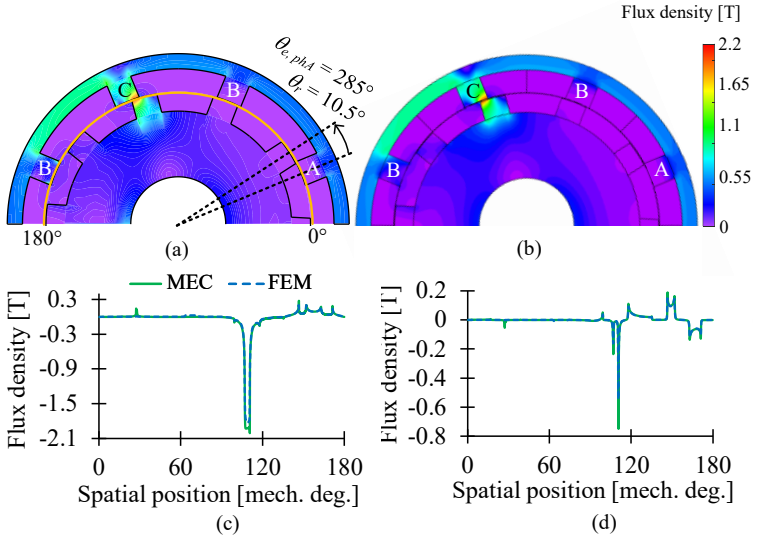

Figure 4.31: Magnetic flux density of 8/10 SRM at $\theta_r = 10.5°$ and $\theta_{e,phA} = 285°$ (a) flux density contours from MEC, (b) flux density contours from FEM, (c) radial component of the airgap flux density and (d) tangential component of the airgap the flux density.

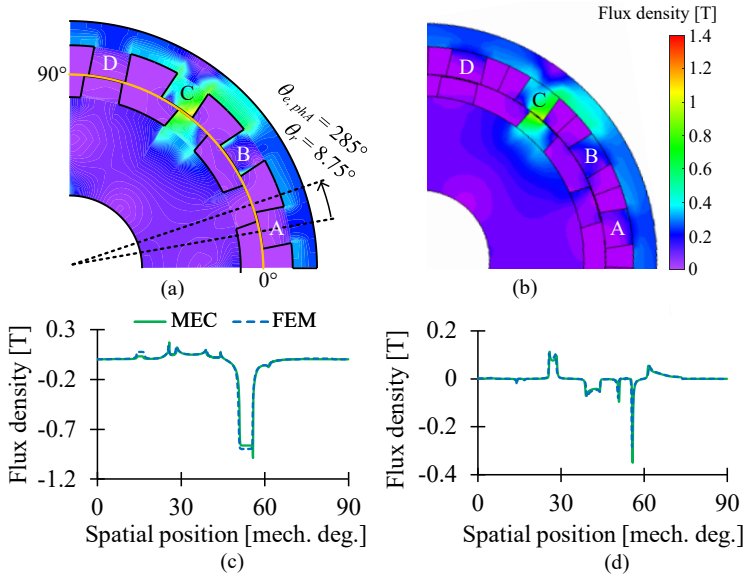

Figure 4.32: Magnetic flux density of 16/12 SRM at $\theta_r = 8.75°$ and $\theta_{e,phA} = 285°$ (a) flux density contours from MEC, (b) flux density contours from FEM, (c) radial component of the airgap flux density and (d) tangential component of the airgap the flux density.

The accuracy of the flux density calculation in the MEC method can be improved by decreasing the rotor step angle, as that increases the number of mesh elements in the airgap. The number of complex mesh elements at the stator and rotor pole teeth edges can also be increased to reduce the geometry approximation and also to reduce field calculation errors. Besides the accuracy of the field calculation can be improved by utilizing a higher number of mesh elements in the stator and rotor poles since those regions experience higher local saturation.

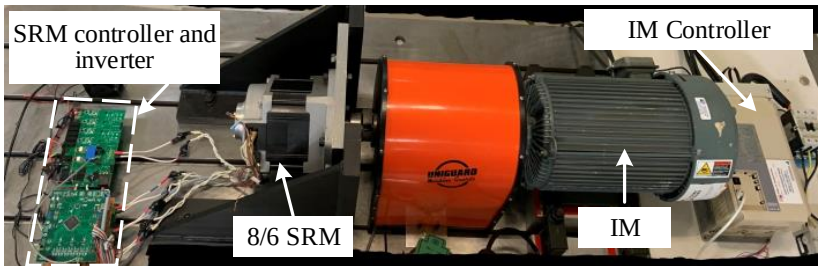

Figure 4.33: Experimental test setup.

4.6 Experimental Validation

Experimental tests have been conducted to further validate the simulated performance of the SRMs using the proposed MEC model. A 4-phase 8/6 SRM is used to obtain the static flux linkage characteristics and dynamic current. Flux density distribution inside the 8/6 SRM is also obtained by exciting the MEC and FEM models using the experimental phase currents. The main parameters of the 8/6 SRM is shown in Table 4.3. The experimental results are compared with corresponding MEC and FEM results. The test setup prepared for the experimental analysis is shown in Fig. 4.33. An asymmetric bridge converter drives the SRM and the current is controlled with hysteresis controller. An induction motor drive is used to apply load to the SRM drive.

Table 4.3: Parameters of the 8/6 SRM in the laboratory.

Parameter	Value
Maximum output power	5.2 kW
Maximum speed	6000 rpm
Maximum reference current	35 A
Phase resistance	0.08 ohm
DC-link voltage	300 V

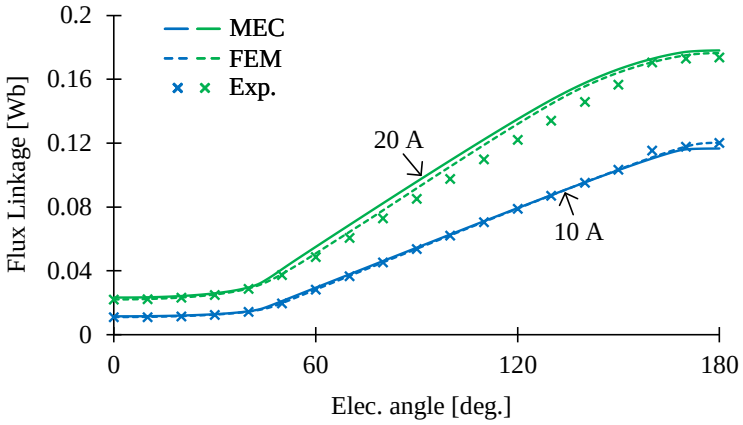

Figure 4.34: Experimental static flux linkage of 8/6 SRM.

4.6.1 Static Phase Flux Linkage Characteristics

The static phase flux linkage characteristics have been obtained through locked rotor tests. Constant voltage is applied to a single phase of the SRM at different rotor positions and the phase current has been recorded. The recorded voltages and currents have been processed using (4.5.3) to determine the phase flux linkage at the given rotor position. The experimental static phase flux linkage characteristics of the 8/6 SRM at 10 A and 20 A excitation currents are shown in Fig. 4.34. The static flux linkage of 8/6 SRM at 10 A from MEC and FEM models shows good agreement with the experimental results. Table 4.4 compares the RMSE calculated from MEC and FEM models with respect to measured static flux linkage.

Table 4.4: Maximum RMSE of the static flux linkage compared to the measured flux linkage.

RMSE	Flux linkage at 10 A	Flux linkage at 20 A
MEC	0.15 %	0.81 %
FEM	0.09 %	0.56 %

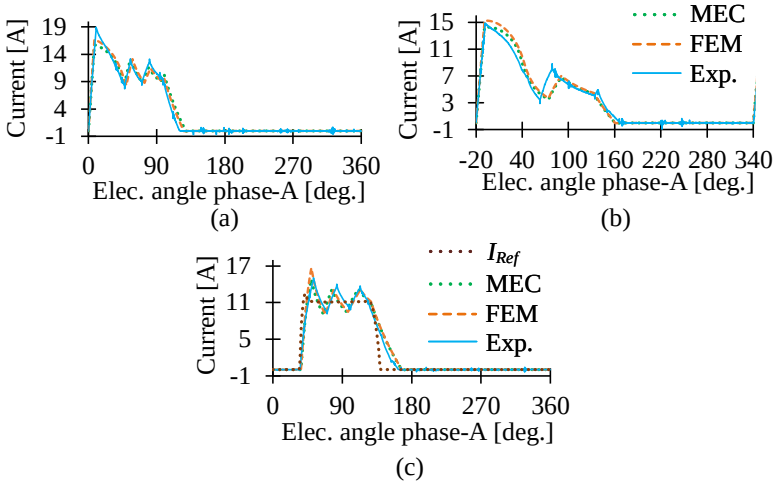

Figure 4.35: Experimental dynamic current of 8/6 SRM (a) $I_{ref} = 10$ A, $\theta_{ON} = 0°$, $\theta_{OFF} = 100°$ at $N_{rpm} = 3500$ rpm, (b) $I_{ref} = 5$ A, $\theta_{ON} = -20°$, $\theta_{OFF} = 140°$ at $N_{rpm} = 5500$ rpm and (c) variable I_{ref} at $N_{rpm} = 3500$ rpm.

4.6.2 Dynamic Current

The hysteresis current controller implemented in the SRM controller is used to obtain the dynamic characteristics of the 8/6 SRM. The frequency of the current controller is 50 kHz, and the hysteresis band has been set to 2 A. The same parameters are set in the simulated MEC and FEM model's hysteresis current controllers for a fair comparison. The measured dynamic current waveforms of the 8/6 SRM for constant and variable I_{ref} are presented in Fig. 4.35. In Fig. 4.35 (a) and (b), I_{ref} was set to 10 A and 5 A constants, respectively. The conduction angles are set to $\theta_{ON} = 0°$, $\theta_{OFF} = 100°$ at 3500 rpm and $\theta_{ON} = -20°$, $\theta_{OFF} = 140°$ at 5500 rpm. I_{ref} in Fig. 4.35 (c) was generated using cubic TSF to produce 2 Nm average torque with the TSF parameters $\theta_{ON} = 34°$, $\theta_{OFF} = 125°$ and, commutation angle, $\theta_{com} = 35°$. The computed currents using MEC and FEM techniques show good agreement with the measured currents. The maximum RMS current error is less than 2% with respect to

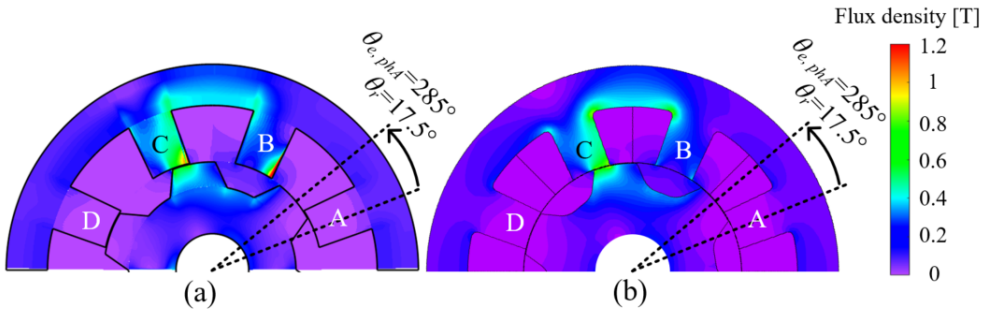

Figure 4.36: Flux density distribution in the 8/6 SRM at $\theta_r = 17.5°$ (a) MEC model and (b) FEM model.

the experimental phase currents.

Flux density distribution inside the 8/6 SRM is obtained by exciting the MEC and FEM models using the experimental phase currents in Fig. 4.35 (a). Fig. 4.36 shows the comparison of the obtained flux density plots at $\theta_r = 17.5°$. Flux density distribution from the MEC model closely follows the distribution in the FEM. The MEC model results show small discrepancies near the stator pole edges of phases B and C due to geometry approximation errors.

4.7 Summary

This chapter has presented a reluctance mesh-based MEC method for modeling SRMs. The MEC models of 3-phase 6/4, 6/16, and 12/8 SRMs and 4-phase 8/6, 8/10, and 16/12 SRMs have been modeled using the proposed method. The meshing, MMF calculation, assembling the MEC, and field solution technique was discussed. The magnetic flux density, static characteristics, and dynamic characteristics were calculated using the proposed method. The MEC models were validated using the results from corresponding FEM models and experiments.

Chapter 5

Radial Force Density Calculation of SRMs using Reluctance Mesh-Based MEC Technique

5.1 Introduction

Acoustic noise and vibration is one of the shortcomings of an SRM. Various techniques have been proposed to reduce the acoustic noise of SRMs. The acoustic noise can be reduced by changing the shape of the stator back-iron [125], introducing windows in the stator and rotor poles [126, 127], using distributed airgap [128], and by applying radial force shaping [129]. In an SRM, the vibration of the stator can have different mode shapes, and each mode shape has a specific frequency. Resonance and, hence, higher vibration can occur when the forcing frequency of a specific circumferential order of a radial force harmonic coincides with the natural frequency of a mode shape with the same circumferential order [130]. It is crucial to identify the magnitudes of

the radial force density harmonics, and their vibration modes and frequencies when analyzing and designing an SRM.

Different analytical techniques have been proposed to calculate the radial forces in the airgap for SRMs. In [131–134], analytical expressions have been developed for SRMs to calculate radial forces. These models have ignored the magnetic saturation and also neglected the mutual coupling effects. FEM is a more accurate technique to calculate the radial force density in an SRM. In [130], [135] and [136], FEM has been applied to calculate the radial force density. The proposed FEM-based method in [135] consists of two steps: (i) developing static LUTs using FEM and (ii) running dynamic simulations in MATLAB using the LUTs to calculate the radial force densities. This process can consider the nonlinear characteristics of the SRM. However, the process in [135] can be complex and time consuming to implement in SRM design since it requires redeveloping the static LUTs when the geometry is changed. The MEC method is a promising alternative to FEM and it has reasonable accuracy [10, 12].

The magnitudes and the harmonics of the radial force density waveform of an SRM depend on the pole configuration, motor geometry, and phase current. The conventional MEC technique can be challenging to calculate the radial force density in an SRM design process as it requires to configure a predefined magnetic flux path for each pole configuration being analyzed. In [137], the conventional MEC technique has been applied to calculate the radial forces in a 12/8 SRM. However, the reluctance mesh-based MEC method has not been widely used to calculate the radial forces in an SRM, even though it has significant advantages over the conventional MEC method.

In this chapter, the proposed reluctance mesh-based MEC models of 3-phase 6/4, 6/16, and 12/8 SRMs and 4-phase 8/6, 8/10, and 16/12 SRMs has been utilized for

calculating the radial force density. The radial force density and stator radial force are calculated using the obtained dynamic characteristics and Maxwell Stress Tensor method. The harmonic spectrum of the radial force density waveforms is obtained using 2D Fast Fourier transform (FFT). The results calculated from the MEC models are verified using the FEM models.

5.2 Proposed Method for Radial Force Calculation

The phase currents create radial and tangential flux densities in the airgap. The radial and tangential flux densities in the airgap are computed by solving the developed MEC method-based dynamic model. Maxwell Stress Tensor is then applied to calculate the radial force density waveform. 2D Fourier series is used to extract the harmonics of the radial force density waveform calculated from the MEC model.

5.2.1 Calculation of the Radial and Tangential Forces

In 2D analysis, the total radial force exerted on one stator pole can be calculated by integrating the radial force density over one stator pole pitch:

$$F_{rad} = \nu_0 a \int_{l_{fs}} \frac{1}{2}(B_{rad}^2 - B_{tan}^2) dl. \tag{5.2.1}$$

The line integral in (5.2.1) is evaluated along the arc l_{fs}. As shown in Fig. 5.1, l_{fs} is chosen in the middle of the stationary airgap mesh closer to the stator. The stationary airgap mesh is divided into n_s number of elements along the tangential direction. Thus, the integral in (5.2.1) can be approximated as a summation of all

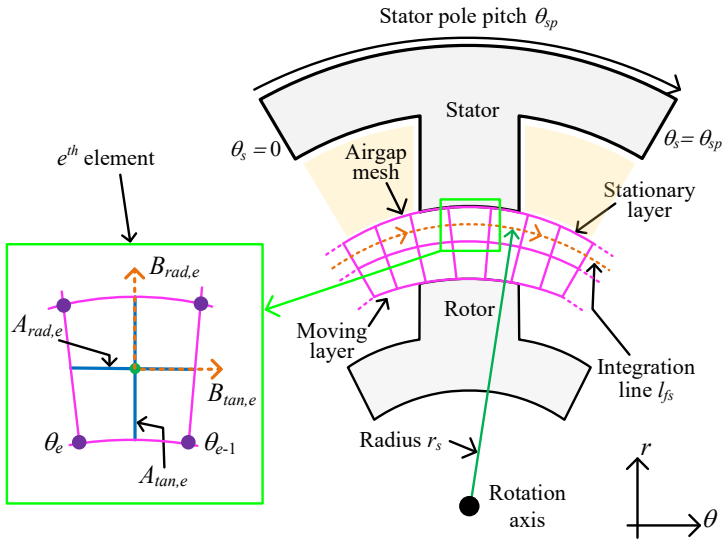

Figure 5.1: Choosing an integration path for computing the radial force.

the stationary elements in the airgap,

$$F_{rad} = \frac{a\nu_0}{2} \sum_{e=1}^{n_s} (B_{rad,e}^2 - B_{tan,e}^2)(\theta_e - \theta_{e-1}). \tag{5.2.2}$$

5.2.2 Radial Force Density Decomposition

The radial force density in the airgap vary with the rotor position or time, and the spatial position of the airgap. Therefore, radial force density can be considered as a spatial waveform varying in time. Different harmonics of the radial force density waveform can excite different circumferential vibration modes of the stator. Therefore, calculating the magnitudes of radial force density harmonics is necessary for acoustic noise analysis in an SRM. 2D Fourier series is applied to decompose the radial force density waveform obtained from the MEC method into its harmonics [130]:

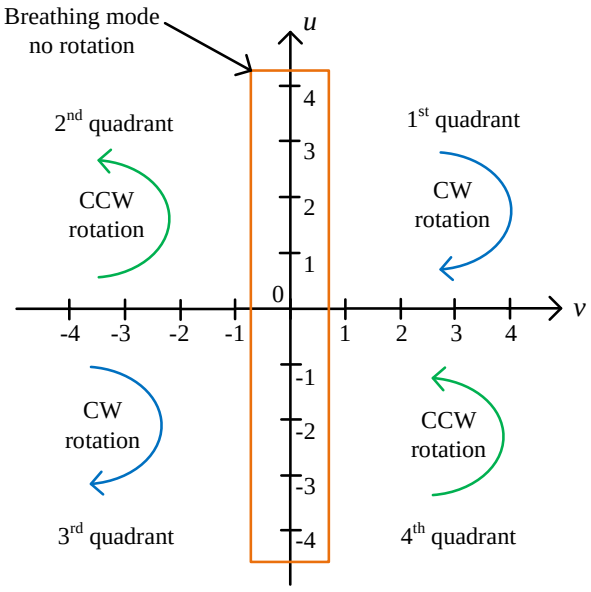

Figure 5.2: Four-quadrant plane for representing the harmonics with spatial and temporal orders.

$$\sigma_{rad}(\theta_r, \theta_s) = \sum_{u=-\infty}^{\infty} \sum_{v=-\infty}^{\infty} C_{u,v} \cos(u\theta_r + v\theta_s + \gamma_{u,v}) \tag{5.2.3}$$

where u and v are integers and they define the spatial order and the temporal order of a radial force density harmonic, respectively. $C_{u,v}$ and $\gamma_{u,v}$ are the Fourier coefficient and phase angle of the u^{th} and v^{th} radial force density harmonic. The harmonic spectrum of the radial force density waveform can be represented in a four-quadrant plane as shown in Fig. 5.2. The harmonics in the 1$^{\text{st}}$ and 3$^{\text{rd}}$ quadrants rotate in the clockwise (CW) direction and the harmonics in the 2$^{\text{nd}}$ and 4$^{\text{th}}$ quadrants rotate in the counter clockwise (CCW) direction based on (5.2.3). From the properties of the 2D Fourier series, $C_{(u,v)}$ equals to $C_{(-u,-v)}$. Hence, the magnitudes of the harmonics in 1$^{\text{st}}$ and 3$^{\text{rd}}$ quadrants are same and the magnitudes of the harmonics in 2$^{\text{nd}}$ and 4$^{\text{th}}$ quadrants are same [130].

Different circumferential vibration modes excited by the radial force density waveform harmonics are shown in Fig. 5.3. As shown in Fig. 5.3 (a), mode-0 expands and contracts the stator along the radial direction. It is called the breathing mode (BM) and it does not have rotation [129]. The existence of modes 2 and 4 depends on the number of magnetic poles of the SRM [138]. Mode-2 corresponds to the spatial orders $v = \pm 2$, and it is the main vibration mode of the two-pole SRMs such as 6/4, 6/16, 8/10 and 8/6. Also, other vibration modes corresponding to the spatial orders with multiples of two (e.g., $v = \pm 4, \pm 6, \pm 8...$) can be excited in a 2-pole SRM. Mode-4 corresponds to the spatial orders $v = \pm 4$, and it is the main vibration mode of the 4-poles SRMs such as 12/8 and 16/12. Other vibration modes corresponding to the spatial orders with multiples of four (e.g., $v = \pm 8, \pm 12, \pm 16...$) can be excited in a 4-pole SRM.

In the four-quadrant plane, the temporal orders corresponding to each spatial order are spaced with the number of strokes. The number of strokes can be calculated using (2.3.2). The excitation frequencies of the radial force density harmonics corresponding to different temporal orders are called the forcing frequencies, and they are

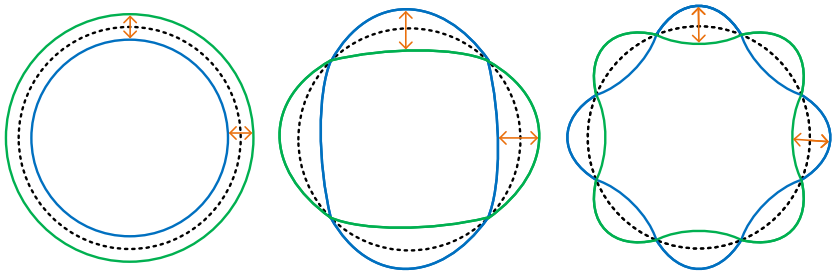

Figure 5.3: Circumferential modes of the stator (a) mode-0, (b) mode-2 and (c) mode-4.

defined as

$$f_{fc} = |u| f_{mech}. \tag{5.2.4}$$

As in (5.2.4), forcing frequencies of the radial force density harmonics depend on the rotational speed of the SRM.

5.3 Case Studies

This section presents calculated dynamic currents from the MEC models of 3-phase 6/4, 6/16, and 12/8 SRMs and 4-phase 8/6, 8/10 and 16/12 SRMs. Obtained radial forces and radial force density waveforms with the dynamic current excitation are presented. The four-quadrant harmonic spectrums of each radial force density waveform are shown. The results are compared with the corresponding results from the FEM models. The FEM models are developed in JMAG, and the dynamic models in JMAG are implemented by voltage excitation of SRMs using an asymmetric bridge converter.

5.3.1 Dynamic Current and Radial Force

Calculated dynamic current and stator radial force waveform for the 3-phase 6/4, 6/16 and, 12/8 SRMs are shown in Figs. 5.4, 5.5 and 5.6 respectively. In all simulations, the rotation of the rotor is in the CCW direction. The conduction angles θ_{ON} and θ_{OFF} are refered to phase-A. As shown in Figs. 5.4, 5.5 and 5.6 (a), dynamic currents obtained from MEC method show good agreement with FEM. The stator radial force calculated from the MEC method for 6/4 and 12/8 SRMs closely follow the forces calculated from FEM as shown in Figs. 5.4 and 5.6 (b). The stator radial

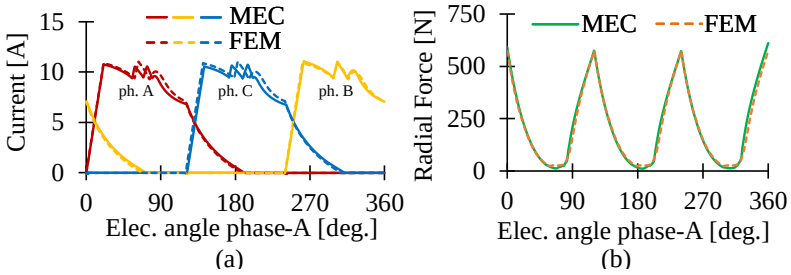

Figure 5.4: Dynamic simulation of 6/4 SRM (a) phase current, (b) stator radial force at $I_{ref} = 10$ A, $\theta_{ON} = 0°$, $\theta_{OFF} = 120°$ at $N_{rpm} = 7500$ rpm.

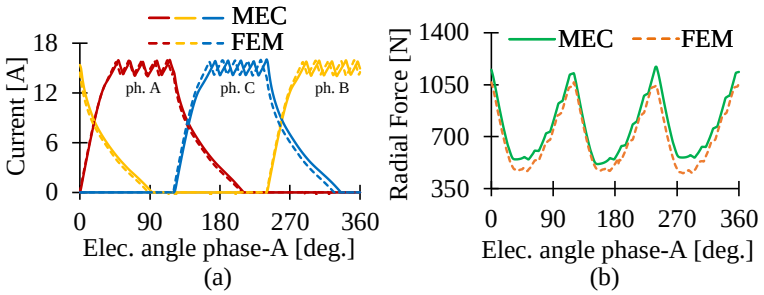

Figure 5.5: Dynamic simulation of 6/16 SRM (a) phase current, (b) stator radial force at $I_{ref} = 15$ A, $\theta_{ON} = 0°$, $\theta_{OFF} = 120°$ at $N_{rpm} = 3000$ rpm.

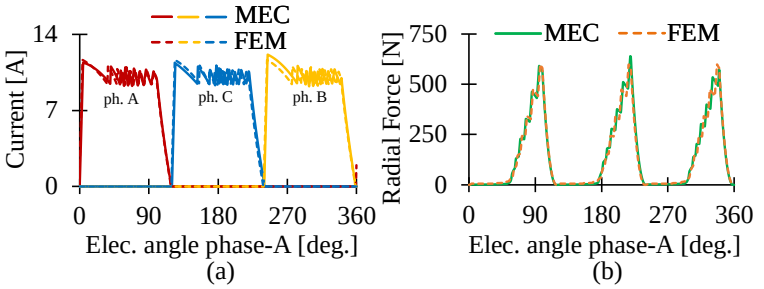

Figure 5.6: Dynamic simulation of 12/8 SRM (a) phase current, (b) stator radial force at $I_{ref} = 10$ A, $\theta_{ON} = 0°$, $\theta_{OFF} = 100°$ at $N_{rpm} = 2500$ rpm.

force calculated for 6/16 SRM from the MEC method in Fig. 5.5 (b) shows small discrepencies compared to the FEM results. Those discrepencies have occured due to minor errors in the calculated airgap flux density in the MEC model.

Figs. 5.7, 5.8, and 5.9 show the dynamic current waveforms and corresponding

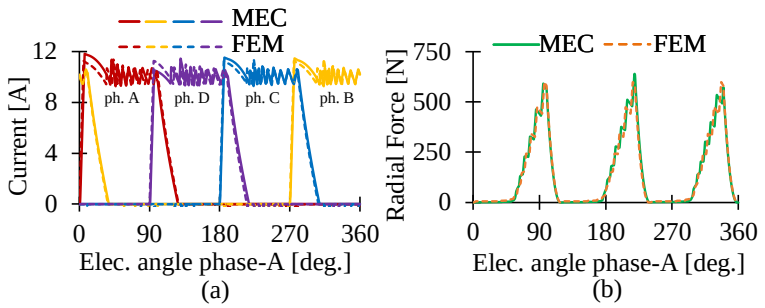

Figure 5.7: Dynamic simulation of 8/6 SRM (a) phase current, (b) stator radial force at $I_{ref} = 10$ A, $\theta_{ON} = 0°$, $\theta_{OFF} = 100°$ at $N_{rpm} = 3500$ rpm.

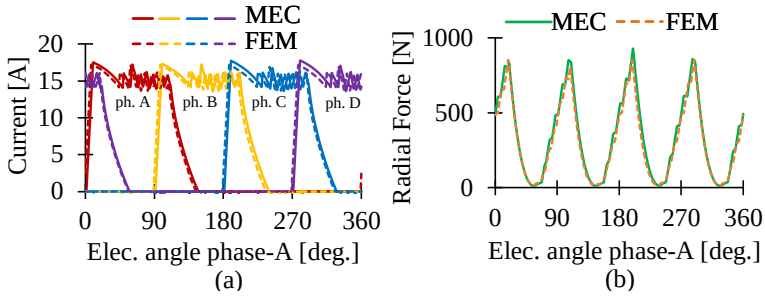

Figure 5.8: Dynamic simulation of 8/10 SRM (a) phase current, (b) stator radial force at $I_{ref} = 15$ A, $\theta_{ON} = 0°$, $\theta_{OFF} = 110°$ at $N_{rpm} = 3000$ rpm.

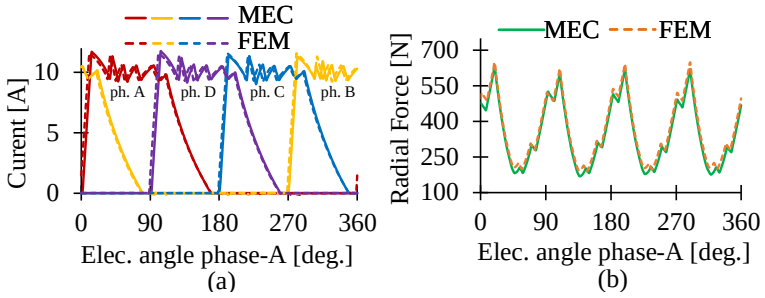

Figure 5.9: Dynamic simulation of 16/12 SRM (a) phase current, (b) stator radial force at $I_{ref} = 10$ A, $\theta_{ON} = 0°$, $\theta_{OFF} = 110°$ at $N_{rpm} = 4000$ rpm.

radial force waveforms for 4-phase 8/6, 8/10 and 16/12 SRMs. Dynamic currents in Figs. 5.7, 5.8, and 5.9 (a) from the MEC method are in good agreement with the FEM results. In Figs. 5.7, 5.8, and 5.9 (b), the stator radial forces calculated from the MEC method match well with the radial forces obtained from FEM.

Table 5.1 compares the errors in RMS current and average radial force from the MEC method with respect to FEM. The MEC method is capable of calculating the RMS current and average radial force with maximum errors 8.73% and 10.19%, respectively.

5.3.2 Radial Force Density Waveform

Figs. 5.10, 5.11, 5.12 (b) and (c) show the radial force density waveforms obtained using the MEC method and FEM for the 3-phase 6/4, 6/16 and 12/8 SRMs. As shown in Figs. 5.10, 5.11 and 5.12 (a), spatial position is varied from 0 to 180° for the 6/4 and 6/16 SRMs and 0 to 90° for the 12/8 SRM. The chosen spatial positions cover three concecutive stator poles belonging the three phases of the SRMs. The rotation of the rotor is considered from 0 to 90°, 0 to 22.5° and 0 to 45° (one electrical cycle) for 6/4, 6/16 and 12/8 SRMs. Therefore, three radial force density pulses exist in Figs. 5.10, 5.11, 5.12 (b) and (c). The radial force density waveforms obtained from the MEC models and FEM models match closely.

Table 5.1: Maximum error in RMS current and average radial force.

Pole configuration	RMS current error	Avg. radial force error
3-phase SRMs		
6/4	5.45 %	3.64 %
6/16	8.43 %	10.19 %
12/8	5.61 %	0.81 %
4-phase SRMs		
8/6	5.57 %	9.18 %
8/10	8.73 %	8.64 %
16/12	5.89 %	5.77 %

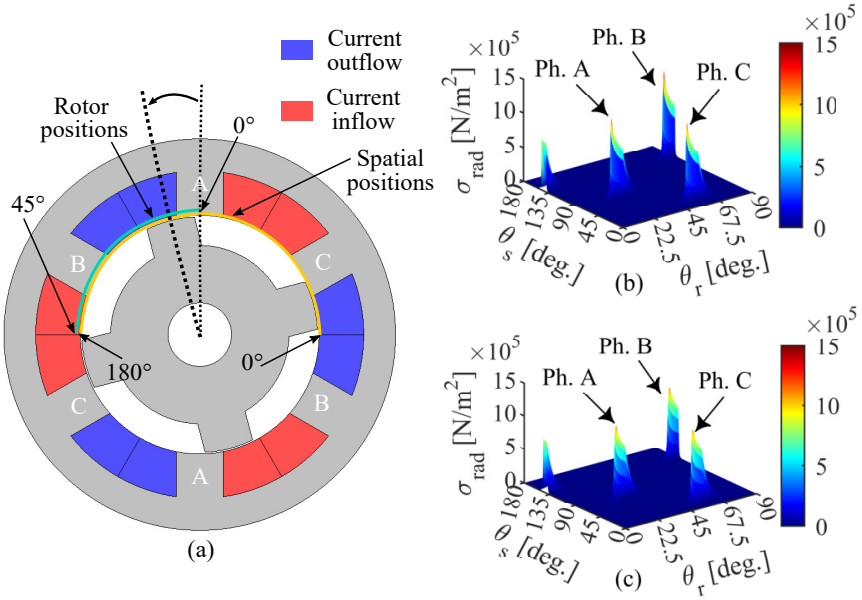

Figure 5.10: Radial force density waveform of 6/4 SRM (a) spatial and rotor positions, (b) MEC and (c) FEM.

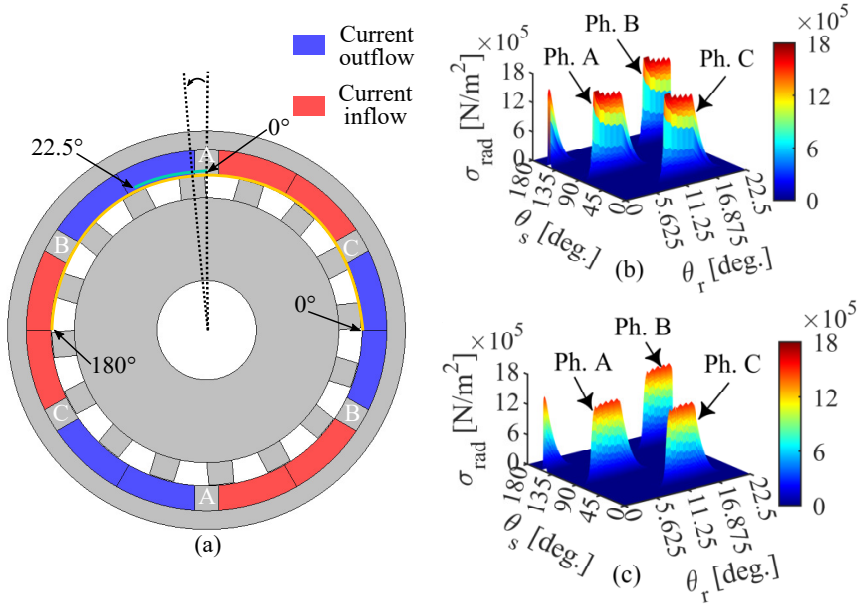

Figure 5.11: Radial force density waveform of 6/16 SRM (a) spatial and rotor positions, (b) MEC and (c) FEM.

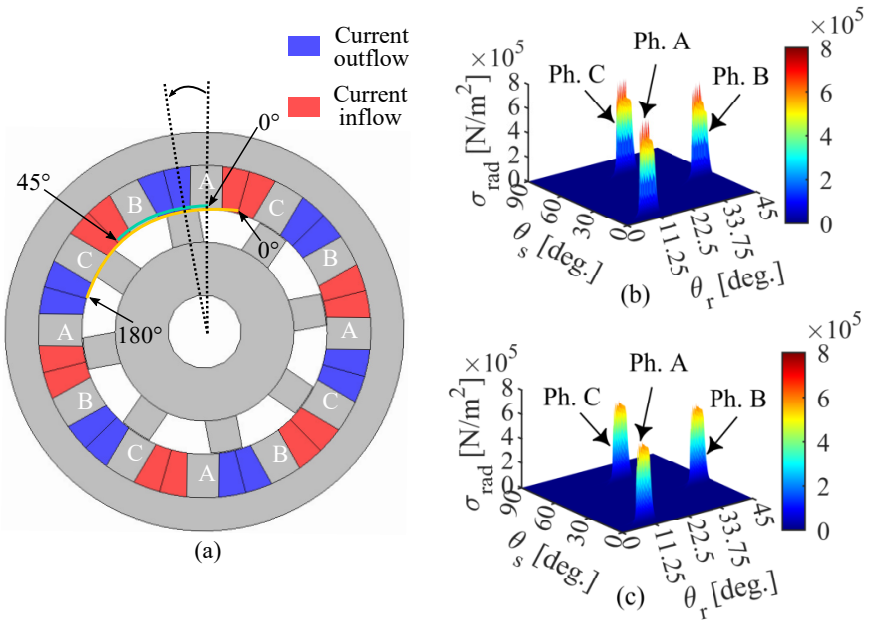

Figure 5.12: Radial force density waveform of 12/8 SRM (a) spatial and rotor positions, (b) MEC and (c) FEM.

Radial force density waveforms obtained for the 4-phase 8/6, 8/10 and 16/12 SRMs using MEC technique and FEM are shown in Figs. 5.13, 5.14, 5.15 (b) and (c). The spatial position changes from 0 to 180° for 8/6 and 8/10 SRMs, and the spatial position of the 16/12 SRM varies from 0 to 90° as shown in Figs. 5.13, 5.14 and 5.15 (a). These spatial positions cover four concecutive stator poles and each of those poles belong to the four phases as illustrated in Figs. 5.13, 5.14 and 5.15 (a). Rotor rotates from 0 to 60°, 0 to 36° and 0 to 30° (one electrical cycle) for 8/6, 8/10 and 16/12 SRMs, respectively. Thus, there are four radial force density pulses in Figs. 5.13, 5.14, 5.15 (b) and (c). In Figs. 5.13, 5.14 and 5.15 (b), the radial force density waveforms obtained from MEC model closely follow the radial force density waveforms obtained from the FEM models. The distribution of the force density from MEC model is not as smooth as those obtained from FEM model because of the

coarse airgap mesh used in the MEC models.

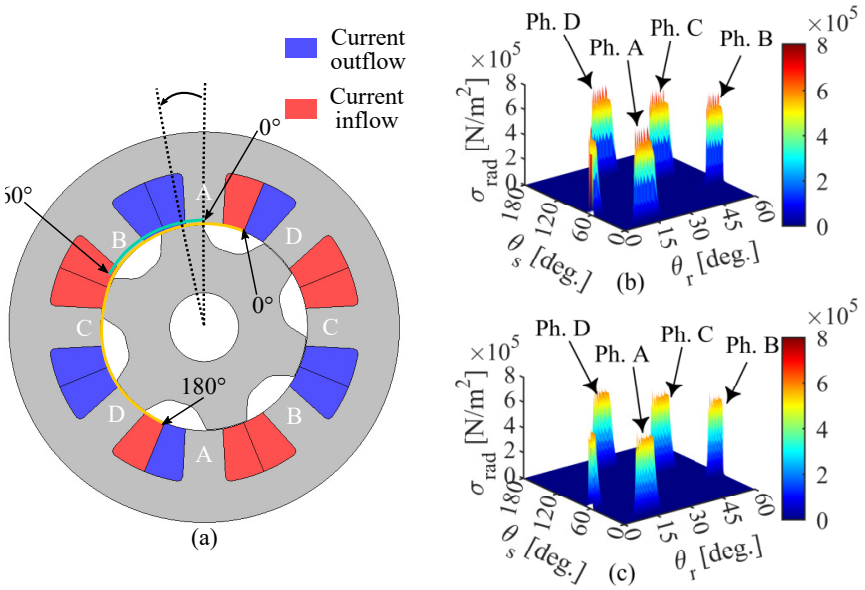

Figure 5.13: Radial force density waveform of 8/6 SRM (a) spatial and rotor positions, (b) MEC and (c) FEM.

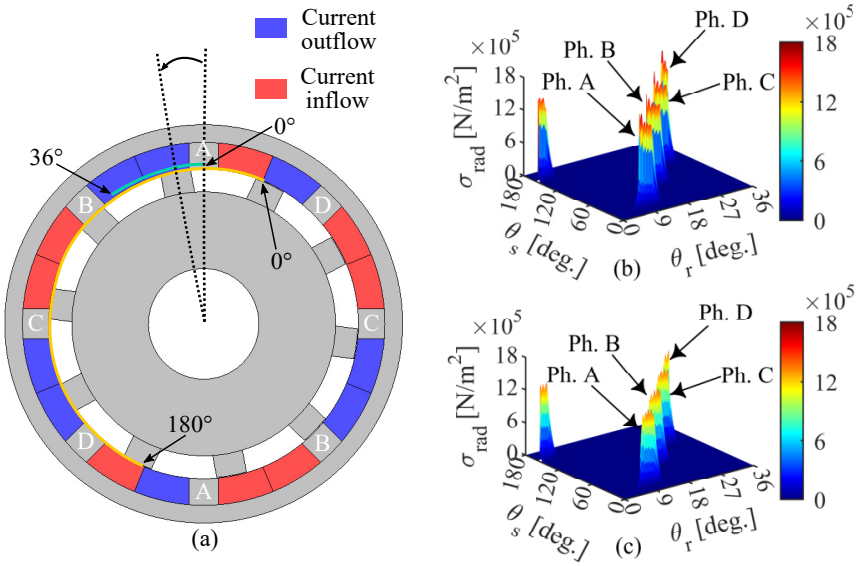

Figure 5.14: Radial force density waveform of 8/10 SRM (a) spatial and rotor positions, (b) MEC and (c) FEM.

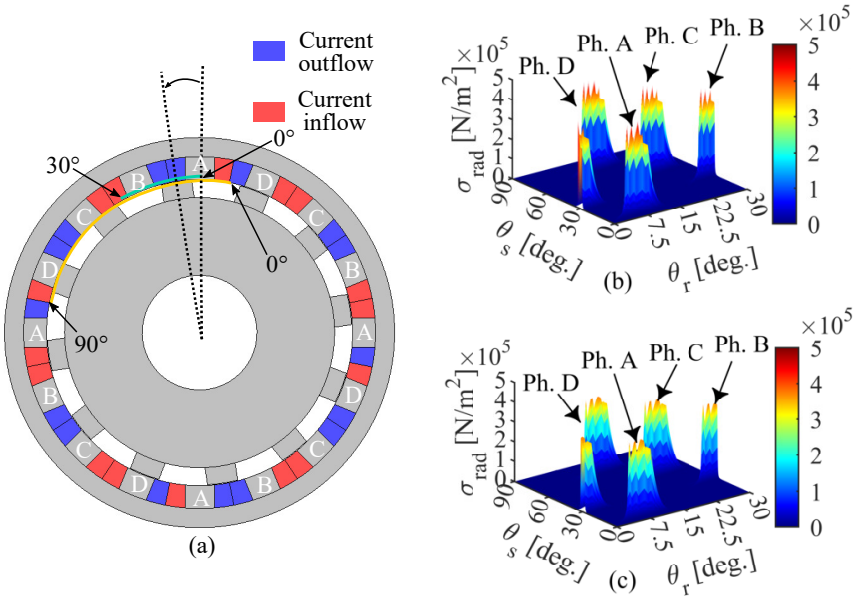

Figure 5.15: Radial force density waveform of 16/12 SRM (a) spatial and rotor positions, (b) MEC and (c) FEM.

5.3.3 Decomposition of the Radial Force Density Waveform

Figs. 5.16, 5.17, 5.18 (a) and (b) shows the dominant harmonic components of the radial force density waveforms in Figs. 5.10, 5.11, 5.12 (b) and (c). The spatial orders of the harmonic specturms in Figs. 5.16, 5.17 (a) and (b) are mutiples of two since 6/4 and 6/16 SRMs have two magnetic poles. The 12/8 SRM has four magnetic poles; hence, the spatial orders are multiples of four in Fig. 5.12 (a) and (b). The temporal orders at the breathing mode ($v = 0$) are symmetrically spaced with multiples of the number of strokes, S_{tr} on the temporal order axis. The 6/4, 6/16 and 12/8 SRMs have number of strokes 12, 48 and 24. Therefore, temporal orders at $v = 0$ are multiples of 12, 48 and 24 as shown in Figs. 5.16, 5.17, 5.18 (a) and (b). The first temporal order corresponding to the fundamental or the first non-zero spatial order is equal to the number of rotor poles N_r and located in the 1st or 2nd quadrant based on the

phase excitation sequence. The fundamental spatial order of the 6/4 and 6/16 SRMs is 2, and the fundamental spatial order of the 12/8 SRM is 4. As shown in Figs. 5.4, 5.5, and 5.6 (a) and in Figs. 5.10, 5.11, and 5.12 (a), phases of those three SRMs are excited in the CW direction (A-C-B sequence). Therefore, first temporal order corresponding to the fundamental spatial order of 6/4, 6/16 and 12/8 SRMs are 6, 16 and 8 and, located in the 1st quandrant of the harmonic spectrums in Figs. 5.16, 5.17, 5.18 (a) and (b). The percentage errors of the harmonic specturms obtained from MEC method are calculated with respect to the harmonic specturms from the FEM. The calculated percentage errors for 6/4, 6/16 and 12/8 SRMs are shown in Figs. 5.16, 5.17 and 5.18 (b) in the first and fourth quardrants.

The dominant harmonic components of the radial force density waveforms in Figs. 5.13, 5.14, 5.15 (b) and (c) for 8/6, 8/10 and 16/12 SRMs are shown in Figs. 5.19, 5.20, 5.21 (a) and (b). Since 8/6 and 8/10 SRMs have two magnetic poles, spatial orders of the harmonic specturms in Figs. 5.19, 5.21 (a) and (b) are mutiples of two. The spatial orders in Figs. 5.21 (a) and (b) of the 16/12 SRM are multiples of four, because it has four magnetic poles. The number of strokes of the 8/6, 8/10

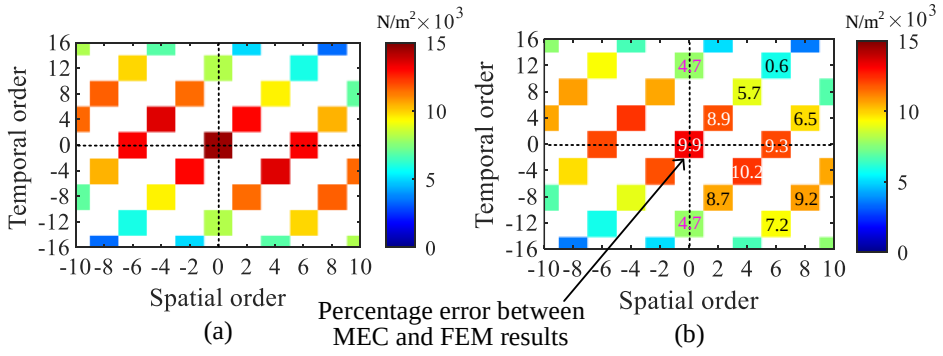

Figure 5.16: Decomposition of radial force density waveform for 6/4 SRM (a) MEC and (b) FEM.

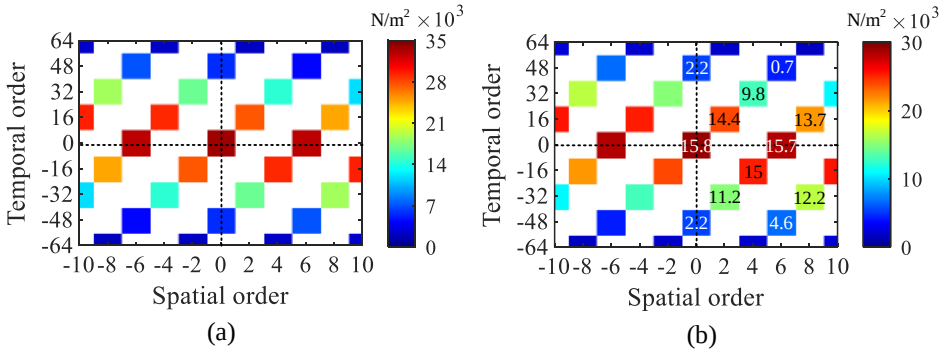

Figure 5.17: Decomposition of radial force density waveform for 6/16 SRM (a) MEC and (b) FEM.

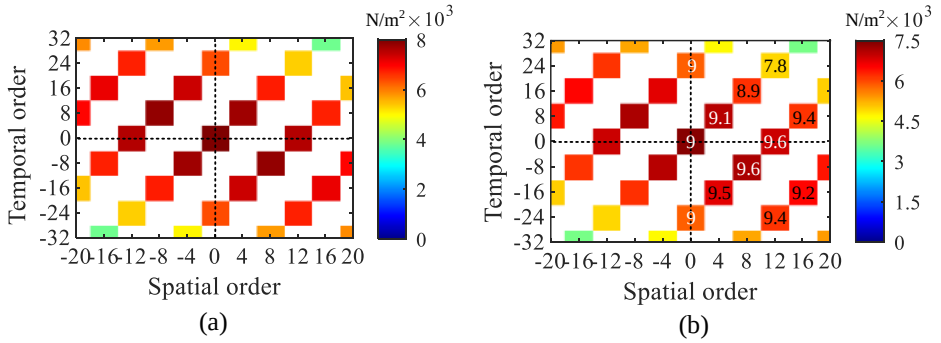

Figure 5.18: Decomposition of radial force density waveform for 12/8 SRM (a) MEC and (b) FEM.

and 16/12 SRMs are 24, 40 and 48. Therefore, temporal orders at the spatial order zero are multiples of 24, 40 and 48 as observed in Figs. 5.19, 5.20, 5.21 (a) and (b). The fundamental spatial order of the 2-pole 8/6 and 8/10 SRMs is 2, and the fundamental spatial order of the 4-pole 16/12 SRM is 4. As shown in Figs. 5.7, 5.9 (a) and Figs. 5.13, 5.15 (a), phases of 8/6 and 16/12 SRM are excited in the CW direction (A-D-C-B sequence). Therefore, first temporal order corresponding to the fundamental spatial order of 8/6 and 16/12 SRMs are 6 and 12, and those harmonics are located in the 1st quandrant of the harmonic spectrums in Figs. 5.19, 5.21 (a) and (b). The phase excitation sequence of the 8/10 SRM is in CCW direction (A-B-C-D

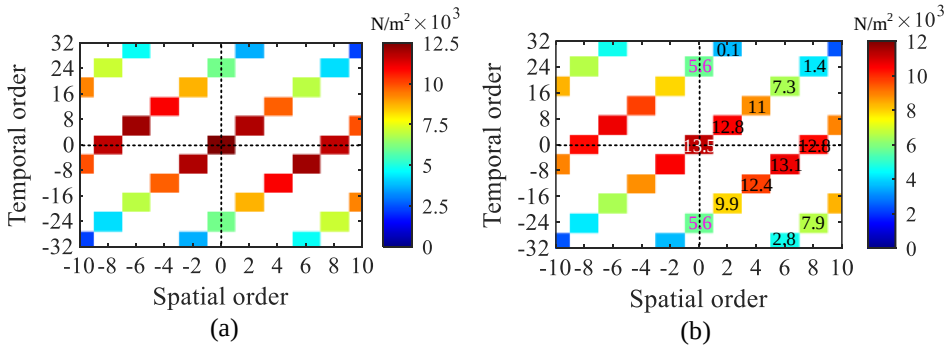

Figure 5.19: Decomposition of radial force density waveform for 8/6 SRM (a) MEC and (b) FEM.

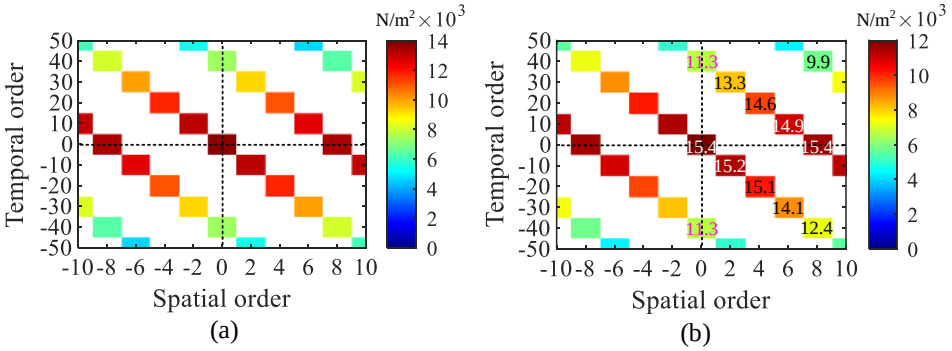

Figure 5.20: Decomposition of radial force density waveform for 8/10 SRM (a) MEC and (b) FEM.

sequence) as shown in Figs. 5.8 (a) and 5.14 (a). Thus, the first temporal order corresponding to the fundamental spatial order of 8/10 SRM is 10, and it is located in the 2nd quadrant of the harmonic specturm as shown in Fig. 5.20 (a) and (b). Percentage errors of the harmonic specturms obtained from the MEC models of 8/6, 8/10 and 16/12 SRMs are shown in Figs. 5.19, 5.20 and 5.21 (b) in the first and fourth quadrants.

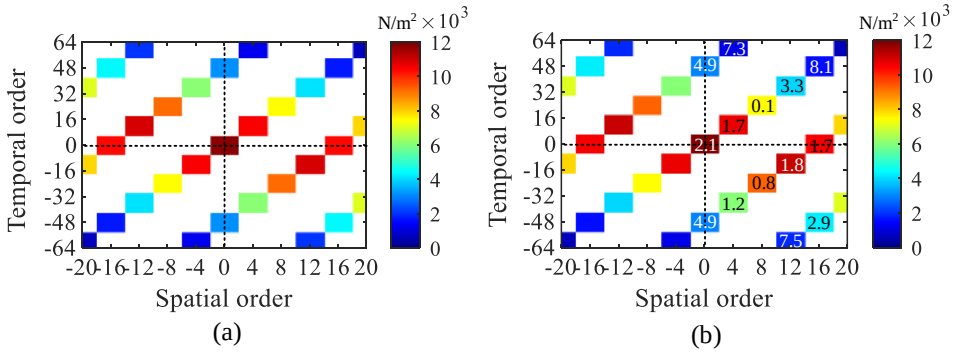

Figure 5.21: Decomposition of radial force density waveform for 16/12 SRM (a) MEC and (b) FEM.

5.4 Summary

A radial force density calculation method using the reluctance mesh-based MEC method for an SRM was proposed in this chapter. The radial force density for 3-phase 6/4, 6/16, 12/8 and, 4-phase 8/6, 8/10, and 16/12 SRMs was calculated by utilizing the Maxwell Stress Tensor method and the dynamic models developed using the MEC models. The harmonics of the radial force density were calculated using the 2D FFT. The results obtained from the MEC model were validated using the FEM.

Chapter 6

Sizing of Motor Geometry for an Electric Aircraft Propulsion SRM using Reluctance Mesh-Based MEC Technique

6.1 Introduction

Electrified propulsion is expected to dominate future transportation systems due to the environmental impact of burning fossil fuels. Electric motors are on the path to replace the engines energized by fossil fuels. PMSMs are already in use in electric propulsion systems [139]. The main drawbacks of PMSMs are the sensitivity of PMs to temperature and demagnetization, and the price volatility and supply chain issues with rare earth metals that make up PMs [6,139]. SRM can overcome these drawbacks

due to its magnet-free motor geometry [1]. SRMs also have other advantages such as low cost, simple construction, and capability to operate at higher speeds [1, 6].

Designing an SRM for an electric propulsion system consists of multiple stages. Various electromagnetic models are used iteratively in each design stage [140]. Usually, FEM is utilized in an SRM design. As an alternative, MEC models can be applied in an SRM design [141]. One of the essential tasks in an SRM design process is to determine the motor geometry. In [142] and [143], MEC models are applied to design a wound field synchronous machine (WFSM) and a PMSM for electric vehicle applications. MEC method is applied in [112] and [144] to design a flux switching machine for an in-wheel motor. The motor geometry of an axial flux SRM is obtained in [11] and [109] utilizing MEC models. But, the conventional MEC method implemented in [112] and [11, 109, 142–144] requires prior knowledge of the flux path inside the motor. It can be challenging to predefine the flux path accurately in an SRM due to its salient structure, while modifying the motor geometry. The reluctance mesh-based MEC method is an alternative that does not require prior knowledge of the flux paths inside an SRM.

In this chapter, the proposed reluctance mesh-based MEC method in this thesis is applied to design a 3-phase 12/16 SRM for the performance requirements of the NASA HLM for the Maxwell X-57 aircraft [3]. The design specifications of the HLM and the motor geometry of the proposed 12/16 SRM are presented in this chapter. Finally, the MEC-based static and dynamic characteristics of the proposed SRM and compares them with the results from FEM.

6.2 NASA Maxwell-57 Electric Aircraft

This chapter applies a reluctance mesh-based MEC technique to the design process of a 3-phase 12/16 SRM for a high lift motor in NASA Maxwell X-57 electric aircraft. In this section, first the NASA Maxwell X-57 aircraft is presented, and then, the design specifications for the NASA high lift motor for the Maxwell X-57 aircraft are introduced.

6.2.1 NASA Maxwell X-57 Aircraft

The NASA Maxwell X-57 aircraft consist of a distributed electrical propulsion system. The main objectives for the Maxwell X-57 are to reduce the energy consumption during the cruise, achieve zero carbon emmision, and decrease the noise. The total propulsion power of the aircraft is provided by 14 electric motors as shown in Fig. 6.1 [3]. The two large motors at the corners of the left and right wings mainly produce the power for cruising. The remaining 12 motors are the high lift motors (HLMs). HLMs are mounted on the left and right wings, and they operate during the flight take-off and landing. The HLMs are not operated during the cruise to reduce air drag. These 12 HLMs should ensure climbing of the aircraft up to a maximum altitude of 3 km above sea level. The expected minimum operation time of the HLMs during the climbing stage is approximately 250 seconds. Also, there is a run-up for 30 seconds at the beginning of the flight mission where the motors run at 4000 rpm.

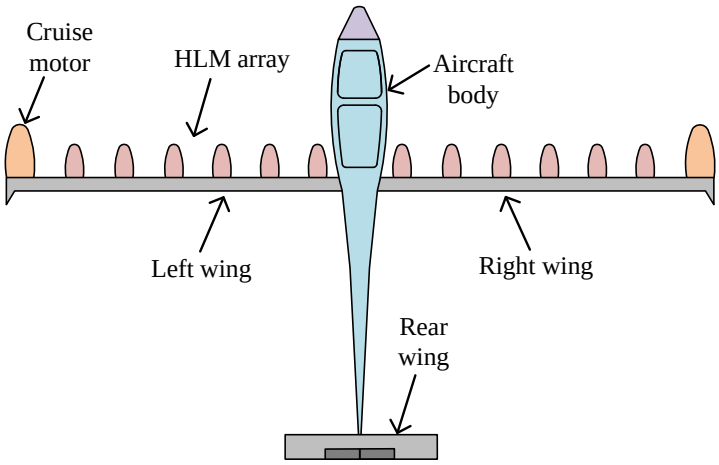

Figure 6.1: Top view of the NASA Maxwell X-57 distributed propulsion aircraft [3].

6.2.2 Design Specifications of the HLM

For the given operating scenarios, the electrical and physical requirements for HLM defined by NASA are shown in Table 6.1 [3,145]. NASA has already designed a PMSM to achieve the above requirements. The outer diameter of the PMSM was 156.45 mm. The maximum available axial length for the stator (including the stack length of the stator core and the length of the end turns) was defined as 66.4 mm. The stator design of the PMSM achieves a stack length of 34.5 mm by using a 24 slot-20 pole PMSM design. The torque density of the PMSM has been greatly improved by using a Halbach magnet array. This also helped reducing the rotor back-iron thickness of the PMSM to 2.45 mm, leading to further weight reduction. The maximum magnet temperature was considered to be $120°C$. The stator and rotor laminations are bonded using EB-548 epoxy. The maximum allowable temperature of the EB-548 is $140°C$. Based on these temperature constraints, the maximum current density of the PMSM is limited to 11 A/mm^2. The maximum wire fill factor and current density requirements, and the achieved fill factor and current density for the PMSM design are shown in

Table 6.2.

6.3 Proposed SRM Design

In this section, the design process of the SRM is discussed. The techniques of selecting the pole configuration, geometry parameters, winding configuration, and the magnetic

Table 6.1: Main design specifications of an high lift motor (HLM).

Electromagnetic design parameters	
Peak output power	13.7 kW
Peak torque	24 Nm
Base speed	5450 rpm
RMS phase current	35 A
DC link voltage	385-538 V
Number of phases	3
Geometry constraints	
Maximum motor diameter (with casing)	161.5 mm
Maximum stator outer diameter (without casing)	156.45 mm
Maximum stator axial length including end turns	66.4 mm
Expected performance	
1. Provide 24 Nm of torque between 2000-5450 rpm and 22 Nm of torque at 5460 rpm. 2. Capable of producing 10.5 kW output power at 5460 rpm and at 460 V DC link voltage with a minimum efficiency of 93%.	

Table 6.2: Fill factor and current density constraints.

Characteristic	Maximum allowable value	Achieved by PMSM design
Wire fill factor	60%	58.4%
Current density	11 A/mm^2	10.7 A/mm^2

material are explained.

6.3.1 Selection of the Pole Configuration

According to the dimensional constraints given by NASA, HLM requires a higher torque to volume ratio. Therefore, flux density in the stator core should be closer to the saturation flux density of the utilized steel material to increase the torque density. In this application, the maximum wire fill factor in the stator slots is constrained to 60%. The motor should have only three phases, according to NASA specifications. Considering the geometry and fill factor constraints, choosing a high stator pole count might limit the slot area. That could further reduce the MMF leading to lower torque production. The stator outer diameter is constrained to 156.45 mm as listed in Table 6.1. The number of stator poles higher than 12 might result in a small stator pole width, leading to oversaturation of the stator teeth. Therefore, the pole configurations that have more than 12 stator poles were not considered for this application. Hence, the possible numbers of stator poles are 6 and 12. The pole configurations with six stator poles have only two magnetic poles for three phase operation. This means that there would be two flux loops in the stator back-iron. Since HLM SRM is designed for high torque density, a relatively small back iron thickness is used. This was the case also for the PMSM design. If a two-pole SRM configuration was used, the stator back-iron could reach to saturation quickly, affecting the torque production capability of the machine. Considering these reasons, the number of stator poles is selected as 12.

There are various number of rotor pole options that would provide a balanced 3-phase operation with 12 stator poles. Considering the speed and torque requirements

of the HLM, three options for the number of rotor poles are considered for 12 stator poles: 8, 16 and 20. For 8 rotor poles, the number of torque pulsations is 24, for 16 it is 48, and for 20 it is 60. For the given speed range and the stator outer diameter, 16 rotor poles is a better choice to maintain an effective stator pole width considering torque density, and a reasonable electrical frequency considering core losses for the given speed range.

6.3.2 Selection of Geometry Parameters

The geometry design parameters of the 3-phase 12/16 SRM are shown in Fig. 6.2. The motor geometry is determined to achieve the maximum torque requirement at the minimum DC link voltage of 385 V. According to the given specifications in Table 6.1, the maximum outer diameter of the motor with the casing should be 161.5 mm. The stator outer diameter is set at 156.45 mm, which is the same as the PMSM designed by NASA for the HLM application.

The airgap length is selected as 0.35 mm to achieve high torque density. An airgap length of 0.35 mm would require tighter tolerances when manufacturing the cores and other mechanical parts of the motor. For an industrial application, this would potentially reflect as a higher cost. However, for an aircraft application, cost is usually a lower priority than torque density.

The maximum and the minimum limits of the pole arc angles are calculated according to

$$\beta_r + \beta_s \leq \frac{360^\circ}{N_r} = 22.5^\circ \tag{6.3.1}$$

$$\beta_r + \beta_s \geq \frac{720^\circ}{mN_r} = 15^\circ. \tag{6.3.2}$$

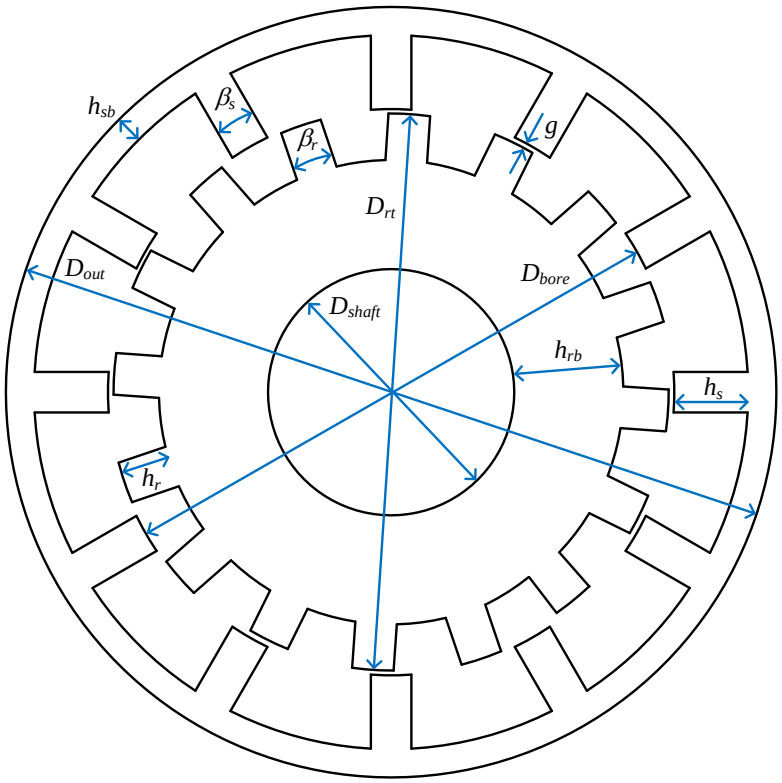

Figure 6.2: Main geometry parameters of the 12/16 SRM.

Equation (6.3.1) ensures existence of fully unaligned position. Equation (6.3.2) is the minimum condition of pole arc angles for self-starting condition in SRMs. Initially, both β_r and β_s were chosen as 7.5° to satisfy (6.3.2). Then, pole arc angles were iteratively modified to achieve the performance requirements of the motor. The final values of the stator and rotor pole arc angles were 8.2° and 8.5°, respectively.

The stator pole height is selected to maximize the slot area while achieving the torque requirements within the given fill factor constraint. For the rotor pole height, after various design iterations using the MEC model, it was found out that the rotor pole height below 8 mm can cause the flux to penetrate into the back-iron instead of the rotor pole. This reduces the torque production. The final rotor pole height was

selected as 10 mm, as there was no significant improvement in the torque when the rotor pole height is above this value.

The stator back iron of the PMSM designed for the HLM application was approximately 3 mm due to the high torque-density requirement. The stator back-iron thickness should be sufficiently large to provide the mechanical strength of the stator and avoid oversaturation. In the SRM design, the stator back-iron thickness is always kept higher than 5 mm to provide a better structural support to the stator poles and to avoid oversaturation of the back iron. The rotor back-iron thickness is determined according to the rotor pole height, and the shaft diameter [6,7]. The shaft diameter of the 12/16 SRM design is 50 mm. The final values for the motor geometry parameters for the 12/16 SRM design for the HLM application are given in Table 6.3.

Table 6.3: Proposed dimensions of the SRM geometry.

Parameter	Value
Outer diameter (D_{out})	156.45 mm
Bore diameter (D_{bore})	115 mm
Shaft diameter (D_{shaft})	50 mm
Airgap length (g)	0.35 mm
Stator pole arc angle (β_s)	8.2°
Rotor pole arc angle (β_r)	8.5°
Stator pole height (h_s)	15 mm
Rotor pole height (h_r)	10 mm
Stator back-iron thickness (h_{sb})	5.725 mm
Rotor back-iron thickness (h_{rb})	22.15 mm

6.3.3 Material for the Magnetic Cores

For the 12/16 SRM design, it is essential to achieve higher flux density in the airgap to maximize the torque density [3]. The utilized magnetic steel material should have a higher saturation flux density. Cobalt-iron (CoFe) magnetic materials provide the highest saturation flux density level as compared to the other technologies in the market [139]. Hiperco-50A iron-cobalt vanadiaum soft magnetic allow from Carpenter Technology is chosen as the magnetic core lamination material for both stator and rotor. The B-H curve of the 0.35 mm thickness lamination is used for the sizing of the 12/16 SRM.

6.3.4 Selection of Winding Configuration and Stack Length

There are four coils per phase in a 3-phase 12/16 SRM. For this application, all four coils are connected in series. The number of turns should be sufficient to create the required MMF in the airgap. The maximum number of turns of a coil is limited by the maximum slot fill factor, wire size, DC link voltage constraint, current dynamics, and phase resistance or copper loss [7]. The HLM design requires to deliver 24 Nm of torque at 5450 rpm. From SRM design perspective, this would require minimum 24 Nm peak static torque around 50A excitation current to satisfy the RMS current constraint. Also, the peak static induced voltage needs to be within 385-538V at 5450 rpm. As show in Table 6.1, the maximum available stator axial length including the end turn lengths is constrained at 66.4 mm. After analyzing the static torque characteristics of the SRM design with different number of turns per coil and stator core stack length in various iterations, and checking the dynamic performance of the motor with the MEC model, the number of turns per coil is selected as 32 and the

stator core stack length is selected as 47 mm. The end turn length on each side of the coil is estimated as 9.7 mm. This makes the total axial length of the stator 66.4 mm, which is within the design constraint defined in Table 6.1. Different wire gauges with different numbers of strands are considered to achieve the wire fill factor constraint of 60% and the current density limit of 11 A/mm^2. With 32 turns and three strands per coil wound with 17 AWG heavy-build magnet wire, the 12/16 SRM design achieves 24 Nm at 5450 rpm with an RMS current of 34.3 A at the minimum DC link voltage of 385 V. The SRM achieves this requirement at an RMS current density of 10.96 A/mm^2 with a fill factor of 58.4 %, which are lower than the design constraints defined in Table 6.2. The final design parameters of the selected winding configuration and stack length are provided in Table 6.4.

The stack length of the SRM design is longer than the stack length of the PMSM. However, the PMSM design uses a Halbach magnet array design to improve the torque density and the maximum magnet temperature was considered as 120°C. In

Table 6.4: Proposed winding configuration and axial length constrains.

Parameter	Value
Number of turns per coil (N_t)	32
Number of strands	3
Wire fill factor	58.4 %
Maximum current density	10.96 A/mm^2
Wire guage	17 AWG Heavy-build
Coil resistance (R_{coil})	0.02768 Ω
Stator core Stack length (L_{stk})	47 mm
Estimated stacking factor	97 %
Estimated end turn length (L_{end})	9.7 mm
Total axial length (L_{ax})	66.4 mm

the 12/16 SRM, there are no permanent magnets. Hence, the SRM can operate at a higher temperature. Among the active materials of an SRM, the polymer insulation of the magnet wires are usually more sensitive to temperature. However, the polymer insulation of magnet wires can handle a much higher temperature than the magnets. For example, $200°C$ thermal class magnet wire is widely accessible. Magnet wires with insulation rated for $240°C$ are also available. Another temperature-limiting material in the PMSM design was the epoxy used for bonding the cores. In the PMSM design, the stator and rotor cores were made of cobalt-iron magnetic material. The laminations were bonded using EB-548 epoxy, which has a maximum allowable temperature of $140°C$. The 12/16 SRM is also designed for cobalt-iron magnetic material and it might require a similar core stacking technique using a bonding agent. Therefore, it is reasonable to limit the operating temperature of the 12/16 SRM at $140°C$, which is higher than the temperature limited by the permanent magnets in the PMSM design. A higher operating temperature for the SRM can be targeted if a different stacking technique is employed, such as welding or interlocking. The choice of stack retention method is dependent on various factors, including manufacturability and change in core loss due to manufacturing stresses.

The higher temperature limit for the SRM can enable targeting a higher current density. Based on further analysis using the MEC model, the calculated stack length of 47 mm at 10.96 A/mm^2 can be further reduced to 45 mm for a current density of 11.82 A/mm^2. In that case, the motor is able to provide 24 Nm at 5450 rpm with an RMS current of 34.8 A at 385 V DC link voltage. The SRM achieves this requirement with 33 turns and 9 strands per coil wound with 22 AWG heavy-build magnet wire. This corresponds to a fill factor of 59.26 % and an estimated phase

resistance of 0.02943 Ω. It should be noted that the higher current density operation of the motor should be validated with thermal analysis.

6.4 Static Characteristics of the Proposed SRM

In this section, the static characteristics, such as the static flux linkage, magnetic flux density, static electromagnetic torque, and static induced voltage obtained from the MEC model of the proposed 12/16 SRM are presented. The results are validated by using the FEM model of the proposed motor geometry in JMAG software.

6.4.1 Magnetic flux density

After obtaining the field solution, the branch fluxes in all mesh elements in the MEC model can be calculated from (4.2.18). The magnitude of the flux density is then calculated from (4.3.3) and (4.3.4). The airgap flux density components from the static analysis are shown in Fig. 6.3. Flux densities are calculated for one stator pole pitch at the aligned and unaligned positions with 60 A excitation current. The radial and tangential airgap flux densities from the MEC model match well with FEM results. The radial flux density at the unaligned position and tangential flux density at the aligned position show minor differences near the spatial angles 10° and 20°. This is because of the field calculation error near the stator and rotor pole edges due to the complex elements.

The magnitude of the flux density distribution inside the SRM at the aligned and unaligned positions are shown in Fig. 6.4. The flux density distribution obtained

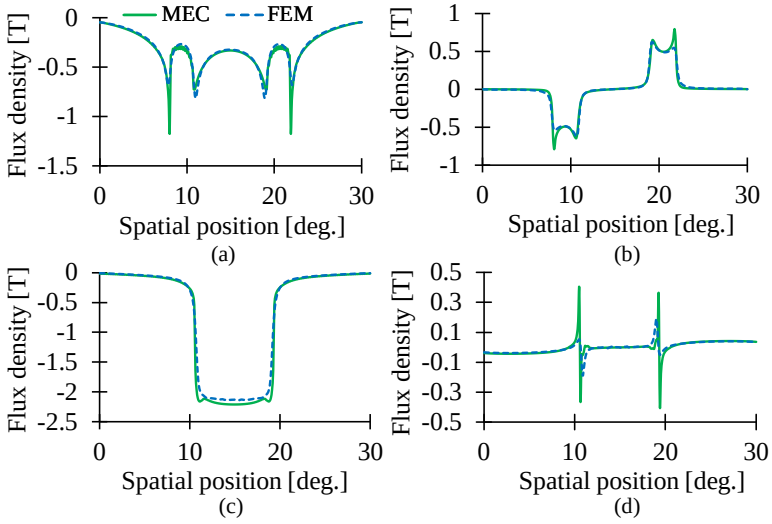

Figure 6.3: Airgap flux density waveforms at 60 A static excitation current: (a) radial flux density at the unaligned position (b) tangential flux density at the unaligned position, (c) radial flux density at the aligned position, and (d) tangential flux density at the aligned position.

from the MEC method shows fair agreement with the flux density distribution obtained from FEM. The flux density values at points P_1, P_2 and P_3 in Fig. 6.4 and their percentage errors relative to the FEM are shown in Table 6.5. The maximum percentage error that occurred in the flux density calculation is less than 10%.

Table 6.5: Flux density comparison at points P_1, P_2 and P_3 in Fig. 6.4 in static simulations.

Position	Point P_1			Point P_2			Point P_3		
	MEC	FEM	% error	MEC	FEM	% error	MEC	FEM	% error
Unaligned	0.98 T	0.96 T	2.1 %	1.43 T	1.31 T	9.1 %	0.55 T	0.54 T	1.9 %
Aligned	1.89 T	1.8 T	5 %	2.41 T	2.33 T	3.4 %	2.31 T	2.25 T	2.7 %

6.4.2 Static flux linkage, torque and voltage

The phase flux linkage can be calculated from (4.3.5). Hence, the induced phase voltage can be determined from (2.2.1). Maxwell Stress Tensor method is applied to compute the tangential force density in the airgap. The electromagnetic torque is then calculated by integrating the tangential force density over the airgap surface area defined by the radial distance in the airgap from (4.3.8) as shown in Fig. 4.6.

The static phase flux linkage of the proposed SRM at different currents is shown in Fig. 6.5. The flux linkage characteristics from the MEC method show a good match with the FEM results. The static induced voltage characteristics are shown in Fig. 6.6. Induced voltage from the MEC model follows the voltage calculated from the

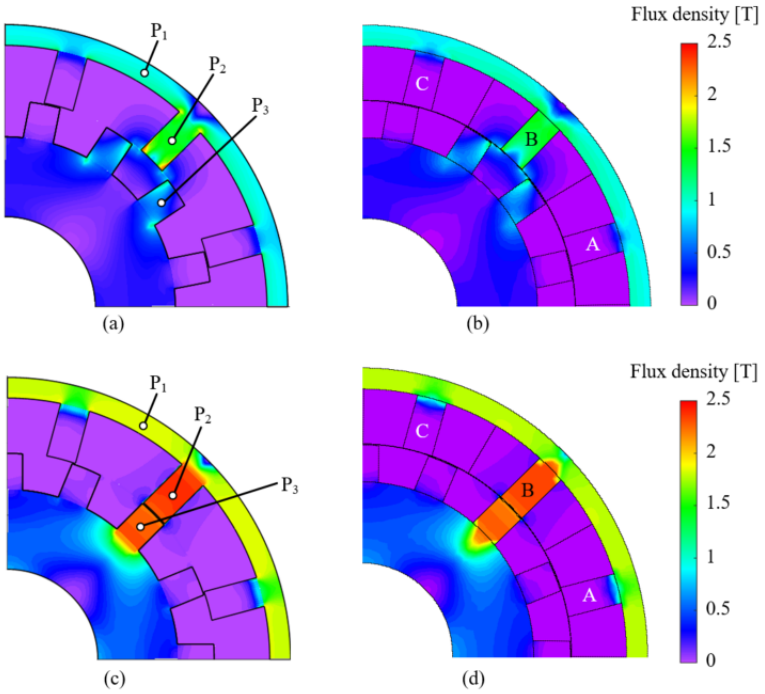

Figure 6.4: Magnetic flux density contours at 60 A static excitation current: (a) unaligned position, MEC, (b) unaligned position, FEM, (c) aligned position, MEC, (d) aligned position, FEM.

FEM model. The voltage profile is calculated by taking the time derivative of the flux linkage characteristics from the MEC model. It can be observed from Fig. 6.5 that the change in the slope in the flux linkage characteristics between 30°-60° electrical angles in the MEC model is not as smooth as the results from the FEM model. This is due to the coarse mesh density used in the MEC model. Therefore, voltage profiles from the MEC model do not match perfectly to the results from FEM within that interval. However, at the other electrical positions, the static voltage profiles from the MEC model fairly match with the FEM results. It will be shown in the next section that this small difference in the static flux linkage and voltage characteristics does not cause a significant impact on the dynamic characteristics calculated from the MEC model. The static electromagnetic torque characteristics of the 12/16 SRM is shown in Fig. 6.7. There is a good match between the torque calculated from the MEC and FEM models. Only minor differences can be recognized in the torque profiles between the electrical angles 30°-60°.

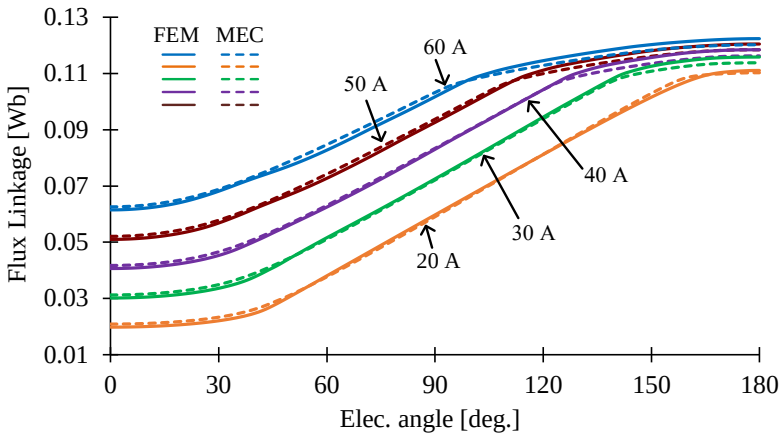

Figure 6.5: Static phase flux linkage characteristics at different currents.

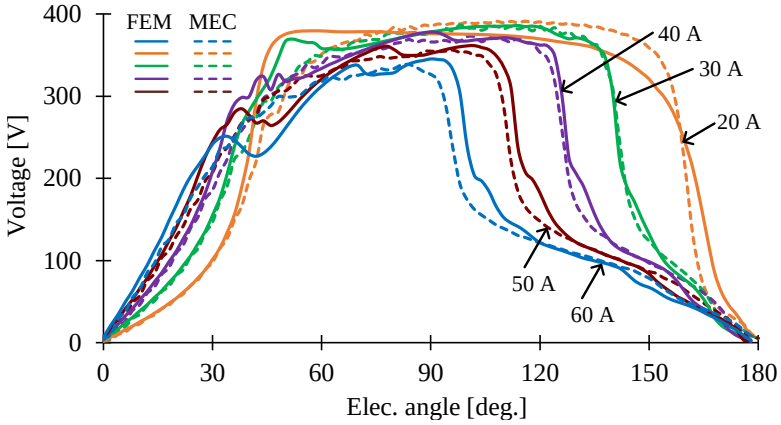

Figure 6.6: Static phase voltage characteristics at 5450 rpm at different currents.

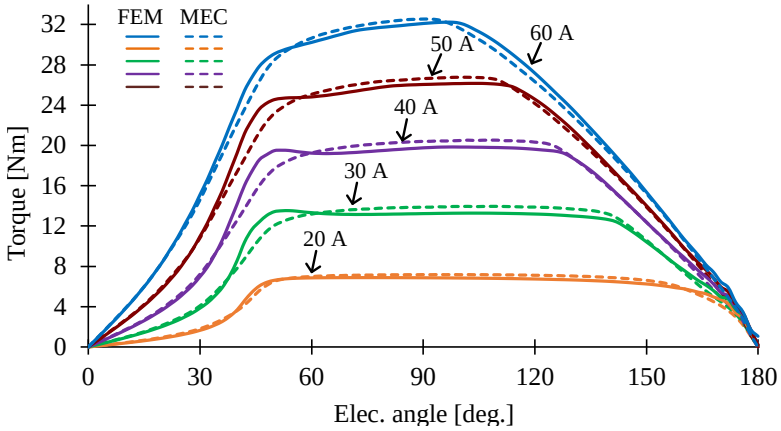

Figure 6.7: Static torque characteristics at different currents.

6.5 Dynamic Characteristics of the Proposed SRM

The dynamic phase currents, and the corresponding flux density and electromagnetic torque from the MEC model of the proposed SRM design are presented in this section. The FEM model is developed in JMAG using the motor geometry obtained from the MEC-based design to validate the dynamic characteristics. The torque-speed characteristics and power-speed characteristics obtained using the MEC model are also presented and compared with FEM results.

6.5.1 Dynamic Current and Electromagnetic Torque

In the dynamic simulations, the conduction angles θ_{ON} and θ_{OFF} are referred to the electrical angle of phase-A. Zero electrical angle indicates that phase-A is at the unaligned position. The dynamic current and corresponding electromagnetic torque at 2000 rpm and 4000 rpm are shown in Figs. 6.8 and 6.9. The RMS current is regulated below 35 A. Here the conduction angles θ_{ON} and θ_{OFF} are heuristically adjusted to provide approximately 24 Nm of torque using the MEC model. The conduction angles are then applied to the FEM model that is excited with an asymmetric bridge converter model with a DC link voltage source of 385 V. According to Figs. 6.8 and 6.9, the dynamic phase current and electromagnetic torque determined from the MEC model are in good agreement with the FEM model. The calculated dynamic current and generated electromagnetic torque at 5450 rpm and 5460 rpm are shown in Figs. 6.10 and 6.11. In both speeds, RMS current is 34 A as shown in Figs. 6.10 and 6.11 (a). The results from the MEC and FEM models show a good match. In some regions of the torque profiles in Figs. 6.10 and 6.11 (b), MEC model calculates slightly higher torque since the calculated dynamic current is higher in those regions. Also, in some regions, MEC model calculates lower current compared to the FEM model. Hence, the generated torque in those regions is slightly less than the FEM results. The dynamic current and electromagnetic torque at 7000 rpm and 8000 rpm (high speed operating points) are shown in Figs. 6.12 and 6.13. As shown in Figs. 6.12 and 6.13 (a), hysteresis controller cannot regulate the current at the set reference due to the voltage dynamics at higher speeds. The MEC model can calculate the current fairly in those conditions as well, compared to the FEM model. As shown in Figs. 6.12 and 6.13 (b), the generated electromagnetic torque developed in the MEC model

is in good agreement with the FEM model. The RMS current, average torque, and percentage errors relative to the FEM at different speeds are shown in Table 6.6. The design proposed from the MEC model has less than 5% error in the RMS current. The average torque calculation of the MEC-based design has maximum 2.5% error.

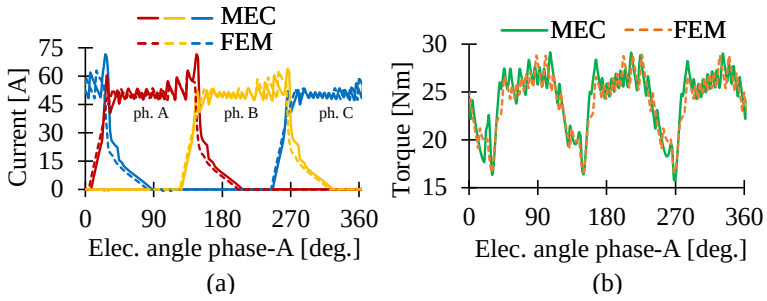

Figure 6.8: Dynamic characteristics at 2000 rpm at 385 V DC: (a) phase currents $I_{ref} = 50$ A, $\theta_{ON} = 10°$ and $\theta_{OFF} = 150°$ and (b) developed electromagnetic torque.

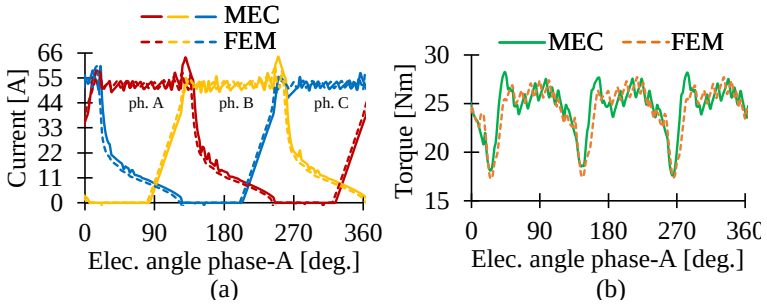

Figure 6.9: Dynamic characteristics at 4000 rpm at 385 V DC: (a) phase currents $I_{ref} = 52$ A, $\theta_{ON} = -35°$ and $\theta_{OFF} = 142°$ and (b) developed electromagnetic torque.

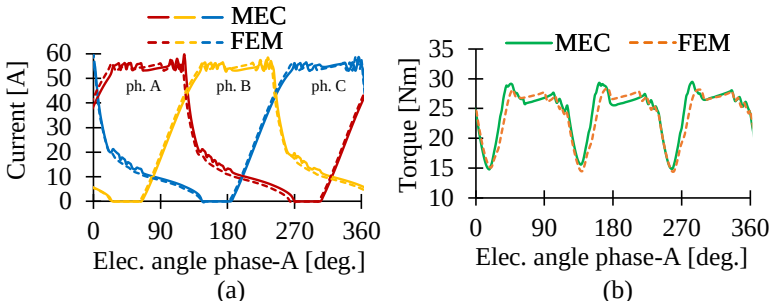

Figure 6.10: Dynamic characteristics at 5450 rpm at 385 V DC: (a) phase currents $I_{ref} = 55$ A, $\theta_{ON} = -52.5°$ and $\theta_{OFF} = 125°$ and (b) developed electromagnetic torque.

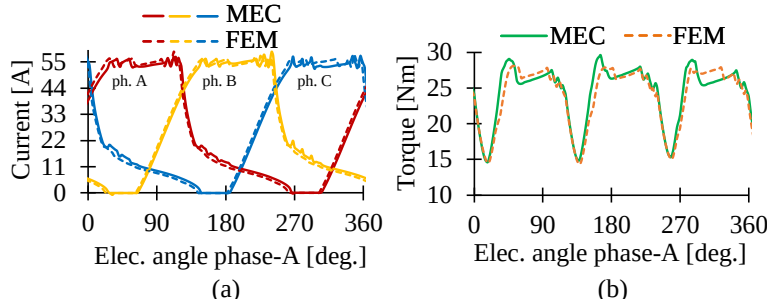

Figure 6.11: Dynamic characteristics at 5460 rpm at 385 V DC: (a) phase currents $I_{ref} = 55$ A, $\theta_{ON} = -52.5°$ and $\theta_{OFF} = 125°$ and (b) developed electromagnetic torque.

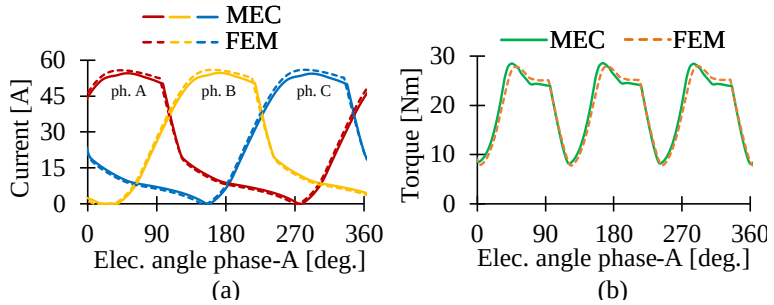

Figure 6.12: Dynamic characteristics at 7000 rpm at 385 V DC: (a) phase currents $I_{ref} = 55$ A, $\theta_{ON} = -79°$ and $\theta_{OFF} = 100°$ and (b) developed electromagnetic torque.

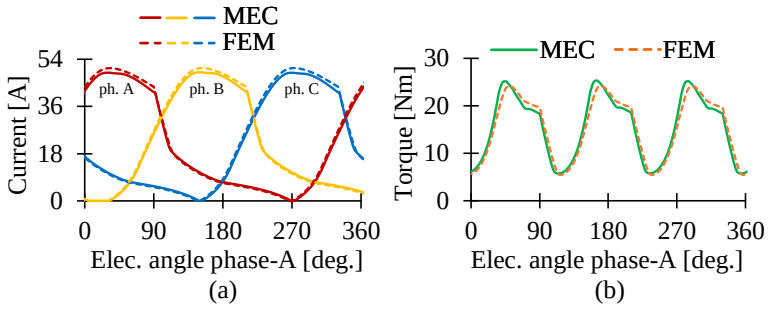

Figure 6.13: Dynamic characteristics at 8000 rpm at 385 V DC: (a) phase currents $I_{ref} = 55$ A, $\theta_{ON} = -85°$ and $\theta_{OFF} = 95°$ and (b) developed electromagnetic torque.

6.5.2 Magnetic Flux density

Fig. 6.14 shows the radial and tangential flux density waveforms at the phase-A electrical position of $\theta_{elec,phA} = 240°$, for the operating condition in Fig. 6.10. At this position, phase C is the incoming phase, and phases A and B are the outgoing phases. Flux density waveforms from the MEC model match well with the FEM results. Fig. 6.15 shows the magnetic flux density contours of the 12/16 SRM design from the MEC

Table 6.6: Comparison of RMS current and Average Torque from the MEC and FEM models.

Speed	RMS current			Avg. torque		
	MEC	FEM	% error	MEC	FEM	% error
2000 rpm	31.8 A	30.9 A	3.2 %	24.3 Nm	24.1 Nm	1.2 %
3000 rpm	34.4 A	33.9 A	1.5 %	24.2 Nm	24.1 Nm	0.4 %
4000 rpm	34. 3 A	34.1 A	0.6 %	24.6 Nm	24.4 Nm	0.8 %
5450 rpm	34.3 A	34.2 A	0.3 %	24.4 Nm	24 Nm	2.5 %
5460 rpm	34 A	34.1 A	0.3 %	24.4 Nm	24 Nm	2.5 %
6000 rpm	32 A	33. 6A	4.8 %	23.4 Nm	23.5 Nm	0.4 %
7000 rpm	31.7 A	32.5 A	2.5 %	20.1 Nm	19.9 Nm	1 %
8000 rpm	27.8 A	28.6 A	2.8 %	15.7 Nm	15.6 Nm	0.6 %

Table 6.7: Flux density comparison at points P_1, P_2, P_3, P_4, P_5 and P_6 for the dynamic operation in Fig. 6.15.

Location	MEC	FEM	% error
Point P_1	1.01 T	0.89 T	13.5 %
Point P_2	0.39 T	0.38 T	2.6 %
Point P_3	2.24 T	2.26 T	0.9 %
Point P_4	2.03 T	1.98 T	2.5 %
Point P_5	0.61 T	0.52 T	17.3 %
Point P_6	0.63 T	0.54 T	16.7 %

and FEA models for the same electrical position. There is a good match between the flux density distributions obtained from the MEC and FEM models. Flux density values and percentage errors with respect to the FEM for points P_1, P_2, P_3, P_4, P_5 and P_6 in Fig. 6.14 (a) are given in Table 6.7.

6.5.3 Torque-speed Characteristics of the 12/16 SRM Design

Fig. 6.16 shows the torque-speed and power-speed characteristics of the proposed SRM design for the peak-load operation. The calculated characteristics from the MEC-based model match well with the FEM results. As shown in Fig. 6.16 (a),

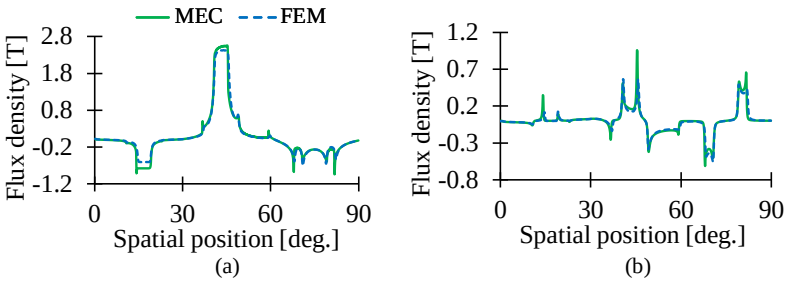

Figure 6.14: Airgap flux density at $\theta_{elec,phA} = 240°$ for phase currents in Fig. 6.10 (a) radial component and (b) tangential component.

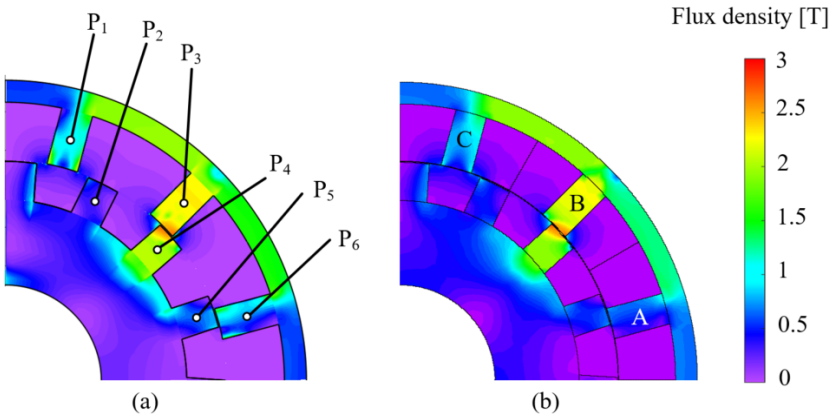

Figure 6.15: Magnetic flux density contours at $\theta_{elec,phA} = 240°$ for the current waveform in Fig. 6.10.

the proposed SRM can provide 24 Nm torque from 2000 rpm to 5460 rpm and that satisfies the design specifications. According to Fig. 6.16 (b), the proposed design can produce 14.7 kW of maximum output power, and it exceeds the given requirement 13.7 kW with the minimum DC link voltage of 385 VDC.

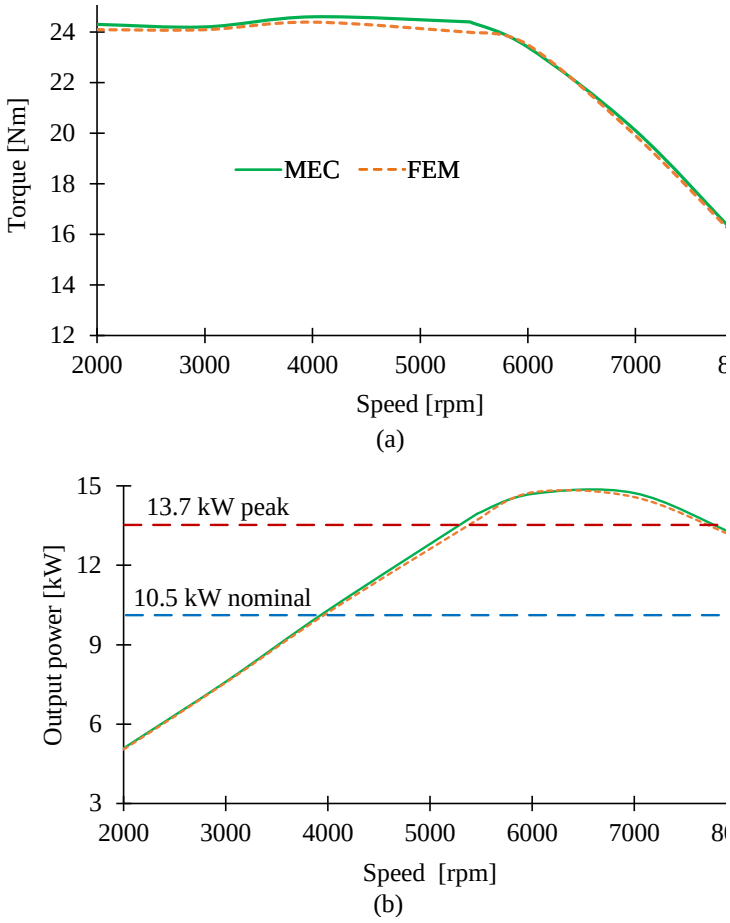

Figure 6.16: Motor characteristics for the peak operating point of the 12/16 SRM at 385 V DC link voltage: (a) torque-speed characteristics and (b) power-speed characteristics.

6.6 Summary

The proposed reluctance mesh-based MEC method in this thesis was applied to design a 3-phase 12/16 SRM for the performance requirements of the NASA HLM for the Maxwell X-57 aircraft in this chapter. The design specifications of the HLM were presented. The selection of pole configuration, geometry parameters, details of the materials for stator and rotor laminations, and selection of winding configuration were discussed. The static and dynamic characteristics of the proposed 12/16 SRM were presented. The design was validated using the FEM.

Chapter 7

Conclusions and Future Work

7.1 Conclusions

This thesis has presented a reluctance mesh-based MEC model for SRMs. The developed model can be utilized in various design stages of an SRM.

The Chapter 1 discussed the main thesis contributions and outline of the thesis. In Chapter 2, operating principle, pole configurations, winding technique, operation modes, and basics of current regulation techniques for SRMs were analyzed.

The Chapter 3 presents various modeling techniques for SRMs. Analytical as well as numerical techniques have been considered. The FEM is the most common method for SRM modeling. However, it is computationally expensive and requires a longer computation time compared to other methods. The MEC technique can alternatively be utilized for modeling SRMs. This technique has higher accuracy as compared to analytical models and it is faster and computationally inexpensive compared to the FEM. The MEC techniques can be divided into two main categories, (i) conventional MEC approach and (ii) reluctance mesh approach. In the conventional MEC, it

is required to know the flux path inside the machine in advance. The reluctance mesh-based MEC method does not require pre-defining the flux path in the machine. Finally, the chapter summarized the advantages, disadvantages, and applications of the various modeling techniques of SRMs.

In Chapter 4, the 3-phase 6/4, 6/16, and 12/8 SRMs and 4-phase 8/6, 8/10, and 16/12 SRMs have been modeled using the proposed reluctance mesh-based MEC method. The airgap flux densities, static characteristics, e.g. static phase flux linkage and static electromagnetic torque, and dynamic characteristics, e.g. magnetic flux density, current, and electromagnetic torque of the considered SRMs have been calculated using the developed MEC model. The calculated results from the MEC model were compared with the corresponding FEM models. The results of the MEC model show good agreement with FEM models. The calculated electromagnetic torque from the MEC model has a maximum error of 8.6 % in the dynamic analysis. The maximum error in the RMS current from the MEC model is 10.5 %. The simulation results of the MEC model are further validated with experimental test results. The experimental results show good agreement with the simulation results from the MEC and FEM models. The maximum error of the dynamic current in the MEC model is 1.3 % compared to the experimental results.

The Chapter 5 presents a radial force density calculation method using the proposed reluctance mesh-based MEC method. The radial and tangential components of the airgap flux density is calculated from the obtained dynamic currents of 6/4, 6/16, 12/8, 8/6, 8/10, and 16/12 SRMs using the MEC models. Maxwell Stress Tensor method was applied to determine the radial force density. The harmonics of the radial force density are determined using the 2D Fourier series. The results obtained

from the MEC model have been compared against the corresponding FEM models. The results obtained from MEC models show good agreement with the FEM models. The developed MEC model is capable of calculating the stator radial force with a maximum error of 10.19 %. The maximum error of the spatial order zero in the radial force density harmonic spectrum from the MEC model is 15.8 %. Besides, the first temporal order of the fundamental spatial order has a maximum error of 15.2 %.

The Chapter 6 presents the sizing of a three-phase 12/16 SRM proposed for the High Lift Motor (HLM) application for NASA Maxwell X-57 aircraft. NASA has designed a high-power-density PMSM using a Halbach magnet array according to defined performance and geometry constraints for the HLM. The SRM was designed to achieve similar performance and geometry constraints. The 12/16 SRM can achieve 24 Nm at 5450 rpm with 385 V minimum DC link voltage. The SRM geometry has been sized using a reluctance mesh-based MEC method. The electromagnetic performance of the SRM was validated using FEM. The phase currents, airgap flux density, and electromagnetic torque were calculated using the MEC model. The results sufficiently match the ones from the FEM model. The outer diameter of the 12/16 SRM is the same as the PMSM. The fill factor and the current density are within the design constraints given by NASA. The stack length of the SRM is longer than the PMSM. However, the total axial length of the stator is within the design constraints with the estimated end turn lengths. The stack length of the stator core can be reduced further by allowing a current density that exceeds the design constraint 11 A/mm^2. This can result in a higher operating temperature, but SRM can operate at a higher temperature than the PMSM due to the lack of PMs. This chapter demonstrates that the proposed MEC model is an effective tool for the sizing of a switched reluctance

motor. The obtained motor geometry of the 12/16 SRM using the MEC model should be further improved with more detailed FEM simulations. The losses and efficiency of the motor should be calculated in FEM. Thermal analysis would be required to determine the operating temperature of the 12/16 SRM to validate that temperature is within the allowable limits for the targeted current density.

7.2 Future Work

There are several ways to improve the contributions presented in this thesis.

Advance Meshing Techniques: The proposed structured meshing technique in this thesis can be improved in several ways. The mesh densities in the stator slots and the gaps between the rotor pole regions can be decreased to reduce the size of the matrices. That reduces the computational time of the model. The size of the matrices can be further reduced by making the arc angles of mesh elements in the rotor pole region multiples of the arc angles of airgap mesh elements.

Modeling Core Losses in SRMs: The reluctance mesh technique is a potential alternative to calculate the core losses in an SRM. The harmonics of the stator and rotor core magnetic flux density can be calculated by applying the FFT. The harmonics of the magnetic flux density can be used with the loss characteristics of electrical steel to calculate the core loss in the stator and rotor. The loss coefficients in the Steinmetz equation can be estimated, and hence, the core loss can be decomposed to hysteresis and eddy current losses.

Hybrid Modeling Techniques: The faster electromagnetic modeling techniques such as Maxwell's equations-based method and BEM can be hybridized with the MEC technique to decrease the computation time. Maxwell's equations-based method and BEM method can be applied to calculate the airgap magnetic field since those techniques are challenging to incorporate local saturation. Then, the reluctance mesh-based MEC technique can be applied to model the stator and rotor core of the SRM while considering the local saturation.

3D Reluctance Mesh-Based MEC Method: The proposed 2D reluctance mesh-based method can be extended for modeling 3D geometries. Two additional reluctance elements can be added to the mesh element along the axial direction to build a 3D mesh element. Adding more reluctance elements requires a large amount of computer memory and higher computation time. The developed nonlinear solver needs to be optimized to handle a larger number of reluctance elements efficiently.

Design Improvements of 12/16 SRM for HLM Application: The proposed motor geometry of the 3-phase 12/16 SRM requires further geometry optimization to improve the design using FEM simulations. The core losses of the motor should be calculated to estimate the efficiency. The radial force density of the 12/16 SRM should be calculated, and acoustic noise and vibration analysis would be required for the final design. Thermal analysis is required to determine the maximum operating temperature and maximum current density constraints of the motor. Prototyping and testing would be required for the further validation of the design.

Modeling Eccentricity Faults in SRMs: Airgap eccentricity is one of the common faults in SRMs. The Force distribution in the airgap becomes uneven due to the eccentricity. It causes unnecessary vibration and noise, damages bearings, and crashes stator and rotor poles each other. The reluctance mesh-based MEC method is a potential alternative to modeling eccentricity faults in SRMs. The mesh in the airgap region is required to modify according to the uneven distribution of the airgap.

7.3 Publications

Conference Papers

G. Watthewaduge, E. Sayed, A. Emadi, and B. Bilgin, "Reluctance mesh-based modeling of switched reluctance machines," in *Proc. IEEE Transportation Electrification Conference & Expo (ITEC)*, Chicago, IL, USA, Jun. 2021, pp. 407-412.

G. Watthewaduge, E. Sayed, M. Bakr, A. Emadi, and B. Bilgin, "An optimization study for a switched reluctance motor using magnetic equivalent circuit and space mapping techniques," in *Proc. IEEE Transportation Electrification Conference & Expo (ITEC)*, Chicago, IL, USA, Jun. 2020, pp. 1025-1030.

Journal Papers

G. Watthewaduge, E. Sayed, A. Emadi, and B. Bilgin, "Electromagnetic modeling techniques for switched reluctance machines: state-of-the-art review," in *IEEE Open Journal of the Industrial Electronics Society*, vol. 1, pp. 218-234, Aug. 2020.

G. Watthewaduge and B. Bilgin, "Reluctance mesh-based magnetic equivalent circuit modeling of switched reluctance motors for static and dynamic analysis," *IEEE Transactions on Transportation Electrification*, Ealy Access, 2021.

G. Watthewaduge and B. Bilgin, "Radial force density calculation of switched reluctance machines using reluctance mesh-based magnetic equivalent circuit," *IEEE Open Journal of the Industrial Electronics Society*, vol.3, pp. 37-49, Dec. 2021.

G. Watthewaduge and B. Bilgin, "Sizing of the motor geometry for an electric aircraft propulsion switched reluctance machine using reluctance mesh-based magnetic equivalent circuit," under review, *IEEE Transactions on Transportation Electrification*, 2022.

Appendix A

Motor Geometries of SRMs

The geometry parameters and main specifications of the 3-phase 6/4, 6/16, 12/8 and 4-phase 8/6, 8/10, and 16/12 SRM are presented here.

Table A.1: Geometry Parameter Values of the 3-phase 6/4 SRM.

Parameter	Value
Outer diameter (D_{out})	123 mm
Bore diameter (D_{bore})	75 mm
Shaft diameter (D_{shaft})	20 mm
Stator core Stack length (L_{stk})	65 mm
Airgap length (g)	0.5 mm
Stator pole arc angle (β_s)	22.5°
Rotor pole arc angle (β_r)	24°
Stator pole height (h_s)	14 mm
Rotor pole height (h_r)	9 mm
Stator back-iron thickness (h_{sb})	10 mm
Rotor back-iron thickness (h_{rb})	18 mm
Number of turns per coil (N_t)	80
Coil resistance (R_{coil})	0.0366 Ω
Maximum current	20 A
DC link voltage	300 V
Maximum speed	12000 rpm
Lamination material	M19-24G

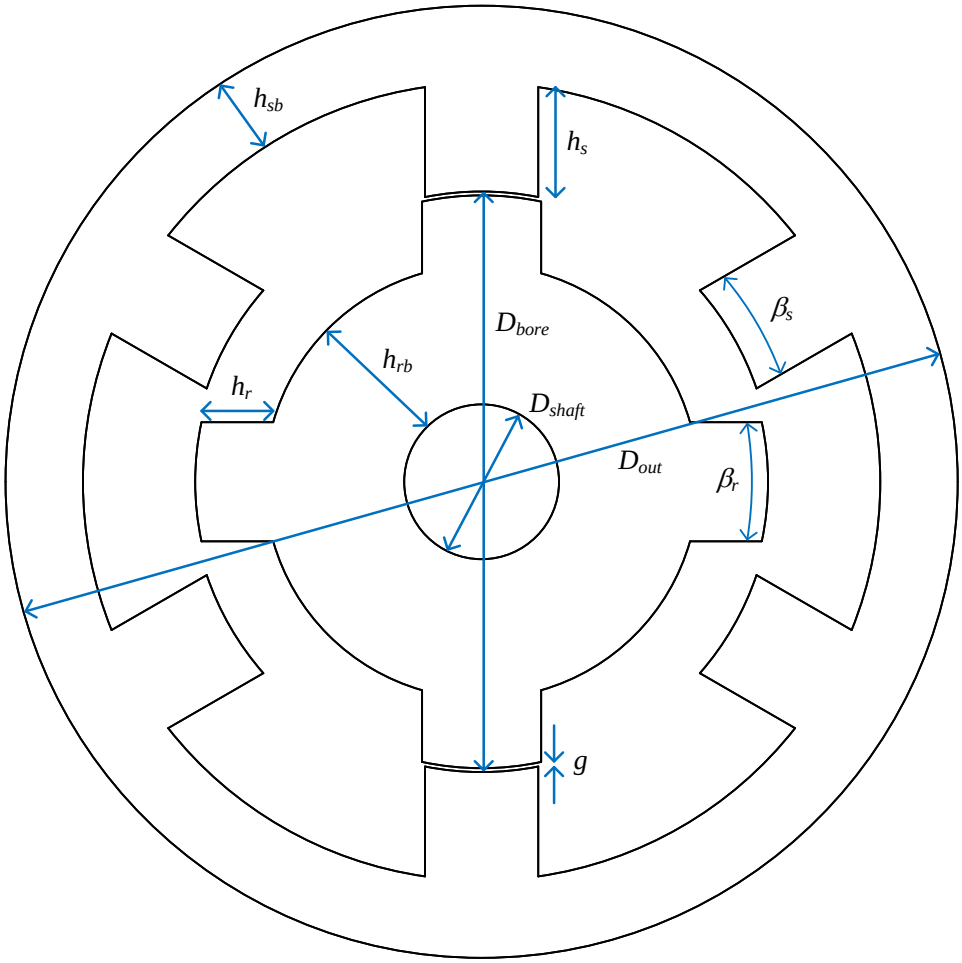

Figure A.1: Motor geometry of the 3-phase 6/4 SRM.

Table A.2: Geometry Parameter Values of the 3-phase 6/16 SRM.

Parameter	Value
Outer diameter (D_{out})	160 mm
Bore diameter (D_{bore})	125 mm
Shaft diameter (D_{shaft})	40 mm
Stator core Stack length (L_{stk})	60 mm
Airgap length (g)	0.35 mm
Stator pole arc angle (β_s)	9°
Rotor pole arc angle (β_r)	9.375°
Stator pole height (h_s)	10
Rotor pole height (h_r)	9
Stator back-iron thickness (h_{sb})	7.5 mm
Rotor back-iron thickness (h_{rb})	33.15 mm
Number of turns per coil (N_t)	50
Coil resistance (R_{coil})	0.06758 Ω
Maximum current	20 A
DC link voltage	300 V
Maximum speed	8000 rpm
Lamination material	35H300

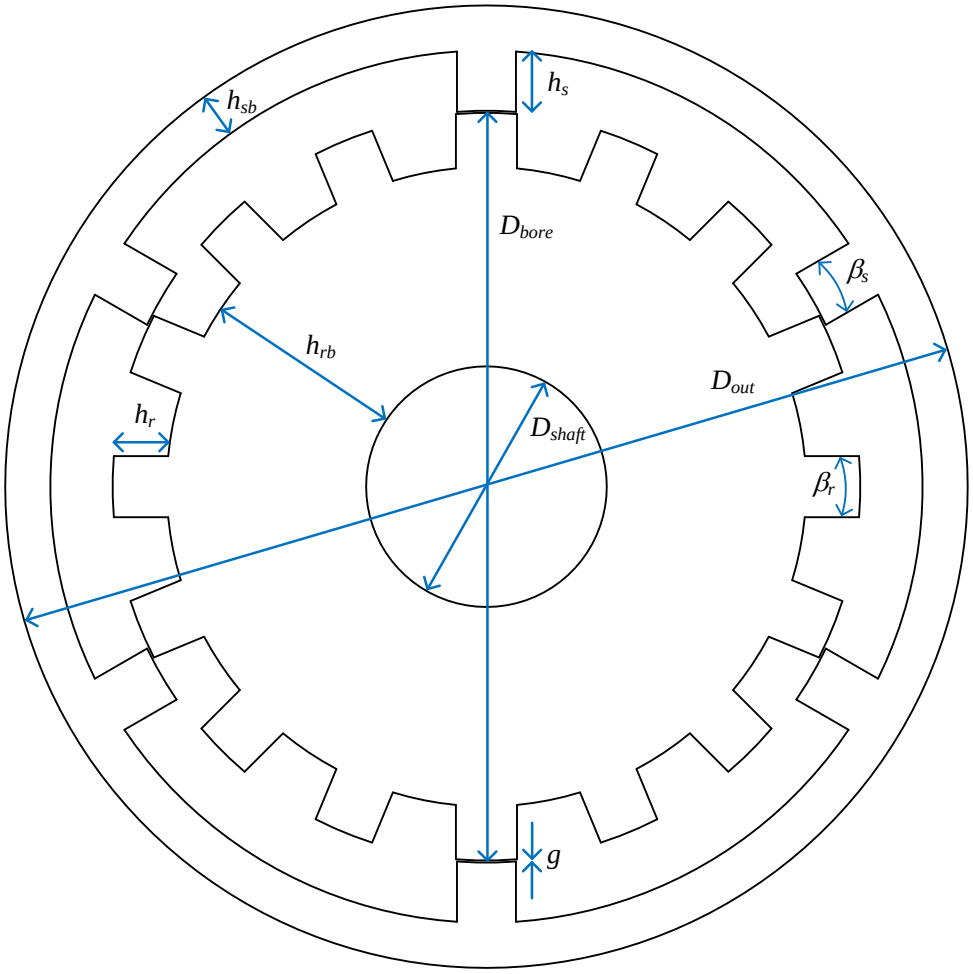

Figure A.2: Motor geometry of the 3-phase 6/16 SRM.

Table A.3: Geometry Parameter Values of the 3-phase 12/8 SRM.

Parameter	Value
Outer diameter (D_{out})	136 mm
Bore diameter (D_{bore})	83.6 mm
Shaft diameter (D_{shaft})	25 mm
Stator core Stack length (L_{stk})	70 mm
Airgap length (g)	0.3 mm
Stator pole arc angle (β_s)	15°
Rotor pole arc angle (β_r)	15°
Stator pole height (h_s)	14.9 mm
Rotor pole height (h_r)	11 mm
Stator back-iron thickness (h_{sb})	11.3 mm
Rotor back-iron thickness (h_{rb})	18 mm
Number of turns per coil (N_t)	28
Coil resistance (R_{coil})	0.052913 Ω
Maximum current	20 A
DC link voltage	300 V
Maximum speed	10000 rpm
Lamination material	35H300

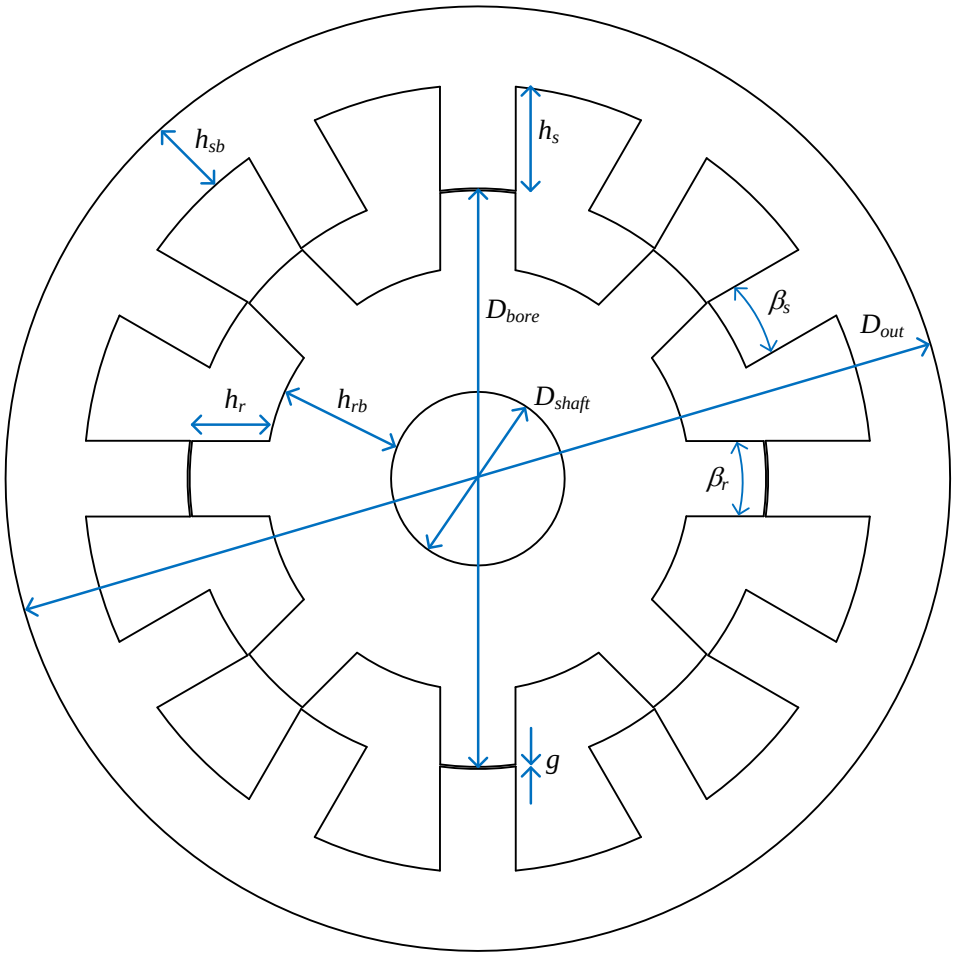

Figure A.3: Motor geometry of the 3-phase 12/8 SRM.

Table A.4: Geometry Parameter Values of the 4-phase 8/6 SRM.

Parameter	Value
Outer diameter (D_{out})	170 mm
Bore diameter (D_{bore})	90 mm
Shaft diameter (D_{shaft})	30 mm
Stator core Stack length (L_{stk})	90 mm
Airgap length (g)	0.35 mm
Stator pole arc angle (β_s)	23°
Rotor pole arc angle (β_r)	21°
Stator pole height (h_s)	23 mm
Rotor pole height (h_r)	10.15 mm
Stator taper angle (τ_s)	3°
Rotor taper angle (τ_r)	15°
Stator back-iron thickness (h_{sb})	17 mm
Rotor back-iron thickness (h_{rb})	19.5 mm
Number of turns per coil (N_t)	33
Coil resistance (R_{coil})	0.038064 Ω
Maximum current	35 A
DC link voltage	300 V
Maximum speed	10000 rpm
Lamination material	35H300

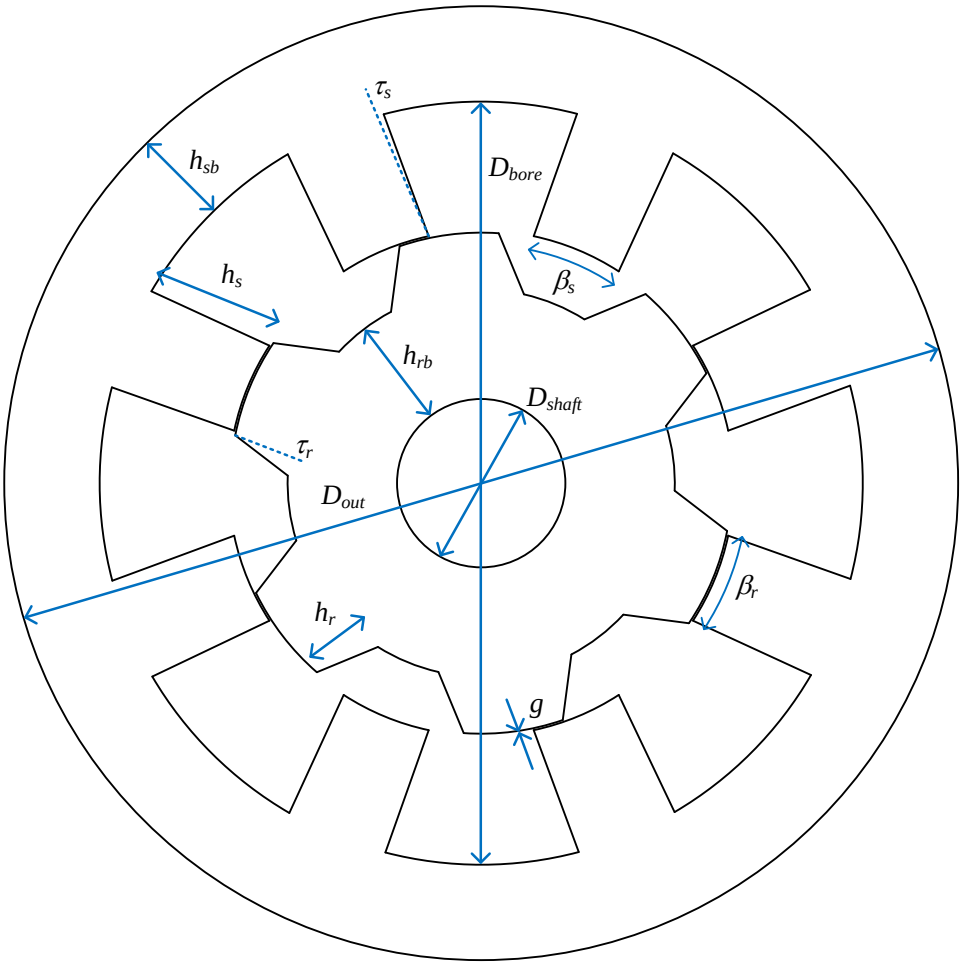

Figure A.4: Motor geometry of the 4-phase 8/6 SRM.

Table A.5: Geometry Parameter Values of the 4-phase 8/10 SRM.

Parameter	Value
Outer diameter (D_{out})	180 mm
Bore diameter (D_{bore})	140 mm
Shaft diameter (D_{shaft})	50 mm
Stator core Stack length (L_{stk})	60 mm
Airgap length (g)	0.35 mm
Stator pole arc angle (β_s)	11°
Rotor pole arc angle (β_r)	11.25°
Stator pole height (h_s)	12 mm
Rotor pole height (h_r)	10 mm
Stator back-iron thickness (h_{sb})	8 mm
Rotor back-iron thickness (h_{rb})	34.65 mm
Number of turns per coil (N_t)	40
Coil resistance (R_{coil})	0.08521 Ω
Maximum current	20 A
DC link voltage	300 V
Maximum speed	10000 rpm
Lamination material	35H300

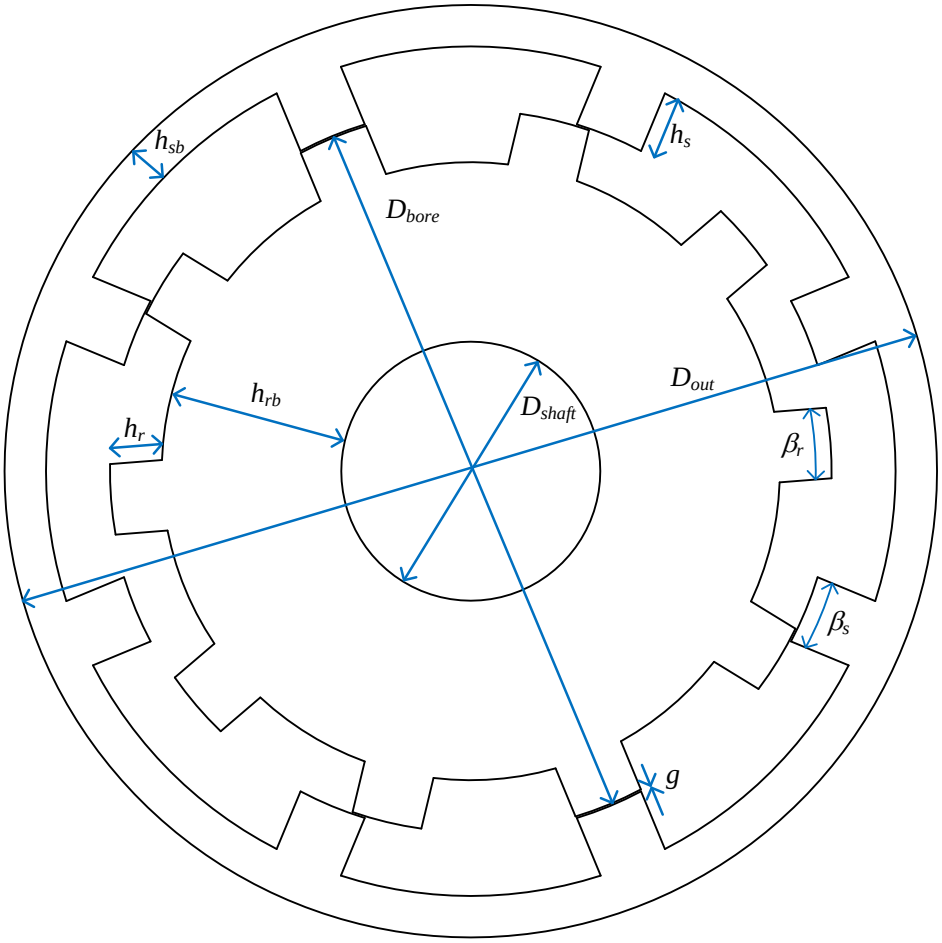

Figure A.5: Motor geometry of the 4-phase 8/10 SRM.

Table A.6: Geometry Parameter Values of the 4-phase 16/12 SRM.

Parameter	Value
Outer diameter (D_{out})	204 mm
Bore diameter (D_{bore})	160 mm
Shaft diameter (D_{shaft})	60 mm
Stator core Stack length (L_{stk})	60 mm
Airgap length (g)	0.4 mm
Stator pole arc angle (β_s)	11°
Rotor pole arc angle (β_r)	11.5°
Stator pole height (h_s)	12 mm
Rotor pole height (h_r)	9 mm
Stator back-iron thickness (h_{sb})	10 mm
Rotor back-iron thickness (h_{rb})	40.6 mm
Number of turns per coil (N_t)	30
Coil resistance (R_{coil})	0.02975 Ω
Maximum current	20 A
DC link voltage	300 V
Maximum speed	10000 rpm
Lamination material	35H300

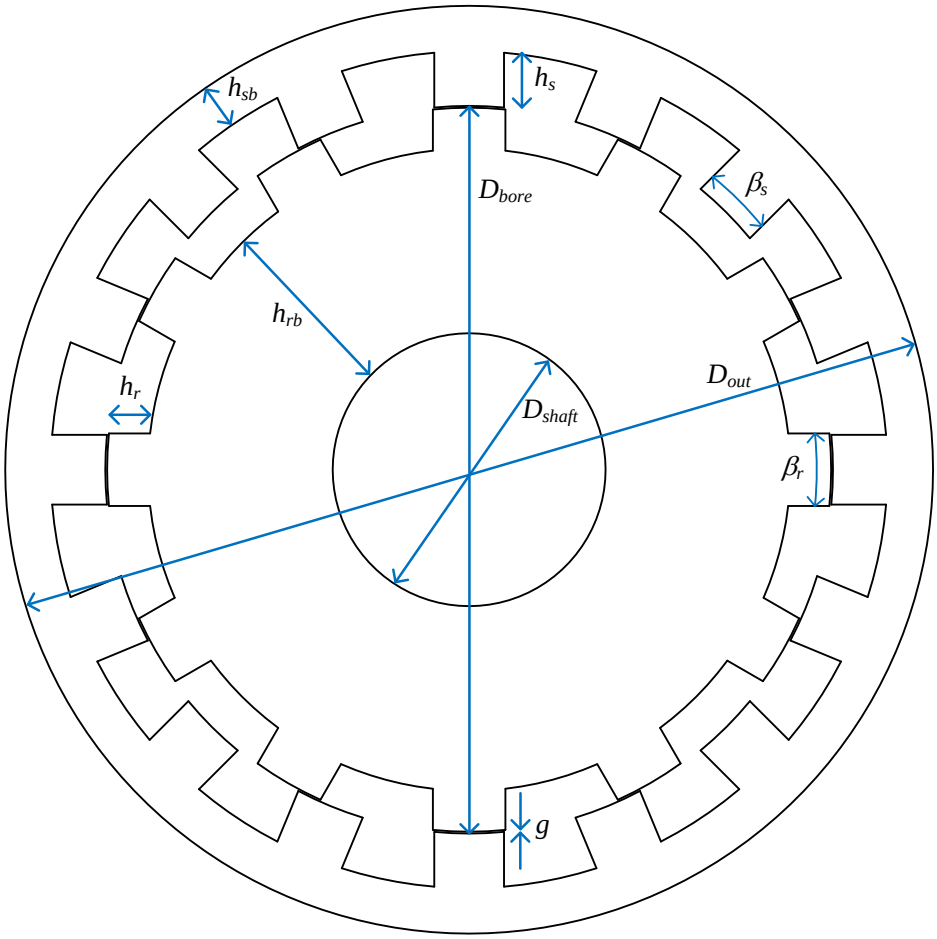

Figure A.6: Motor geometry of the 4-phase 16/12 SRM.

Appendix B

An Example Formulation of MEC

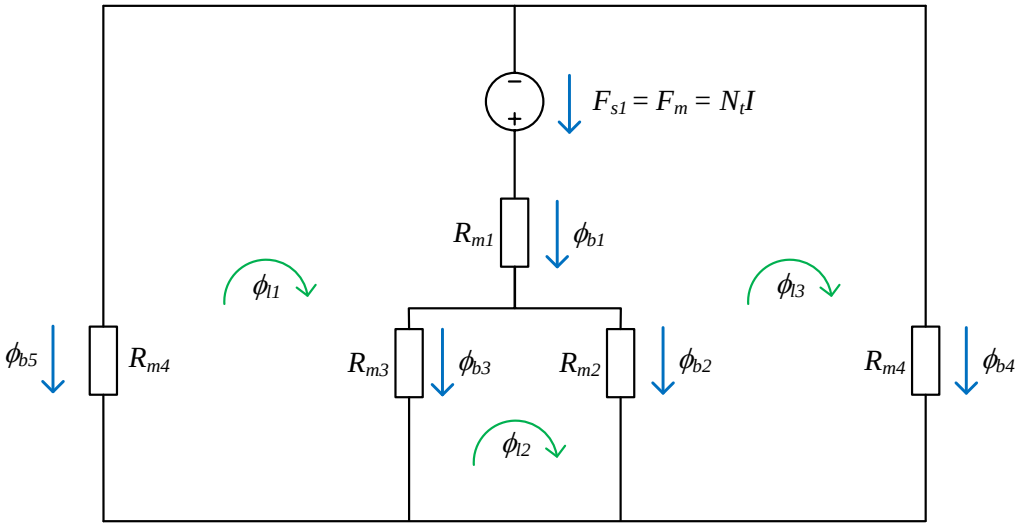

Figure B.1: An example MEC.

From equation (4.2.12):

$$\boldsymbol{L} = \begin{pmatrix} 1 & 0 & -1 \\ 0 & 1 & -1 \\ 1 & -1 & 0 \\ 0 & 0 & 1 \\ -1 & 0 & 0 \end{pmatrix} \tag{B.0.1}$$

$$\boldsymbol{R}_b = \begin{pmatrix} R_{m1} \\ R_{m2} \\ R_{m3} \\ R_{m4} \\ R_{m4} \end{pmatrix} \tag{B.0.2}$$

From equation (4.2.11):

$$\boldsymbol{R} = \begin{pmatrix} R_{m1} + R_{m3} + R_{m4} & -R_{m3} & -R_{m1} \\ -R_{m3} & R_{m2} + R_{m3} & -R_{m2} \\ -R_{m1} & -R_{m2} & R_{m1} + R_{m3} + R_{m4} \end{pmatrix} \tag{B.0.3}$$

$$\boldsymbol{N}_b = \begin{pmatrix} N_t \\ 0 \\ 0 \\ 0 \\ 0 \end{pmatrix} \tag{B.0.4}$$

There is only single stator pole in the MEC shown in Fig. B.1. By using equation (4.2.15):

$$\boldsymbol{M} = \begin{pmatrix} 1 \\ 1 \\ 1 \\ 1 \\ 1 \end{pmatrix} \tag{B.0.5}$$

From equations (4.2.13) and (4.2.14):

$$\boldsymbol{F}_l = \begin{pmatrix} N_t I \\ 0 \\ -N_t I \end{pmatrix} = \begin{pmatrix} F_m \\ 0 \\ -F_m \end{pmatrix} \tag{B.0.6}$$

$\boldsymbol{C}$ can be derived from (4.2.19)

$$\boldsymbol{C} = \begin{pmatrix} 1 & 1 & 1 \\ 1 & 1 & 1 \\ 1 & 1 & 1 \end{pmatrix} \tag{B.0.7}$$

Appendix C

Boundary Conditions

There are three main boundary conditions that can be applied in the MEC model.

1. Dirichlet boundary condition.
2. Neumann boundary condition.
3. Periodic boundary condition.

C.1 Dirichlet Boundary Condition

In the Dirichlet boundary condition, the flux flow is tangential to the boundary interface as shown in Fig. C.1. Reluctance elements along the radial direction can be removed from the mesh elements to force the tangential flux flow at the interface.

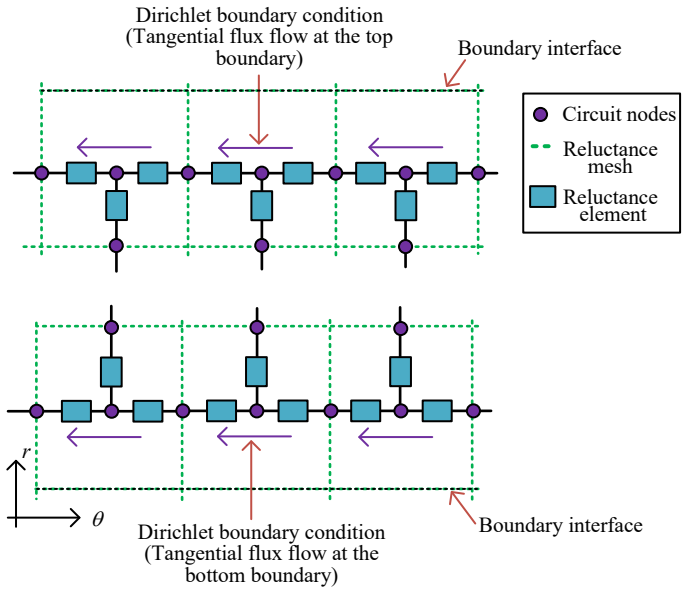

Figure C.1: An example for imposing Dirichlet boundary condition.

C.2 Neumann Boundary Condition

As shown in Fig. C.2, the flux flow is perpendicular to the boundary interface for the Neumann boundary condition. Reluctance elements along the radial/tangential directions can be connected as shown in Fig. C.2 to impose the Neumann boundary condition at the interface.

C.3 Periodic Boundary Conditions

The periodic boundary conditions can be applied based on the periodicity in the geometry. The reluctance elements at the two boundary interfaces can be connected as shown in Fig. C.3 (a) to impose the periodic boundary condition. For imposing anti-periodic boundary conditions, reluctance elements can be connected similar to periodic boundary conditions. However, the loop flux direction at the left boundary

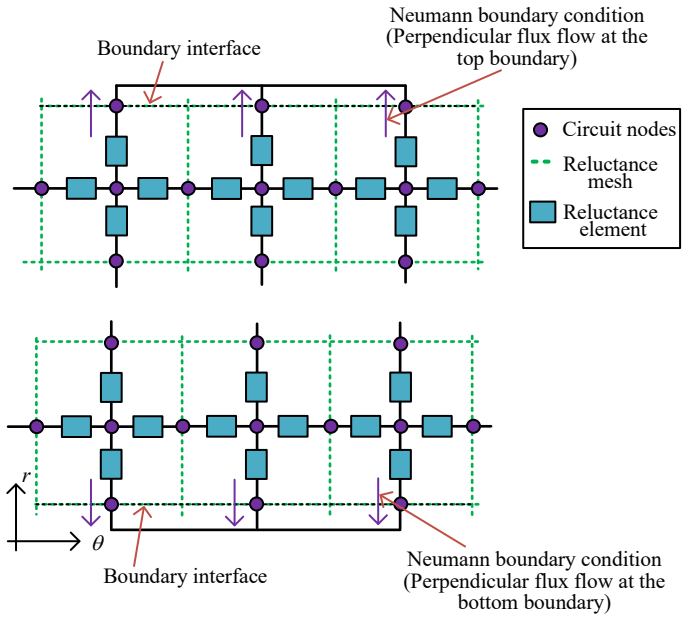

Figure C.2: An example for imposing Neumann boundary condition.

surface is considered to be opposite to the right boundary surface as shown in Fig. C.3 (b).

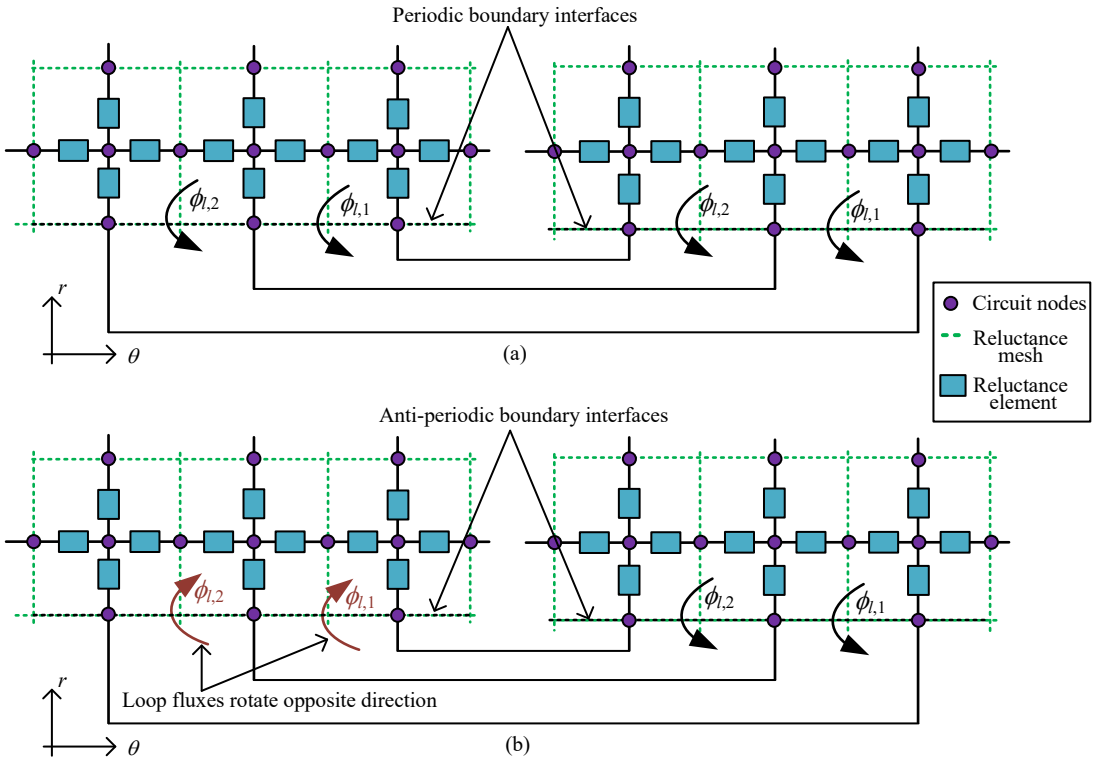

Figure C.3: An example for imposing Periodic boundary conditions (a) periodic bounary and (b) anti-periodic boundary.

References

[1] G. Watthewaduge, E. Sayed, A. Emadi, and B. Bilgin, "Electromagnetic modeling techniques for switched reluctance machines: State-of-the-art review," *IEEE Open Jour. of the Ind. Electron. Society*, vol. 1, pp. 218–234, Aug. 2020.

[2] G. Watthewaduge, E. Sayed, A. Emadi, and B. Bilgin, "Reluctance mesh-based modeling of switched reluctance machines," in *Proc. IEEE Transp. Electrification Conf. & Expo (ITEC)*, Chicago, IL, USA, Jun. 2021, pp. 407–412.

[3] D. Hall, J. Chin, A. Anderson, A. Smith, R. Edwards, and K. P. Duffy, "Development of a maxwell x-57 high lift motor reference design," in *Proc. AIAA Propulsion and Energy Forum*, Indianapolis, IN, USA, Aug. 2019, pp. 4481–4502.

[4] G. Watthewaduge and B. Bilgin, "Reluctance mesh-based magnetic equivalent circuit modeling of switched reluctance motors for static and dynamic analysis," *IEEE Trans. Transp. Electr.*, Early Access, 2021.

[5] G. Watthewaduge and B. Bilgin, "Radial force density calculation of switched reluctance machines using reluctance mesh-based magnetic equivalent circuit," *IEEE Open Jour. of the Ind. Electron. Society*, vol. 3, pp. 37–49, Dec. 2021.

[6] B. Bilgin, J. W. Jiang, and A. Emadi, *Switched reluctance motor drives: fundamentals to applications*. Boca Raton: CRC Press, 2019.

[7] B. Howey, B. Bilgin, and A. Emadi, "Design of an external-rotor direct drive e-bike switched reluctance motor," *IEEE Trans. Veh. Technol.*, vol. 69, no. 3, pp. 2552–2562, Jan. 2020.

[8] J. W. Jiang, B. Bilgin, and A. Emadi, "Three-phase 24/16 switched reluctance machine for a hybrid electric powertrain," *IEEE Trans. Transp. Electr.*, vol. 3, no. 1, pp. 76–85, Feb. 2017.

[9] S. Li, S. Zhang, T. G. Habetler, and R. G. Harley, "Modeling, design optimization, and applications of switched reluctance machines-a review," *IEEE Trans. Ind. Appl.*, vol. 55, no. 3, pp. 2660–2681, Feb. 2019.

[10] M. Yilmaz and P. T. Krein, "Capabilities of finite element analysis and magnetic equivalent circuits for electrical machine analysis and design," in *Proc. IEEE Power Electron. Specialists Conf.*, Rhodes, Greece, Jun. 2008, pp. 4027–4033.

[11] A. Labak and N. C. Kar, "Designing and prototyping a novel five-phase pancake-shaped axial-flux srm for electric vehicle application through dynamic fea incorporating flux-tube modeling," *IEEE Trans. Ind. Appl.*, vol. 49, no. 3, pp. 1276–1288, Jun. 2013.

[12] W. Ding, Z. Yin, L. Liu, J. Lou, Y. Hu, and Y. Liu, "Magnetic circuit model and finite-element analysis of a modular switched reluctance machine with e-core stators and multi-layer common rotors," *IET Electric Power Appl.*, vol. 8, no. 8, pp. 296–309, Sep. 2014.

[13] V. Ostovic, *Dynamics of saturated electric machines*. New York: Springer Science & Business Media, 2012.

[14] S. Yavuz, N. Parspour, and L. Ma, "Analytical modelling of a parametrized switched reluctance motor with adapting flux tube method," in *Proc. IEEE Int. Conf. on Ind. Tech. (ICIT)*, Lyon, France, Feb. 2018, pp. 335–340.

[15] A. Deihimi, S. Farhangi, and G. Henneberger, "A general nonlinear model of switched reluctance motor with mutual coupling and multiphase excitation," *Elect. Eng.*, vol. 84, no. 3, pp. 143–158, Jul. 2002.

[16] Q. Yu, X. Wang, and Y. Cheng, "Magnetic modeling of saliency effect for saturated electrical machines with a new calculation method," *IEEE Trans. Magn.*, vol. 52, no. 6, pp. 1–6, Jan. 2016.

[17] S.-H. Mao, D. Dorrell, and M.-C. Tsai, "Fast analytical determination of aligned and unaligned flux linkage in switched reluctance motors based on a magnetic circuit model," *IEEE Trans. Magn.*, vol. 45, no. 7, pp. 2935–2942, Jun. 2009.

[18] G. Davarpanah and J. Faiz, "Nonlinear modeling of a c-core connected two-phase switched reluctance motor," *IEEE Trans. Energy Convers.*, pp. 1–1, Feb. 2021.

[19] H. Chen and W. Yan, "Flux characteristics analysis of a double-sided switched reluctance linear machine under the asymmetric air gap," *IEEE Trans. Ind. Electron.*, vol. 65, no. 12, pp. 9843–9852, Feb. 2018.

[20] W. Sun, Q. Li, L. Sun, L. Zhu, and L. Li, "Electromagnetic analysis on novel rotor-segmented axial-field srm based on dynamic magnetic equivalent circuit," *IEEE Trans. Magn.*, vol. 55, no. 6, pp. 1–5, Mar. 2019.

[21] N. Li, J. Zhu, M. Lin, G. Yang, Y. Kong, and L. Hao, "Analysis of axial field flux-switching memory machine based on 3-d magnetic equivalent circuit network considering magnetic hysteresis," *IEEE Trans. Magn.*, vol. 55, no. 6, pp. 1–4, Mar. 2019.

[22] M. Amrhein and P. T. Krein, "3-d magnetic equivalent circuit framework for modeling electromechanical devices," *IEEE Trans. Energy Convers.*, vol. 24, no. 2, pp. 397–405, May. 2009.

[23] J. Perho, *Reluctance network for analysing induction machines*. Helsinki University of Technology, 2002, ch. 3, pp. 43–58.

[24] A. Hemeida, A. Lehikoinen, P. Rasilo, H. Vansompel, A. Belahcen, A. Arkkio, and P. Sergeant, "A simple and efficient quasi-3d magnetic equivalent circuit for surface axial flux permanent magnet synchronous machines," *IEEE Trans. Ind. Electron.*, vol. 66, no. 11, pp. 8318–8333, Dec. 2018.

[25] D. Cao, W. Zhao, J. Ji, L. Ding, and J. Zheng, "A generalized equivalent magnetic network modeling method for vehicular dual-permanent-magnet vernier machines," *IEEE Trans. Energy Convers.*, vol. 34, no. 4, pp. 1950–1962, Jun. 2019.

[26] S. Asfirane, S. Hlioui, Y. Amara, O. De La Barriere, G. Barakat, and M. Gabsi, "Global quantities computation using mesh-based generated reluctance networks," *IEEE Trans. Magn.*, vol. 54, no. 11, pp. 1–4, Oct. 2018.

[27] R. Krishnan, *Switched reluctance motor drives: modeling, simulation, analysis, design, and applications*. Boca Raton: CRC press, 2017.

[28] X. Ma, G. Li, G. Jewell, and Z. Zhu, "Recent development of reluctance machines with different winding configurations, excitation methods, and machine structures," *CES Trans. on Elect. Mach. and Sys.*, vol. 2, no. 1, pp. 82–92, Mar. 2018.

[29] H. Chen, W. Yan, J. J. Gu, and M. Sun, "Multiobjective optimization design of a switched reluctance motor for low-speed electric vehicles with a taguchi–cso algorithm," *IEEE/ASME Trans. Mechatronics*, vol. 23, no. 4, pp. 1762–1774, Aug. 2018.

[30] C. Ma and L. Qu, "Multiobjective optimization of switched reluctance motors based on design of experiments and particle swarm optimization," *IEEE Trans. Energy Convers.*, vol. 30, no. 3, pp. 1144–1153, Sep. 2015.

[31] B. Fahimi, A. Emadi, and R. B. Sepe, "Four-quadrant position sensorless control in srm drives over the entire speed range," *IEEE Trans. Power Electron.*, vol. 20, no. 1, pp. 154–163, Jan. 2005.

[32] X. Xue, K. W. E. Cheng, J. Lin, Z. Zhang, K. Luk, T. W. Ng, and N. C. Cheung, "Optimal control method of motoring operation for srm drives in electric vehicles," *IEEE Trans. Veh. Technol.*, vol. 59, no. 3, pp. 1191–1204, Mar. 2010.

[33] Y. Zhang, K. Chau, J. Jiang, D. Zhang, and C. Liu, "A finite element–analytical method for electromagnetic field analysis of electric machines with free rotation," *IEEE Trans. Magn.*, vol. 42, no. 10, pp. 3392–3394, Oct. 2006.

[34] T. Lubin, H. Razik, and A. Rezzoug, "Magnetic saturation effects on the control of a synchronous reluctance machine," *IEEE Trans. Energy Convers.*, vol. 17, no. 3, pp. 356–362, Sep. 2002.

[35] G. Dajaku and D. Gerling, "Stator slotting effect on the magnetic field distribution of salient pole synchronous permanent-magnet machines," *IEEE Trans. Magn.*, vol. 46, no. 9, pp. 3676–3683, Sep. 2010.

[36] D. Wang, D. Zhang, X. Du, and X. Wang, "Unitized design methodology of linear switched reluctance motor with segmental secondary for long rail propulsion application," *IEEE Trans. Ind. Electron.*, vol. 65, no. 12, pp. 9884–9894, Dec. 2018.

[37] W. Uddin, T. Husain, Y. Sozer, and I. Husain, "Design methodology of a switched reluctance machine for off-road vehicle applications," *IEEE Trans. Ind. Appl.*, vol. 52, no. 3, pp. 2138–2147, Jun. 2016.

[38] N. Bianchi, *Electrical machine analysis using finite elements*. Boca Raton: CRC press, 2005.

[39] K. Hameyer and R. Belmans, *Numerical modelling and design of electrical machines and devices*. WIT press, 1999, vol. 1.

[40] J. Sykulski, *Computational magnetics*. Springer Science & Business Media, 1995.

[41] W. Uddin and Y. Sozer, "Analytical modeling of mutually coupled switched reluctance machines under saturation based on design geometry," *IEEE Trans. Ind. Appl.*, vol. 53, no. 5, pp. 4431–4440, Oct. 2017.

[42] A. Radun, "Analytically computing the flux linked by a switched reluctance motor phase when the stator and rotor poles overlap," *IEEE Trans. Magn.*, vol. 36, no. 4, pp. 1996–2003, Jul. 2000.

[43] K. Vijayakumar, R. Karthikeyan, S. Paramasivam, R. Arumugam, and K. Srinivas, "Switched reluctance motor modeling, design, simulation, and analysis: a comprehensive review," *IEEE Trans. Magn.*, vol. 44, no. 12, pp. 4605–4617, Dec. 2008.

[44] E. Bostanci, M. Moallem, A. Parsapour, and B. Fahimi, "Opportunities and challenges of switched reluctance motor drives for electric propulsion: a comparative study," *IEEE Trans. Transp. Electr.*, vol. 3, no. 1, pp. 58–75, Mar. 2017.

[45] A. Kladas and J. Tegopoulos, "A new scalar potential formulation for 3-d magnetostatics necessitating no source field calculation," *IEEE Trans. Magn.*, vol. 28, no. 2, pp. 1103–1106, Mar. 1992.

[46] A. Radun, "Analytical calculation of the switched reluctance motor's unaligned inductance," *IEEE Trans. Magn.*, vol. 35, no. 6, pp. 4473–4481, Nov. 1999.

[47] S. Li, S. Zhang, C. Gong, T. G. Habetler, and R. G. Harley, "An enhanced analytical calculation of the phase inductance of switched reluctance machines," *IEEE Trans. Ind. Appl.*, vol. 55, no. 2, pp. 1392–1407, Apr. 2018.

[48] M. Golzarzadeh and B. Ganji, "Analytical modelling of the linear switched reluctance motor with segmental translator," *IET Elect. Power Appl.*, vol. 13, no. 4, pp. 527–537, Apr. 2019.

[49] T. C. O'Connell and P. T. Krein, "A schwarz–christoffel-based analytical method for electric machine field analysis," *IEEE Trans. Energy Convers.*, vol. 24, no. 3, pp. 565–577, Sep. 2009.

[50] E. Ilhan, M. F. Kremers, E. T. Motoasca, J. J. Paulides, and E. A. Lomonova, "Spatial discretization methods for air gap permeance calculations in double salient traction motors," *IEEE Trans. Ind. Appl.*, vol. 48, no. 6, pp. 2165–2172, Dec. 2012.

[51] Z. Djelloul-Khedda, K. Boughrara, F. Dubas, and R. Ibtiouen, "Nonlinear analytical prediction of magnetic field and electromagnetic performances in switched reluctance machines," *IEEE Trans. Magn.*, vol. 53, no. 7, pp. 1–11, Jul. 2017.

[52] S. Li, S. Zhang, J. Dang, T. G. Habetler, and R. G. Harley, "Calculating the unsaturated inductance of 4/2 switched reluctance motors at arbitrary rotor positions based on partial differential equations of magnetic potentials," in *Proc. IEEE North American Power Symposium (NAPS)*, Charlotte, NC, USA, Nov. 2015, pp. 1–8.

[53] Z. Poming, M. Qishuang, and X. Ping, "Modeling and analysis of switched reluctance machines using an improved conformal mapping method," in *Proc. IEEE Int. Conf. on Elect. Mach. and Sys. (ICEMS)*, Harbin, China, Aug. 2019, pp. 1–4.

[54] S. Zhao, N. Cheung, C. Lee, X. Yang, and Z. Sun, "Survey of modeling methods for flux linkage of switched reluctance motor," in *Proc. IEEE Int. Conf. on Power Electron. Sys. and Appl.*, Hong Kong, Jun. 2011, pp. 1–4.

[55] J. Pan, N. C. Cheung, and J. Yang, "High-precision position control of a novel planar switched reluctance motor," *IEEE Trans. Ind. Electron.*, vol. 52, no. 6, pp. 1644–1652, Dec. 2005.

[56] P. Chancharoensook and M. F. Rahman, "Dynamic modeling of a four-phase 8/6 switched reluctance motor using current and torque look-up tables," in *Proc. IEEE Ann. Conf. of the Ind. Electron. Soc. IECON*, vol. 1, Sevilla, Spain, Nov. 2002, pp. 491–496.

[57] K. M. Rahman and S. E. Schulz, "High-performance fully digital switched reluctance motor controller for vehicle propulsion," *IEEE Trans. Ind. Appl.*, vol. 38, no. 4, pp. 1062–1071, Aug. 2002.

[58] R. B. Inderka and R. W. De Doncker, "Ditc-direct instantaneous torque control of switched reluctance drives," *IEEE Trans. Ind. Appl.*, vol. 39, no. 4, pp. 1046–1051, Aug. 2003.

[59] P. Zhang, P. A. Cassani, and S. S. Williamson, "An accurate inductance profile measurement technique for switched reluctance machines," *IEEE Trans. Ind. Electron.*, vol. 57, no. 9, pp. 2972–2979, Sep. 2010.

[60] Z. Zhihui and L. Yuren, "Numerical and analytical modeling of switched reluctance machines," *J. Comput.*, vol. 7, no. 12, pp. 3036–3043, Dec. 2012.

[61] Y. Yang and A. Emadi, "Coupled switched reluctance machine modeling and simulations," in *Proc. IEEE Conf. and Exp. Transp. Electrification Asia-Pacific (ITEC Asia-Pacific)*, Beijing, China, Sept. 2014, pp. 1–6.

[62] J. Dong, B. Howey, B. Danen, J. Lin, J. W. Jiang, B. Bilgin, and A. Emadi, "Advanced dynamic modeling of three-phase mutually coupled switched reluctance machine," *IEEE Trans. Energy Convers.*, vol. 33, no. 1, pp. 146–154, Mar. 2017.

[63] O. Safdarzadeh, A. Mahmoudi, E. Afjei, and H. Torkaman, "Rotary-linear switched reluctance motor: analytical and finite-element modeling," *IEEE Trans. Magn.*, vol. 55, no. 5, pp. 1–10, May. 2019.

[64] G. S. Buja and M. I. Valla, "Control characteristics of the srm drives. i. operation in the linear region," *IEEE Trans. Ind. Electron.*, vol. 38, no. 5, pp. 313–321, Oct. 1991.

[65] M. Hassanin, M. T. Alrifai, and D. A. Torrey, "Experimentally verified flux density models for the switched-reluctance machine," *IEEE Trans. Magn.*, vol. 37, no. 5, pp. 3818–3824, Sep. 2001.

[66] M. Stiebler and K. Liu, "An analytical model of switched reluctance machines," *IEEE Trans. Energy Convers.*, vol. 14, no. 4, pp. 1100–1107, Dec. 1999.

[67] T. Miller and M. McGilp, "Nonlinear theory of the switched reluctance motor for rapid computer-aided design," *Proc. IEE B (Electric Power Appl.)*, vol. 137, no. 6, pp. 337–347, Nov. 1990.

[68] C. Roux and M. M. Morcos, "On the use of a simplified model for switched reluctance motors," *IEEE Trans. Energy Convers.*, vol. 17, no. 3, pp. 400–405, Sep. 2002.

[69] X. Xue, K. Cheng, and S. Ho, "A self-training numerical method to calculate the magnetic characteristics for switched reluctance motor drives," *IEEE Trans. Magn.*, vol. 40, no. 2, pp. 734–737, Mar. 2004.

[70] X.-D. Xue, K. Cheng, and S. Ho, "Simulation of switched reluctance motor drives using two-dimensional bicubic spline," *IEEE Trans. Energy Convers.*, vol. 17, no. 4, pp. 471–477, Dec. 2002.

[71] V. Nasirian, S. Kaboli, A. Davoudi, and S. Moayedi, "High-fidelity magnetic characterization and analytical model development for switched reluctance machines," *IEEE Trans. Magn.*, vol. 49, no. 4, pp. 1505–1515, Apr. 2012.

[72] H.-J. Chen, D.-Q. Jiang, J. Yang, and L.-X. Shi, "A new analytical model for switched reluctance motors," *IEEE Trans. Magn.*, vol. 45, no. 8, pp. 3107–3113, Aug. 2009.

[73] M. Farshad, J. Faiz, and C. Lucas, "Development of analytical models of switched reluctance motor in two-phase excitation mode: extended miller model," *IEEE Trans. Magn.*, vol. 41, no. 6, pp. 2145–2155, Jun. 2005.

[74] D. Torrey and J. Lang, "Modelling a nonlinear variable-reluctance motor drive," *IEE Proc. B (Electric Power Appl.)*, vol. 137, no. 5, pp. 314–326, Sep. 1990.

[75] S. Mir, I. Husain, and M. E. Elbuluk, "Switched reluctance motor modeling with on-line parameter identification," *IEEE Trans. Ind. Appl.*, vol. 34, no. 4, pp. 776–783, Aug. 1998.

[76] S. A. Hossain and I. Husain, "A geometry based simplified analytical model of switched reluctance machines for real-time controller implementation," *IEEE Trans. Power Electron.*, vol. 18, no. 6, pp. 1384–1389, Nov. 2003.

[77] D. Essah and S. Sudhoff, "An improved analytical model for the switched reluctance motor," *IEEE Trans. Energy Convers.*, vol. 18, no. 3, pp. 349–356, Sep. 2003.

[78] X. Xue, K. Cheng, S. Ho, and K. Kwok, "Trigonometry-based numerical method to compute nonlinear magnetic characteristics in switched reluctance motors," *IEEE Trans. Magn.*, vol. 43, no. 4, pp. 1845–1848, Apr. 2007.

[79] C. S. Edrington, B. Fahimi, and M. Krishnamurthy, "An autocalibrating inductance model for switched reluctance motor drives," *IEEE Trans. Ind. Electron.*, vol. 54, no. 4, pp. 2165–2173, Aug. 2007.

[80] C. Yoopakdee and N. H. Fuengwarodsakul, "Analytic model of switched reluctance machine using combined fourier-polynomial approximation technique," in *Proc. IEEE Int. Conf. on Elect. Mach. (ICEM)*, Alexandroupoli, Greece, Sep. 2018, pp. 1381–1387.

[81] F. R. Salmasi and B. Fahimi, "Modeling switched-reluctance machines by decomposition of double magnetic saliencies," *IEEE Trans. Magn.*, vol. 40, no. 3, pp. 1556–1561, May. 2004.

[82] A. Khalil and I. Husain, "A fourier series generalized geometry-based analytical model of switched reluctance machines," *IEEE Trans. Ind. Appl.*, vol. 43, no. 3, pp. 673–684, Jun. 2007.

[83] C. Lin, W. Wang, M. McDonough, and B. Fahimi, "An extended field reconstruction method for modeling of switched reluctance machines," *IEEE Trans. Magn.*, vol. 48, no. 2, pp. 1051–1054, Feb. 2012.

[84] S. Song, M. Zhang, and L. Ge, "A new decoupled analytical modeling method for switched reluctance machine," *IEEE Trans. Magn.*, vol. 51, no. 3, pp. 1–4, Mar. 2015.

[85] W. Lu, A. Keyhani, and A. Fardoun, "Neural network-based modeling and parameter identification of switched reluctance motors," *IEEE Trans. Energy Convers.*, vol. 18, no. 2, pp. 284–290, Jun. 2003.

[86] O. Ustun, "Measurement and real-time modeling of inductance and flux linkage in switched reluctance motors," *IEEE Trans. Magn.*, vol. 45, no. 12, pp. 5376–5382, Dec. 2009.

[87] Z. Lin, D. S. Reay, B. W. Williams, and X. He, "Online modeling for switched reluctance motors using b-spline neural networks," *IEEE Trans. Ind. Electron.*, vol. 54, no. 6, pp. 3317–3322, Dec. 2007.

[88] G.-Z. Cao, N. Chen, S.-D. Huang, S.-S. Xiao, and J. He, "Nonlinear modeling of the flux linkage in 2-d plane for the planar switched reluctance motor," *IEEE Trans. Magn.*, vol. 54, no. 11, pp. 1–5, Nov. 2018.

[89] H. Sahraoui, H. Zeroug, and H. Toliyat, "Switched reluctance motor design using neural-network method with static finite-element simulation," *IEEE Trans. Magn.*, vol. 43, no. 12, pp. 4089–4095, Dec. 2007.

[90] S. Zhou, "Modeling of switched reluctance motor based on combined clustering rbf network," in *Proc. IEEE Int. Conf. on Elect. Mach. and Sys. (ICEMS)*, Sydney, NSW, Australia, Aug. 2017, pp. 1–5.

[91] W. Ding and D. Liang, "Modeling of a 6/4 switched reluctance motor using adaptive neural fuzzy inference system," *IEEE Trans. Magn.*, vol. 44, no. 7, pp. 1796–1804, Jul. 2008.

[92] S.-D. Huang, G.-Z. Cao, Z.-Y. He, J. Pan, J.-A. Duan, and Q.-Q. Qian, "Nonlinear modeling of the inverse force function for the planar switched reluctance motor using sparse least squares support vector machines," *IEEE Trans. Ind. Informat.*, vol. 11, no. 3, pp. 591–600, Jun. 2015.

[93] H. Likun, Y. Qingxin, and A. Jinlong, "Modeling of srm based on xs-lssvr optimized by gds," *IEEE Trans. Appl. Supercond.*, vol. 20, no. 3, pp. 1102–1105, Jun. 2010.

[94] S. R. Mousavi-Aghdam, M. R. Feyzi, N. Bianchi, and M. Morandin, "Design and analysis of a novel high-torque stator-segmented srm," *IEEE Trans. Ind. Electron.*, vol. 63, no. 3, pp. 1458–1466, Mar. 2015.

[95] J. Y. Loh, M. A. Prabhu, S. Wang, S. C. Joshi, V. Viswanathan, and S. Ramakrishna, "Optimal segmented rotor design for the embedded electrical machine for

the more electric aircraft," *The J. of Eng.*, vol. 2019, no. 17, pp. 4321–4324, Jun. 2019.

[96] A. A. S. Bukhari *et al.*, "Switched reluctance motor design for electric vehicles based on harmonics and back emf analysis," *The J. of Eng.*, vol. 2019, no. 17, pp. 4220–4225, Jun. 2019.

[97] Y. Yang, N. Schofield, and A. Emadi, "Double-rotor switched reluctance machine (drsrm)," *IEEE Trans. Energy Convers.*, vol. 30, no. 2, pp. 671–680, Jun. 2015.

[98] J. Lin, T. Lambert, Y. Yang, B. Bilgin, R. Lankin, and A. Emadi, "A novel axial flux switched reluctance motor with multi-level air gap geometry," in *Proc. IEEE Elect. Power and Energy Conf. (EPEC)*, Ottawa, ON, Canada, Oct. 2016, pp. 1–8.

[99] V. Rallabandi, J. Wu, P. Zhou, D. G. Dorrell, and D. M. Ionel, "Optimal design of a switched reluctance motor with magnetically disconnected rotor modules using a design of experiments differential evolution fea-based method," *IEEE Trans. Magn.*, vol. 54, no. 11, pp. 1–5, Nov. 2018.

[100] M. Klauz and D. G. Dorrell, "Eddy current effects in a switched reluctance motor," *IEEE Trans. Magn.*, vol. 42, no. 10, pp. 3437–3439, Oct. 2006.

[101] M. Al Eit, P. Dular, F. Bouillault, C. Marchand, and G. Krebs, "Perturbation finite element method for efficient copper losses calculation in switched reluctance machines," *IEEE Trans. Magn.*, vol. 53, no. 6, pp. 1–4, Jun. 2017.

[102] S. J. Salon, *Finite element analysis of electrical machines*. Kluwer academic publishers Boston, 1995, vol. 101.

[103] Y. Tang and J. A. Kline, "Modeling and design optimization of switched reluctance machine by boundary element analysis and simulation," *IEEE Trans. Energy Convers.*, vol. 11, no. 4, pp. 673–680, Dec. 1996.

[104] T. C. O'Connell and P. T. Krein, "A time-harmonic three-dimensional vector boundary element model for electromechanical devices," *IEEE Trans. Energy Convers.*, vol. 25, no. 3, pp. 606–618, Sep. 2010.

[105] A. M. Omekanda, C. Broche, and M. Renglet, "Calculation of the electromagnetic parameters of a switched reluctance motor using an improved fem-biem-application to different models for the torque calculation," *IEEE Trans. Ind. Appl.*, vol. 33, no. 4, pp. 914–918, Aug. 1997.

[106] D. M. Araujo, J.-L. Coulomb, O. Chadebec, and L. Rondot, "A hybrid boundary element method-reluctance network method for open boundary 3-d nonlinear problems," *IEEE Trans. Magn.*, vol. 50, no. 2, pp. 77–80, Feb. 2014.

[107] T. A. Lipo, *Introduction to AC machine design*. John Wiley & Sons, 2017.

[108] L.-L. Zhu, D. Xu, Q. Li, W. Sun, and Y.-Q. Hu, "Analysis and optimization of equivalent magnetic circuit model for a hybrid axial field flux-switching permanent magnet machine," in *Proc. IEEE Int. Conf. on Elect. Mach. and Sys. (ICEMS)*, Jeju, South Korea, Oct. 2018, pp. 407–412.

[109] J. Ma, R. Qu, and J. Li, "Optimal design of axial flux switched reluctance motor for electric vehicle application," in *Proc. IEEE Int. Conf. on Elect. Mach. and Sys. (ICEMS)*, Hangzhou, China, Oct. 2014, pp. 1860–1865.

[110] M. Preston and J. Lyons, "A switched reluctance motor model with mutual coupling and multi-phase excitation," *IEEE Trans. Magn.*, vol. 27, no. 6, pp. 5423–5425, Nov. 1991.

[111] J. M. Kokernak and D. A. Torrey, "Magnetic circuit model for the mutually coupled switched-reluctance machine," *IEEE Trans. Magn.*, vol. 36, no. 2, pp. 500–507, Mar. 2000.

[112] Y. Tang, J. J. Paulides, and E. A. Lomonova, "Automated design of dc-excited flux-switching in-wheel motor using magnetic equivalent circuits," *IEEE Trans. Magn.*, vol. 51, no. 4, pp. 1–11, Mar. 2015.

[113] C. Bruzzese, D. Zito, and A. Tessarolo, "Finite reluctance approach: a systematic method for the construction of magnetic network-based dynamic models of electrical machines," in *Proc. IEEE Ann. Conf. The Need for a More Effective Tech. Transfer (AEIT)*, Trieste, Italy, Sep. 2014, pp. 1–6.

[114] H. Xie, G. Krebs, M. H. Hassan, M. Zhang, C. Marchand, and Z. Ren, "A new reluctance network-based method with complementary distributed magnetomotive forces," *IEEE Trans. Magn.*, vol. 55, no. 6, pp. 1–5, Jun. 2019.

[115] H. Chen, W. Yan, and Z. Li, "Flux characteristics analysis of a single-phase tubular switched reluctance linear launcher," *IEEE Trans. Plasma Sci.*, vol. 47, no. 5, pp. 2316–2322, May. 2019.

[116] A. Stuikys and J. K. Sykulski, "An efficient design optimization framework for nonlinear switched reluctance machines," *IEEE Trans. Ind. Appl.*, vol. 53, no. 3, pp. 1985–1993, Jun. 2017.

[117] M. L. Bash, J. M. Williams, and S. D. Pekarek, "Incorporating motion in mesh-based magnetic equivalent circuits," *IEEE Trans. Energy Convers.*, vol. 25, no. 2, pp. 329–338, Jun. 2010.

[118] W. Peng and J. Gyselinck, "Magnetic-equivalent-circuit modelling of switched reluctance machines with mutual coupling effects," in *Proc. IEEE Int. Conf. on Elect. Mach. (ICEM)*, Lausanne, Switzerland, Sep. 2016, pp. 426–432.

[119] N. Radimov, N. Ben-Hail, and R. Rabinovici, "Simple model of switched-reluctance machine based only on aligned and unaligned position data," *IEEE Trans. Magn.*, vol. 40, no. 3, pp. 1562–1572, May 2004.

[120] D. S. Mihic, M. V. Terzic, and S. N. Vukosavic, "A new nonlinear analytical model of the srm with included multiphase coupling," *IEEE Trans. Energy Convers.*, vol. 32, no. 4, pp. 1322–1334, May 2017.

[121] J. Du, D. Liang, and X. Liu, "Performance analysis of a mutually coupled linear switched reluctance machine for direct-drive wave energy conversions," *IEEE Trans. Magn.*, vol. 53, no. 9, pp. 1–10, Jun. 2017.

[122] A. Demenko and J. K. Sykulski, "Analogies between finite-difference and finite-element methods for scalar and vector potential formulations in magnetic field calculations," *IEEE Trans. Magn.*, vol. 52, no. 6, pp. 1–6, Jun. 2016.

[123] G. Liu, S. Jiang, W. Zhao, and Q. Chen, "Modular reluctance network simulation of a linear permanent-magnet vernier machine using new mesh generation methods," *IEEE Trans. Ind. Electron.*, vol. 64, no. 7, pp. 5323–5332, Jul. 2017.

[124] T. A. Lipo, "Winding distribution in an ideal machine," in *Analysis of synchronous machines*. CRC Press, 2017, pp. 1–76.

[125] K. Masoudi, M. R. Feyzi, and A. Masoudi, "Reduction of vibration and acoustic noise in the switched reluctance motor by using new improved stator yoke shape," in *Proc. IEEE Iranian Conf. on Elec. Eng. (ICEE)*, Mashhad, Iran, May. 2013, pp. 1–4.

[126] O. Gundogmus, M. Elamin, Y. Yasa, T. Husain, Y. Sozer, J. Kutz, J. Tylenda, and R. L. Wright, "Acoustic noise mitigation of switched reluctance machines with windows on stator and rotor poles," *IEEE Trans. Ind. Appl.*, vol. 56, no. 4, pp. 3719–3730, Jul. 2020.

[127] O. N. Samani and B. Ganji, "Noise reduction of switched reluctance motors," in *Proc. IEEE Power Electron., Drive Sys. & Tech. Conf. (PEDSTC)*, Mashhad, Iran, Feb. 2017, pp. 300–304.

[128] Y. Yasa, D. Tekgun, Y. Sozer, J. Kutz, and J. Tylenda, "Effect of distributed airgap in the stator for acoustic noise reduction in switched reluctance motors," in *Proc. IEEE Appl. Power Electron. Conf. and Expo. (APEC)*, Tampa, FL, USA, Mar. 2017, pp. 633–639.

[129] A. D. Callegaro, B. Bilgin, and A. Emadi, "Radial force shaping for acoustic noise reduction in switched reluctance machines," *IEEE Trans. Power Electron.*, vol. 34, no. 10, pp. 9866–9878, Jan. 2019.

[130] A. D. Callegaro, J. Liang, J. W. Jiang, B. Bilgin, and A. Emadi, "Radial force density analysis of switched reluctance machines: the source of acoustic noise," *IEEE Trans. Transp. Electr.*, vol. 5, no. 1, pp. 93–106, Dec. 2018.

[131] I. Husain, A. Radun, and J. Nairus, "Unbalanced force calculation in switched-reluctance machines," *IEEE Trans. Magn.*, vol. 36, no. 1, pp. 330–338, Jan. 2000.

[132] M. Anwar and O. Husain, "Radial force calculation and acoustic noise prediction in switched reluctance machines," *IEEE Trans. Ind. Appl.*, vol. 36, no. 6, pp. 1589–1597, Nov. 2000.

[133] F.-C. Lin and S.-M. Yang, "An approach to producing controlled radial force in a switched reluctance motor," *IEEE Trans. Ind. Electron.*, vol. 54, no. 4, pp. 2137–2146, Jul. 2007.

[134] J. Li and Y. Cho, "Investigation into reduction of vibration and acoustic noise in switched reluctance motors in radial force excitation and frame transfer function aspects," *IEEE Trans. Magn.*, vol. 45, no. 10, pp. 4664–4667, Sep. 2009.

[135] J. Dong, J. W. Jiang, B. Howey, H. Li, B. Bilgin, A. D. Callegaro, and A. Emadi, "Hybrid acoustic noise analysis approach of conventional and mutually coupled switched reluctance motors," *IEEE Trans. Energy Convers.*, vol. 32, no. 3, pp. 1042–1051, Feb. 2017.

[136] M. Abdalmagid, M. Bakr, E. Sayed, and A. Emadi, "Adjoint sensitivity analysis of radial force components of switched reluctance machines," in *Proc. IEEE Transp. Electrification Conf. & Expo (ITEC)*, Chicago, IL, USA, Jun. 2021, pp. 1–6.

[137] M. Takemoto, A. Chiba, H. Akagi, and T. Fukao, "Radial force and torque of a bearingless switched reluctance motor operating in a region of magnetic saturation," in *Proc. IEEE Ind. Appl. Conf. 37th IAS Annual Meeting (Cat. No. 02CH37344)*, Pittsburgh, PA, USA, Oct. 2002, pp. 35–42.

[138] J. Liang, A. D. Callegaro, B. Howey, B. Bilgin, J. Dong, J. Lin, and A. Emadi, "Analytical calculation of temporal and circumferential orders of radial force density harmonics in external-rotor and internal-rotor switched reluctance machines," *IEEE Open Journal of Ind. Appl.*, vol. 2, pp. 70–81, Apr. 2021.

[139] E. Sayed, M. Abdalmagid, G. Pietrini, N.-M. Sa'adeh, A. D. Callegaro, C. Goldstein, and A. Emadi, "Review of electric machines in more/hybrid/turbo electric aircraft," *IEEE Trans. Transp. Electr.*, vol. 7, no. 4, pp. 2976–3005, Dec. 2021.

[140] B. Bilgin, J. Liang, M. V. Terzic, J. Dong, R. Rodriguez, E. Trickett, and A. Emadi, "Modeling and analysis of electric motors: state-of-the-art review," *IEEE Trans. Transp. Electr.*, vol. 5, no. 3, pp. 602–617, Sep. 2019.

[141] A. Delale, L. Albert, L. Gerbaud, and F. Wurtz, "Automatic generation of sizing models for the optimization of electromagnetic devices using reluctance networks," *IEEE Trans. Magn.*, vol. 40, no. 2, pp. 830–833, Apr. 2004.

[142] J.-J. Lee, J. Lee, and K.-S. Kim, "Design of a wfsm for an electric vehicle based on a nonlinear magnetic equivalent circuit," *IEEE Trans. Appl. Supercond.*, vol. 28, no. 3, pp. 1–4, Feb. 2018.

[143] J.-G. Lee, D.-K. Lim, and H.-K. Jung, "Analysis and design of interior permanent magnet synchronous motor using a sequential-stage magnetic equivalent circuit," *IEEE Trans. Magn.*, vol. 55, no. 10, pp. 1–4, Jul. 2019.

[144] N. Ullah, F. Khan, W. Ullah, M. Umair, and Z. Khattak, "Magnetic equivalent circuit models using global reluctance networks methodology for design of permanent magnet flux switching machine," in *Proc. IEEE Int.l Bhurban Conf. on Appl. Sciences and Tech. (IBCAST)*, Islamabad, Pakistan, Mar. 2014, pp. 397–404.

[145] S. L. Schnulo, D. L. Hall, J. C. Chin, and A. D. Smith, "Further development of the nasa x-57 maxwell mission planning tool for mods ii, iii, and iv," in *Proc. AIAA/IEEE Electric Aircraft Tech. Symposium (EATS)*, Indianapolis, IN, USA, Aug. 2019, pp. 1–14.